ARNT-independent functions of HIF2α in tumorigenesis

Dissertation

der Mathematisch-Naturwissenschaftlichen Fakultät

der Eberhard Karls Universität Tübingen

zur Erlangung des Grades eines

Doktors der Naturwissenschaften

(Dr. rer. nat.)

vorgelegt von

Liudmyla Taranets

aus Chechelnyk, Ukraine

Tübingen

2020

Gedruckt mit Genehmigung der Mathematisch-Naturwissenschaftlichen Fakultät der Eberhard Karls Universität Tübingen.

Tag der mündlichen Qualifikation:	8.12.2020
Stellvertretender Dekan:	Prof. Dr. József Fortágh
1. Berichterstatter:	Prof. Dr. Stefan Laufer
2. Berichterstatter:	Prof. Dr. Nikita Popov

Contents

Summary

Hypoxia is a significant stress factors during normal development and tumorigenesis. Cells respond to oxygen deprivation by stabilizing hypoxia-inducible transcription factors (HIFs) that regulate genes controlling cellular metabolism, angiogenesis, cell proliferation, migration and invasion. HIFs can also accumulate due to mutations in the VHL ubiquitin ligase and drive tumor growth and metastasis, e.g. in renal cancers. Most of the functions of HIFs in transcription are thought to depend on dimerization with the ARNT protein. Small molecule inhibitors disrupting the HIF2α-ARNT complex are currently in clinical trials with preliminary data indicating that they are able to suppress primary tumor growth in renal carcinomas; nevertheless their impact on metastasis has not been investigated.

Here we show that some HIF2α-dependent cellular responses, such as invasion and migration, do not require interaction with ARNT. Results of our cell-based assays and *in vivo* studies show that migration, invasion and metastasis in renal and colorectal cancer can be regulated by HIF2α independently of ARNT.

Transcriptome profiling showed that inhibitors of the HIF2α-ARNT dimer, as well as the HIF2α mutant incapable of binding ARNT, only partially block HIF2α-dependent transcription. Interestingly, we found that HIF2α interacts with and deregulates the function of the epigenetic modifier EZH2. We show that pharmacologic or genetic inhibition of EZH2 suppresses HIF2α-dependent invasion of cancer cells. In addition, we found that HIF2α binds and controls the turnover of β-catenin and E-cadherin, proteins that are known to mediate cell migration and invasion. Overall, our results suggest that pharmacologic targeting of EZH2 activity and stabilization of cadherins can synergize with HIF2α inhibition which might have a potential as a novel therapeutic approach to control tumor development and metastatic dissemination.

Zusammenfassung

Hypoxie ist einer der wesentlichen Stressfaktoren während der normalen Entwicklung und während der Tumorentstehung. Zellen reagieren auf Sauerstoffmangel mit der Stabilisierung von Hypoxie-induzierbaren Transkriptionsfaktoren (HIFs), die Gene regulieren, die den zellulären Stoffwechsel, die Angiogenese, die Zellproliferation, die Migration und die Invasion steuern. HIFs können sich auch aufgrund von Mutationen im VHL-Ubiquitin-Ligasegen akkumulieren und das Tumorwachstum und die Metastasierung fördern., z.B. bei Nierenkrebs. Man nimmt an, dass die meisten Funktionen der HIFs bei der Transkription von der Dimerisierung mit dem ARNT-Protein abhängen. Kleinmolekulare Inhibitoren, die auf den HIF2α-ARNT-Komplex abzielen, befinden sich derzeit in klinischen Studien, die eine Unterdrückung des Primärtumorwachstums bei Nierenkarzinomen zeigen; ihr Einfluss auf die Metastasierung ist jedoch noch nicht untersucht worden.

Hier zeigen wir, dass einige HIF2α-abhängige zelluläre Reaktionen, wie z.B. Invasion und Migration, keine Interaktion mit ARNT erfordern. Die Ergebnisse unserer zellbasierten Assays und *in vivo*-Studien zeigen, dass Migration, Invasion und Metastasierung bei Nieren- und Darmkrebs durch HIF2α unabhängig von ARNT reguliert werden können.

Die Erstellung von Transkriptom-Profilen zeigte, dass Inhibitoren des HIF2α-ARNT-Dimers sowie der HIF2α-Mutant, der nicht in der Lage ist, ARNT zu binden, die HIF2α-abhängige Transkription nur teilweise blockieren. Interessanterweise fanden wir heraus, dass HIF2α mit dem epigenetischen Modifikator EZH2 interagiert und dessen Funktion dereguliert. Wir zeigen, dass die pharmakologische oder genetische Inhibition von EZH2 die HIF2α-abhängige Invasion von Krebszellen unterdrückt. Darüber hinaus konnten wir zeigen, dass HIF2α den Umsatz von β-Catenin und E-Cadherin, bindet und kontrolliert. Von diesen Proteinen ist bekannt, dass sie die Zellmigration und -invasion vermitteln.

Insgesamt deuten unsere Ergebnisse darauf hin, dass die pharmakologische Hemmung der EZH2-Aktivität und die Stabilisierung von Cadherinen mit der Hemmung von HIF2α synergetisch zusammenwirken kann. Eine solche Kombination hat das Potenzial, als therapeutischer Ansatz zur Kontrolle der Tumorentwicklung und der Metastasierung eingesetzt zu werden.

1. Introduction

1.1. Hypoxia inducible factors are major mediators of cellular adaptation to the hypoxic microenvironment in tumors

Insufficient tissue oxygenation – the state of hypoxia – is a part of normal physiology (1) and during mammalian embryogenesis O_2 at concentrations of 1 %–5 % functions as a morphogen (2). Three Nobel Prizes in Physiology or Medicine were awarded for studying the mechanisms of cellular and tissue response to oxygen levels. In 1931 Otto Warburg discovered the enzymatic basis for cellular respiration. In 1938 Corneille Heymans showed the involvement of the nervous system in the respiration control (he showed that the carotid body adjacent to large blood vessels on both sides of the neck contains specialized cells that sense the blood's oxygen levels and controls our respiratory rate by communicating directly with the brain). And finally, Gregg Semenza, William Kaelin, and Peter Ratcliffe made fundamental discoveries on the action of the hypoxia inducible factors (HIFs), transcription factors which mediate gene regulation in response to oxygen changes.

In human cancers intratumoral hypoxia comprises a part of their microenvironment (3) and is primarily triggered by the imbalanced growth of the tumor lesion and impaired vasculature, resulting in a deficient supply of nutrients and oxygen (4). Oxygenation in solid tumors varies from physiologic levels of approximately 5 % - 8 % O_2 to near anoxia (Semenza, 2012). Tumor-associated hypoxia significantly affects most of the hallmarks of cancer, though is not being recognized as a separate hallmark itself. So far, it was shown that hypoxia regulates cell proliferation, apoptosis, differentiation and self-renewal, tumor angiogenesis, genetic instability, tumor metabolism, antitumor immune response, resistance to

chemo- and radiotherapy, and most interesting for the current project – tumor cell invasion and metastasis (summary presented in Fig. 1).

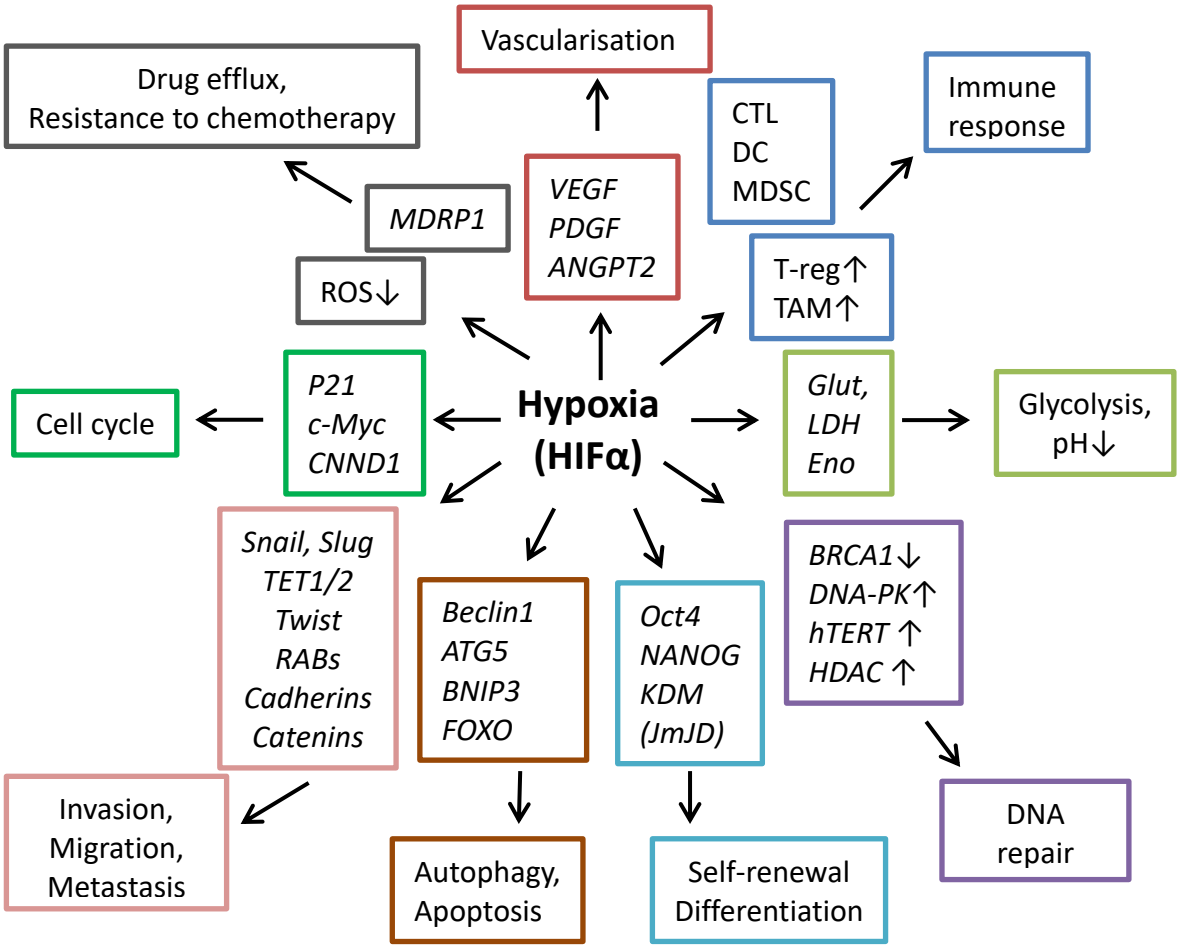

Figure 1. Hypoxia and HIFs regulate multiple features of cancer. HIFs are proteins that respond to oxygen levels by acting as transcription factors and mediate adaptation to the hypoxic tumor microenvironment by regulating multiple genes and processes. Modified from Wigerup et al. (5-8).

Cells can adapt to the hypoxic microenvironment by multiple different mechanisms. Nonetheless, hypoxia inducible factors (HIFs) are the main mediators of hypoxic effects in the cell (9). HIFs were shown to primarily function as heterodimeric transcription factors that are comprised of one alpha and one beta subunit. Up to date, three HIF alpha (HIF1α, 2α, and 3α) and one common beta

(HIF1β, or ARNT) subunits were reported (3, 10-12). While alpha proteins are oxygen sensitive, ARNT is known to be constitutively expressed in cells and is independent of hypoxia (7, 13). HIF1α and HIF2α (as parts of HIF1 and HIF2 transcription factors, respectively) are known to control majority of the hypoxia-mediated responses in the cell. HIF3α does not form a functional heterodimer with the beta subunit, but was rather shown to form a complex with HIF1α preventing its ARNT binding (12, 14). Thus, HIF3α suppresses HIF1α transcriptional activity providing a switch to HIF2α-dependent transcription.

In normoxia (tissue oxygen tensions ranging from 3 to 10 % depending on the tissue, (14-16), HIFα subunits become hydroxylated by the oxygen-sensing enzymes prolyl hydroxylases (PHD1-3), which hydroxylate HIF alpha proteins at two proline residues in their oxygen-dependent degradation domain (15). The hydroxylated HIFs are then recognized by the von Hippel-Lindau ubiquitin ligase complex and targeted for proteasomal degradation. Figure 2 schematically summarizes oxygen mediated proteolytic regulation of the HIF alpha subunits.

In conditions of low tissue oxygen levels (equal or less than 1-2 %, (15) activity of PHDs becomes severely limited, resulting in the rescue of HIFα proteins from VHL-directed proteolysis and accumulation of HIFα. The respective alpha subunits translocate into the nucleus and then form a heterodimer with the constitutively present HIF1β, alternatively named aryl hydrocarbon receptor nuclear translocator (ARNT), to activate gene transcription by binding to hypoxia response elements, HREs (17-19).

It is also known that HIF proteins can undergo many other posttranslational modifications which cells utilize to fine-tune their functions (20-22). For example, another oxygen-dependent enzyme asparaginyl hydroxylase factor-inhibiting HIFα (FIH1) hydroxylates asparagine residue within the HIFα C-terminal transactivation domain (CAD) precluding its association with the essential coactivator CBP/p300

and resulting in repression of the HIFα transcriptional activity (23). Additionally, other types of modifications as SUMOylation, phosphorylation, and nitrosylation were reported to modulate HIF transcriptional activity, as well as numerous transcriptional coactivators and other interacting proteins that together provide cell and tissue specificity of HIF target gene regulation (21, 22, 24).

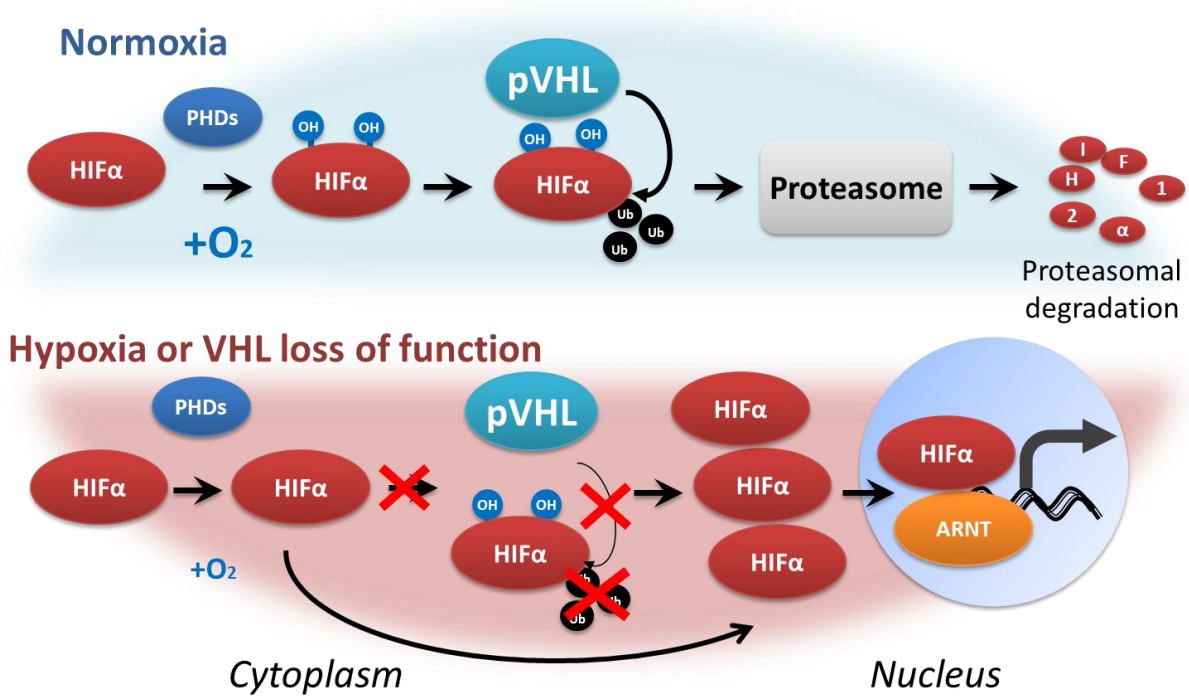

Figure 2. Oxygen-dependent and oxygen-independent mechanisms of regulation of the hypoxia inducible factors. In oxygen-rich conditions, HIFα is hydroxylated at proline residues by prolyl-4-hydroxylases (PHDs) and polyubiquitinated by the SCF ubiquitin ligase von Hippel–Lindau protein (pVHL). This leads to degradation of HIFα proteins by the 26S proteasome. In hypoxic conditions or VHL loss of function, HIFα is stabilized and translocates into the nucleus where it binds to its dimerization partner HIF1β to enhance the transcription of HIF target genes. Adapted from (20, 25).

1.2. Structural and functional features of HIFs

HIFs are believed to primarily function as heterodimeric transcription factors that induce transcription of downstream target genes by binding to hypoxia response elements (HREs, with the consensus core sequence A/GCGTG) in gene promoters and enhancers (26-28).

Historically, HIF1α was first described as the sole master regulator of the hypoxic response that ensures cell survival during a hypoxic stress. This misconception was probably due to the broad expression of HIF1α across many different human tissues, whereas HIF2α was initially identified as an endothelium-specific HIFα isoform (thus, its first name EPAS1 from the endothelial PAS domain protein) and was therefore considered to have a more specialized function than HIF1α (29). Decades of further studies showed that HIF2α is present in many other tissues, such as the brain, heart, lung, kidney, liver, pancreas, and intestines, suggesting that it also has a wider role in the hypoxic response (3). In the kidney, for example, HIF2α is expressed in renal interstitial fibroblasts, endothelial cells, and some glomerular cells, whereas HIF1α expression can be detected predominantly in tubular cells (10).

Interestingly, HIF proteins are restricted to metazoans with HIF1α being highly conserved across various phylogenetic groups, whereas HIF2α emerged much later in the course of evolution (30). HIFα subunits show highly conserved sequence homology in the bHLH (85 %), PAS-A (68 %) and PAS-B (73 %) domains (31). Schematic representation of the main protein domains of HIF1α, HIF2α and ARNT is depicted in Fig. 3.

N-terminal transactivation domain (N-TAD) that contains the region mediating DNA binding and interaction with ARNT, and C-terminal transactivation domains (C-TAD) of HIF1α and HIF2α show lower sequence homology between the

isoforms and appeared *de novo* in the process of evolution (30). Recent evidence shows that both N-TAD and C-TAD of HIFα subunits enable the interaction with various coactivators and other proteins, while N-TAD primarily determines HIFα specificity of target gene regulation.

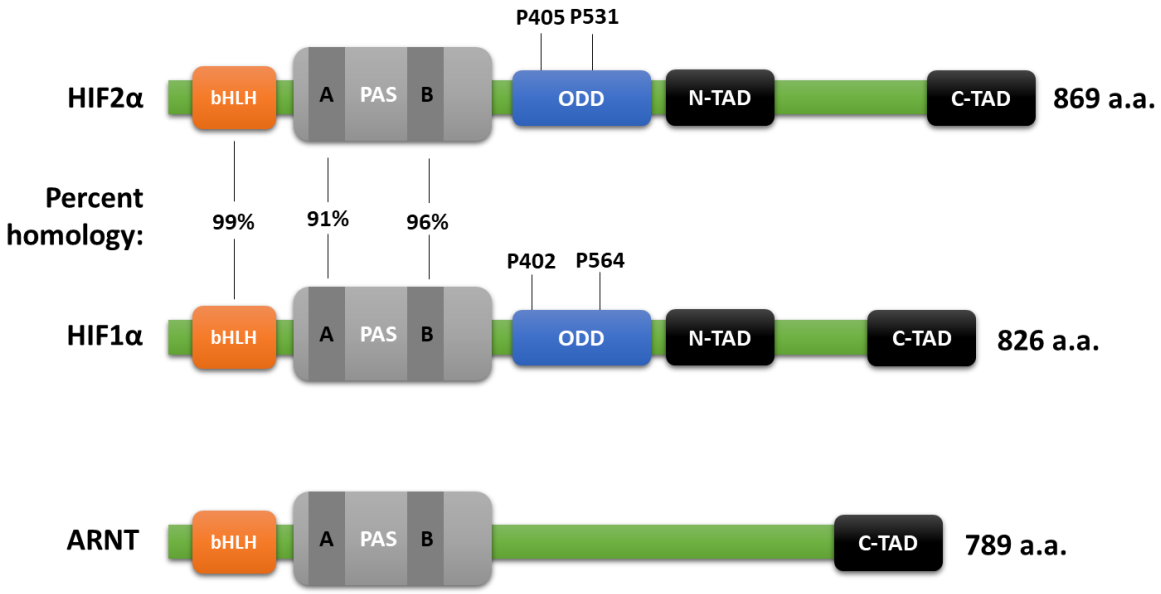

Figure 3. Protein structure of human HIF1/2α and ARNT. Both HIF1α and HIF2α contain basic helix-loop-helix (bHLH), per-ARNT-SIM (PAS), oxygen-dependent degradation domain (ODD), and C- and N-terminal transactivation domains (CADs). Prolyl hydroxylases (PHDs) hydroxylate proline residues at positions 402 and 564 in ODD of HIF1α, and 405 and 531 in ODD of HIF2α leading to the degradation of hydroxylated proteins by the proteasome. Numbers refer to amino acid similarity between human HIF1α and HIF2α in the defined domains. Modified from Hu et al., 2007 and Lee H. J. et al. 2019. (13, 27).

In a study by the group of Celeste Simon it has been shown that replacement of the N-TAD of HIF2α with the analogous region of HIF1α was sufficient to convert HIF2α into a protein with HIF1α functional specificity (13). Similar experiments with an exchange of the DNA binding domain (bHLH), dimerization domain, or C-TAD did not result in altering target gene specificity of HIFs. Nevertheless, both domains were shown to be important in target gene regulation: while N-TADs confer target gene selectivity by interacting with additional transcriptional

cofactors, such as the ETS transcription factor (13), C-TAD contributes to the regulation of most HIF target genes and is the stronger transactivation domain (24). In another phylogenetic study by Graham and Presnell C-TAD was reported to be required for overall high HIFα activity and interaction with transcriptional co-activators, for example CBP/300 – a well-known coactivator reported earlier by the group of Pereira (30, 32), or TAZ (33).

Because of the shared consensus DNA binding motif, HIF1 and HIF2 also have many common downstream target genes, expression of which is often cell context and tissue type dependent (11, 14, 26, 34-36). For example, HIF1 and HIF2 can both regulate vascular endothelial growth factor A (VEGFA) and the glucose transporter 1 (GLUT1), or erythropoietin (EPO). Interestingly, HIF1α alone was originally believed to promote the hypoxic induction of erythropoietin (EPO) by binding to the HRE in the EPO enhancer. Nevertheless, later it is was clearly shown *in vitro* and then also in mice that HIF2α not only can drive EPO production, but in fact is the predominant regulator (14). However, HIF1α and HIF2α can under some circumstances substitute one another: HIF2α has been shown to regulate enzymes of the glycolytic pathway in the absence of HIF1α, while HIF1α is capable of activating some matrix metalloproteases (MMPs), chemotaxis (CXCR4), or histone modifiers (JMJD) (10, 14).

Additional evidence of the unique and irreplaceable functions of the alpha isoforms came from the studies of embryos. Mice which are homozygous for a null allele at the locus encoding either HIF1α or HIF2α die by embryonic day 10.5 and 12.5, respectively. HIF1α null embryos develop with cardiac malformations, vascular defects, and impaired erythropoiesis, while HIF2α null embryos die due to vascular defects, bradycardia linked to deficient catecholamine production, impaired lung maturation, and vascular defects in the yolk sac and embryos (9, 31).

Recent evidence indicate that HIF1α and HIF2α exhibit mostly parallel or non-overlapping regulation of their target genes (35). However, other reports suggest that HIF1α and HIF2α can have more different then similar downstream target gene profiles as the result of unique patterns of distribution over the genome and interaction with various partners (7, 35). Interestingly, only nine genes were found by now to be inversely regulated by the two HIF isoforms, suggesting that alpha subunits indeed mostly cooperate in driving gene expression (35). In fact, antagonism between HIF1α and HIF2α was only described in the very few cases when both of the isoforms controlled target genes involved in the same cellular process, i.e. by controlling the expression of proteins with antagonistic functions (3, 21). For example, HIF1α and HIF2α exhibit antagonism in regulating mTOR signaling: HIF1α inhibits mTORC1 signaling by increasing autophagy under hypoxic stress conditions, whereas HIF2α stimulate mTORC1 to promote cellular proliferation in oxygen-deprived cells (37). Other examples of antagonistic pathways regulated by both alpha isoforms are the production of nitric oxide (NO) upon interferon gamma (IFNγ) stimulation in tumor-associated macrophages (38). It was shown that high levels of IFNγ lead to HIF1α-mediated expression of the inducible nitric oxide synthase (iNOS) and M1 polarization of macrophages (i.e. activation of their antitumor activity), while low IFNγ levels result in HIF2α-dependent activation of arginase 1 and M2 polarization of macrophages that exert pro-tumorigenic functions (37-39).

However, some of the most striking functional differences between the HIF isoforms were discovered in tumors which show a drastic variation in oxygen supply and thus even exhibit different types of hypoxia (40, 41). Thus, more advanced stage tumors and areas of growing tumors near the necrotic centers are characterized by chronic hypoxia that is primarily regulated by HIF2α, while tumor cells at the invasive front might experience fluctuating – intermittent – hypoxia

which is mostly associated with HIF1α (42, 43). Further investigations showed that expression of a particular HIFα isoform is also time-dependent: HIF1α expression typically peaks in the early phases of hypoxia, while HIF2α becomes the main isoform at later stages, a process that is in part regulated by the hypoxia-associated actor (HAF) (14, 36, 42, 44). In addition, clear evidence that HIF1α and HIF2α have functionally distinct roles come from the studies of neuroendocrine tumors and clear cell renal cell carcinomas (ccRCCs). Particularly, somatic gain-of-function mutations in the ODD domain of HIF2α were found in neuroendocrine tumors (45, 46). It has been shown that upregulation of HIF2α as the result of these mutations is associated with chemo- and radiotherapy resistance, and escape from immune surveillance (47). Interestingly, in renal cell carcinomas HIF2α was found to drive tumorigenesis, while introduction of HIF1α induced apoptotic cell death, hence in these tumors HIF1α is believed to function as a tumor suppressor (47-49). To better understand the focus of the current project, in the next section we will review in details main mechanisms of HIF action in tumor cells.

1.3. Diverse roles of the hypoxia inducible factors in tumor cells: evidence for transcriptional and non-transcriptional mechanisms of HIFα activity

1.3.1. Transcriptional role of HIFs

Transcription factors are often viewed as high-level molecular controllers of entire regulatory networks in cells since they can simultaneously impact the expression of multiple genes. Some transcription factors indeed have a wide range of downstream targets, e.g. c-Myc that is arguably the most versatile TF of all since it is reported to control the expression of up to 15 % of all human genes (50). Unlike c-Myc, HIFs do not have as many downstream target genes. Genome-wide analysis of the transcriptional response to hypoxia coupled to analysis of HIF DNA binding

revealed only a small proportion of genes that are under the control of these transcription factors, comprising from <1 % to 5 % of all genes depending whether the promoter regions or enhancers are being counted (10, 51). Nonetheless they were shown to control many critical features of cancer, such as neoangiogenesis (52, 53), glycolytic metabolism (54-57), autophagy (58, 59), apoptosis (55, 60, 61), cell cycle and proliferation (62-64), immune response (12, 39, 65-68), and tumor invasion and metastasis (34, 69-71).

Interestingly, as numerous investigations showed, HIFs can exert both tumor suppressive and tumor promoting effects (72-74). For example, HIF1α was shown to drive EMT and metastasis by directly regulating ZEB proteins in a mouse model of CRC which was further corroborated using colorectal carcinoma patient-derived xenografts (75). In another study, HIF1 was also shown to promote EMT via upregulation of Snail in gastric cancer (76). Another investigation focused on the role of HIFs in colorectal cancer showed that silencing of HIF1α results in reduction of primary tumor growth, which was opposite to the case of HIF2α targeting that resulted in increased primary tumor growth (73). On the contrary, in a study by Mazumdar at al. the authors show that depletion of HIF2α, but not HIF1α, in lung cancer results in a profound antitumor effect in the established *Kras*^{G12D}-driven non-small cell lung cancer (NSCLC) mouse model (77, 78). In yet another model of bone metastatic ccRCC, HIF2α but not HIF1α was found to be the predominant HIF isoform responsible for the hypoxia-mediated effects and significantly contributed to tumor growth and progression (79, 80). All of these seemingly controversial findings simply reflect the wide-ranging scope of transcriptional control by these master regulators and emphasize the need to analyze their function depending on the exact tumor type and context.

It is widely believed that most of the classic hypoxia-response genes (e.g. *VEGFA, GLUT1*) are induced by HIFα/ARNT heterodimers (9, 81). Nevertheless, several

recent studies showed alternative mechanisms how HIFs can regulate downstream genes independently of ARNT. In fact, many of the ARNT-independent effects were shown to be mediated by the N-terminal transactivation domain of HIF1/2α which also confers some target gene specificity in HIF1α and HIF2α (13). For example, HIF1α was shown to counteract c-Myc transcriptional activity by displacing c-Myc from promoters of *CDKN2A*, *hTERT*, and *BRCA1* resulting in a cell cycle arrest in HCT116 cells (62). Figure 4 summarizes some of the published HIF2α interaction partners and highlights their functional role.

Some of the alternative interaction partners can be shared by both isoforms. For example, HIF1α and HIF2α were both shown to interact with β-catenin (82, 83). The resulting HIF1α/β-catenin complex was then shown to reduce TCF4 binding to regulatory regions in some genes, such as MMP13 (83), while HIF2α/β-catenin promoted TCF4-driven transcription and proliferation in tumor cells (82).

1.3.2. Non-transcriptional functions of HIFs

Non-transcriptional functions of either HIF1α or HIF2α can explain the discrepancy between the limited HIF-mediated transcriptional response in terms of the number of HIF-regulated target genes on one hand and the huge versatility of the hypoxia driven processes on the other hand. In general, ARNT-dependent and ARNT-independent HIF1/2α-mediated transcriptional regulation has been extensively studied by now (summarized for HIF2α in Figure 4), while non-transcriptional roles of HIFs have only started to be explored. Recently transcription- and ARNT-independent roles of HIF1/2α have been reported to regulate cell cycle progression (84), protein synthesis (85, 86), and formation of adherens junctions and cell motility (87-90). For example, in a publication by the group of G. Semenza the authors showed that binding of HIF1α to Cdc6/MCM complex decreased phosphorylation and activation of the complex by the Cdc7

kinase resulting in stalling of replication forks and cell cycle arrest in hypoxic conditions (84).

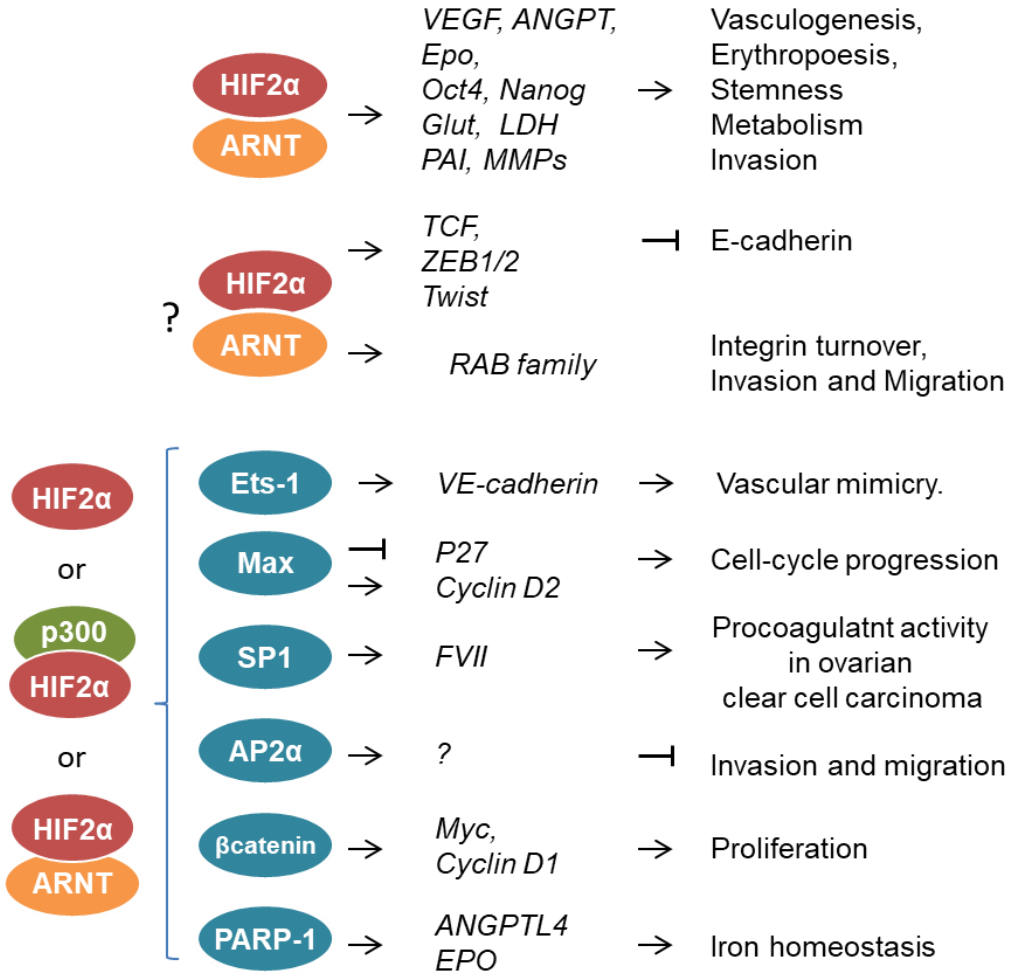

Figure 4. HIF2α interacting partners and the regulated downstream pathways. HIF2α dimerizes with ARNT and regulates the expression of canonical hypoxia-dependent genes which are responsible for angiogenesis, glycolysis, differentiation, and tumor cell invasion. However, HIF2α was also shown to form complexes with other transcription factors for which heterodimerization with ARNT or transactivation by p300 is optional. Such interactions define the context dependent transcriptional responses to hypoxia (64, 74, 82, 91, 92).

In another publication exploring the unconventional functions of HIFs, HIF1α was shown to interact with the enzymatic subunit of γ-secretase and augment its activity leading to increased Notch signaling (93). Moreover, this mechanism of hypoxia-mediated activation of Notch was shown to promote metastasis in breast cancer. Interestingly, by studying several HIF1α mutants that lacked the bHLH, N-TAD, or

C-TAD domains the authors could show that ARNT and DNA-binding by HIF1α was not required for the interaction with and activation of the γ-secretase. This finding was further supported by experiments with a pharmacological HIF1α inhibitor echinomycin which blocks the binding of HIFs to hypoxia-response elements, but that can also disrupt HIF1α/ARNT complexes: the authors showed that HIF1α was able to bind and augment γ-secretase activity even in the presence of the inhibitor.

Several other studies discovered HIFs to non-transcriptionally regulate ciliogenesis, an important process for maintaining stability of cell contacts and interaction of cells with the ECM (87, 94). Particularly, *VHL* inactivation was found to be associated with the loss of primary cilium in renal cysts as an early mark of RCC pathogenesis (94, 95), while *VHL* restoration or targeting of HIF1α, but not HIF2α, in RCC cells resulted in restoration of the cilia (95). It is believed that HIF2α can also regulates this process in an ARNT-independent and non-transcriptional manner since HIF2α protein was shown to be localized in the cilia during inflammation (96), however the exact mechanism remains elusive.

In comparison to HIF1α ARNT- and transcription-independent mechanisms of action, far fewer such mechanisms were described for HIF2α. Of these, the most interesting are studies published by the group of S. Lee linking HIF2α to protein synthesis regulation. The authors found that one of the mechanisms how tumor cells adapt to hypoxia is by a global repression of protein synthesis (97). Interestingly, the authors showed that HIF2α could overrule this repression and maintain translation of some genes by forming a complex with eIF4E and subsequent binding of this new heterodimer to HRE elements on mRNA (86).

In summary, HIF1α and HIF2α were shown to impact transcription of downstream target genes as parts of HIFα/ARNT and non-ARNT heterodimeric transcription

factors. Additionally, HIFs can regulate activity and stability of various interacting partners in a non-transcriptional manner.

Since hypoxia was shown to play a major role in the growth and progression of renal and colorectal carcinomas, in the next section we will explore HIF2α functions in these tumors.

1.4. Role of HIF2α in kidney cancer, colorectal carcinomas, and other hypoxia-driven tumors: clinical significance and potential for therapeutic exploitation

As discussed above, HIFs become primarily activated either in response to the tumor-associated hypoxia or by inactivation of the *VHL* gene. Clear cell renal cell carcinoma (ccRCC), which comprises 70 % of all renal tumors, is the classic example of a HIF-driven cancer (7, 28, 98, 99). Around 50 % of all ccRCC cases have impaired pVHL function due to various inactivating mutations or through epigenetic silencing of the *VHL* gene (Fig. 5). This results in constitutively activated hypoxia signaling with HIF2α being the predominant alpha isoform. Moreover, it was shown that in RCCs HIF2α acts as one of the key oncoproteins, whereas HIF1α is considered to function as a tumor suppressor and can activate apoptosis and is even frequently mutated or epigenetically silenced (80, 100-102).

Analysis of gene expression profiles in RCC tumors from patients with metastasis at initial diagnosis in comparison to patients without metastases revealed a significantly increased hypoxic signature in metastasizing tumors characterized by elevated mRNA levels of multiple HIF targets (Fig. 6, A).

A

Gene	Total number of mutations	Number of samples with one or more mutations	Frequency, %
VHL	**241**	**225**	**49,9**
PBRM1	141	138	30,6
ARAP3	38	25	5,5
SETD2	58	51	11,3
KDM5C	27	27	6,0
BAP1	42	40	8,9
MTOR	33	32	7,1
MUC4	129	77	17,1

B

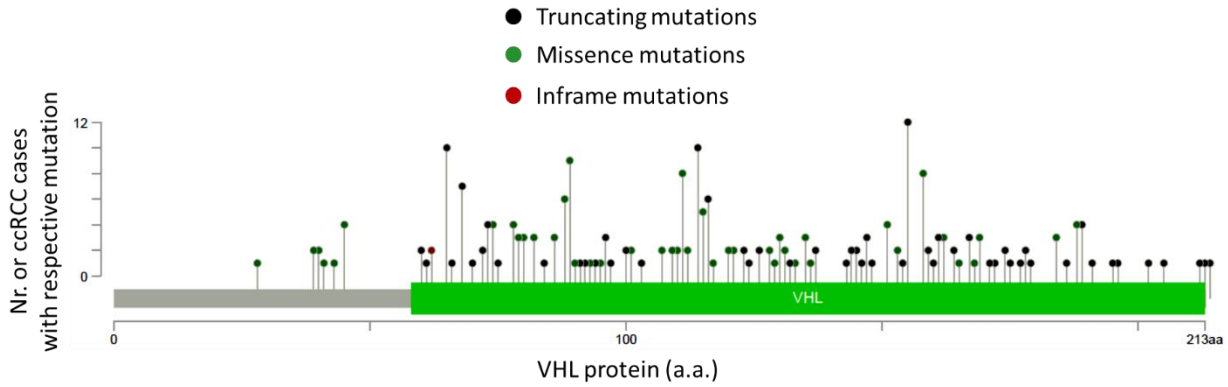

Figure 5. Inactivation of pVHL is the most common alteration in ccRCC. A. Approximately 50 % of all ccRCC patients harbor one or more inactivating mutations in the *VHL* gene (103). **B**. Significant portion of the remaining patients show severely decreased pVHL levels due to numerous inactivating mutations across the whole body of the gene, or other mechanisms, e.g. through epigenetic silencing by hypermethylation of the *VHL* promoter.

However, despite the correlation between pVHL loss of function with poor prognosis and decreased overall survival in ccRCC patients, inactivating mutations in the *VHL* gene did not correlate with metastasis in these patients (98). This highlights the point that it is not pVHL loss itself, but other factors, like HIF2α signaling, that are driving metastasis in ccRCC.

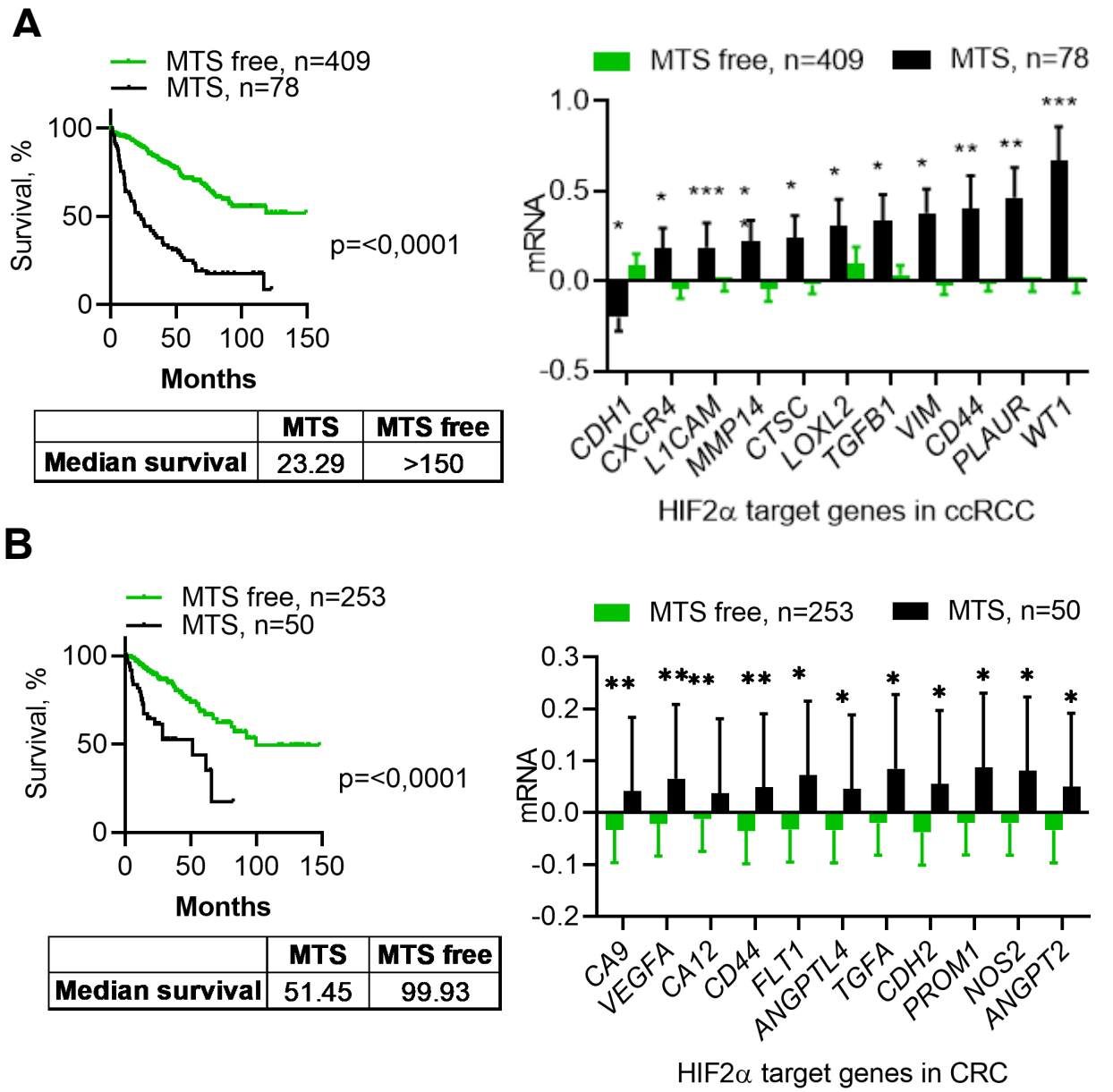

	MTS	MTS free
Median survival	23.29	>150

	MTS	MTS free
Median survival	51.45	99.93

Figure 6. Correlation between tumor metastasis and the hypoxic gene signature in kidney and colorectal cancer patients. Patients with metastatic ccRCC (**A**) or CRC (**B**) show decreased survival and increased hypoxia signature as shown by mRNA levels of typical hypoxia response genes. Survival and gene expression data from respective patient cohorts in the TCGA database were extracted using the c-bio portal.

Realization of the fact that loss of pVHL significantly alters the intracellular signaling in RCC cells (e.g. by activation of the hypoxia signaling), several synthetic lethality approaches have been developed to exploit this vulnerability in kidney cancer. For example, in a study by the group of William Kaelin it has been

shown that pVHL-defective ccRCC cells are hyperdependent on the H3K27 methyltransferase EZH1 for survival. The authors employed an shRNA screen and identified two enzymes demethylase KDM6 and methyltransferase EZH1 that control reciprocal reactions: demethylation and trimethylation of lysine K27 on the histone H3, respectively. Targeting of EZH1 preferentially killed VHL-deficient RCC cells due to their dependency on HIF2α-driven histone demethylase activity (104). In another study an shRNA screen in ccRCC cells identified a synthetic lethality between CDK4/6 and VHL inactivation. The authors observed synergistic suppression of renal cancer cell growth when using a CDK4/6 inhibitor in combination with a HIF2α inhibitor (105). Additionally, a recent CRISPR/Cas9-mediated screen revealed pVHL loss of function to form a synthetic lethality pairs with two other pathways: DNA damage response and selenocysteine biosynthesis (106). Cells deficient for VHL have dysfunctional mechanisms of dealing with reactive oxygen species (ROS) and develop a greater dependence on selenoproteins in coping with the imbalanced cellular ROS levels for survival. Genetic targeting of selenoproteins resulted in efficient elimination of VHL deficient renal cancer cells, though specific chemical inhibitors against selenoproteins have not been used in this study. In addition, authors showed that pVHL loss induces DNA damage related stress and conveys a strong reliance on DNA double strand break repair mechanisms (DDR) for survival. Hence, targeting DDR pathways with small molecule inhibitors of AURKA, AURKB, ATR, CDK1, or TOP2A inhibited growth of cells deficient for VHL. Lastly, inhibition of lysosomes was also shown to form a synthetic lethality pair with pVHL loss of function as described by Turcotte S. et al, 2008. Specifically, the authors could show that cells with pVHL inactivation are unable to maintain their lysosomes at the perinuclear localization in response to the treatment with STF-62247 (4-pyridynil-2-anilinothiazole) which was identified in a massive screen of 64’000 compounds. STF-62247 is a potent

blocker of late stages of autophagy through inactivation of lysosome restoration and disruption of their integrity which was suggested to be controlled by the VHL protein (107).

Similar to identified synthetic lethality pairs with pVHL loss of function, HIF2α-overexpressing tumor enteroids were reported to show significantly increased sensitivity to oxidative cell death activators via induction of ferroptosis that is characterized by the loss of lipid peroxide repair capacity (108). These results are supported by the observations that activation of HIFs during hypoxia leads to upregulation of lipid regulatory genes in colon cancer cells. In line with these results, treatment of colon cancer cells and enteroids with the hypoxia mimetic FG4592 (Roxadustat) accompanied with ferroptosis activators such as erastin, RSL3, sorafenib, or dimethyl fumarate resulted in robust cell death in a dose- and time-dependent manner (108).

Beyond kidney tumors, high expression of hypoxia target genes was observed in also in metastatic colorectal carcinomas (CRC), as shown in Fig. 6, B. Particularly, in these tumors hypoxia was shown to be a major regulator of tumor angiogenesis mostly due to the transcriptional upregulation of VEGFA (109-111).

Similar to RCC and CRC tumors, HIF2α was also shown to function as an oncoprotein in several other infrequent tumor entities as polycystemias, paragangliomas and pheochromocytomas. Curiously, in these tumors HIF2α accumulation is not the result of *VHL* loss, but rather due to stabilizing mutations in the HIF2α ODD domain (45-47, 49).

There is additional evidence showing that HIF2α is important for the development and progression of many other types of cancer, such as melanoma, T-cell leukemia, colon, pancreatic, and lung cancer (34, 70, 77, 108, 112-114). Moreover, HIF2α was also shown to be regulating epithelial-to-mesenchymal transition (EMT) and hence contributes to metastasis across different tumor types (52, 112).

In summary, numerous reports presented exhaustive clinical and experimental evidence that hypoxia signaling presents an attractive target for the development of new therapeutic approaches for the treatment of hypoxia-driven tumors. Importantly, HIF2α as the dominant isoform in ccRCCs and because of its key oncogenic role in these tumors is an especially attractive target for inhibition. Therefore, in the next section we will review the current approaches to targeting hypoxia, and more specifically – HIF2α.

1.5. Pharmacological inhibition of HIFs as treatment for patients with hypoxia-driven cancers

Early realization of the significant role that HIFs play in tumor development and progression led to focused efforts to develop specific inhibitors targeting HIFs or HIF-driven pathways (17). Over the years several classes of such inhibitors have been developed and studied as monotherapy or in combination with other agents aimed at the treatment of advanced or refractory cancers. There are two major categories of HIF inhibitors: 1) direct HIF inhibitors which affect the expression or function of the HIF proteins; and 2) indirect HIF inhibitors that regulate upstream or downstream pathways which ultimately affect HIF signaling (e.g. mTOR, HDAC, and various tyrosine kinase inhibitors) (7, 17). Most of the HIF inhibitors that were also used in clinical studies target both transcription factors, which makes it impossible to discriminate the contribution of individual HIFα isoforms to tumor invasion and metastasis. However, several HIF2α selective inhibitors have been recently developed and even tested in first clinical trials.

Of all inhibitors targeting tumor hypoxia, two types of selective HIF2α inhibitors were described:

1) a small-molecule inhibitor that blocks HIF2α translation (115, 116);

2) several small-molecule inhibitors (e.g. PT2385 and PT2399) that disrupt the HIF2α/ARNT heterodimer (81, 117, 118).

A brief overview of the main HIF inhibitors is summarized in Table 1.

Importantly, several of the small molecule inhibitors which target the HIF2α/ARNT heterodimer (PT2385, PT2399, and PT2977) were shown to efficiently downregulate many of the known hypoxia response genes and reduce tumor growth in preclinical cancer models of ccRCC. On the basis of these findings these compounds were granted further testing in phase I and II clinical trials (17).

Table 1. Summary of the key feature of HIF2α-specific inhibitors

Inhibitor, Primary mechanism of action	**Phase of clinical trials/ Preclinical models tested**	**Reference / Clinical trial number**	**Clinical application/ Result of preclinical studies**
PT2385, first of the class of HIF2α/ARNT inhibitors	II	NCT03108066	RCC patients with a loss of pVHL who have no evidence of metastatic disease
	II	NCT03216499	Recurrent glioblastoma with the primary endpoint of radiographic tumor response
	I, dose escalation. Combination of PT2385 with nivolumab (PD-1 inhibitor) and cabozantinib (VEGF TKI)	NCT02293980	Metastatic RCC
PT2977, second-generation HIF2α/ARNT inhibitor	II	NCT03401788	*VHL*-associated RCCs with no evidence of metastatic disease
	PT2977 with cabozantinib (a VEGF tyrosine kinase inhibitor)	NCT03634540	Advanced RCCs with clear cell morphology
Compound 76, HIF2α mRNA inhibitor	Zebra fish	(116)	Reversed the compromised cardiac contractility of $VHL^{-/-}$ embryos and partially rescued early lethality in $VHL^{-/-}$ zebra fishes

Inhibitor, Primary mechanism of action	Phase of clinical trials/ Preclinical models tested	Reference / Clinical trial number	Clinical application/ Result of preclinical studies
Small molecule inhibitors of HIF2α translation (Compounds 46, 76, and 77)	786O ccRCC cells, WT8 B-lymphoblastoid cell line, PC3prostate adenocarcinoma	(115)	Decreased HUVEC proliferation after treatment with conditioned tissue culture medium from compound-treated cells
HIF2α-RGD-DPC, RNA interference	A498 cells orthotopically transplanted in nude mice	(100)	Decreased primary tumor growth and reduced passive lung metastases after tail vein injection

Interestingly, in a recent report it was found that PT2385-treated neuroblastoma PDX cells show a virtually unaffected transcriptome profile compare to control cells, indicating that either HIF2α/ARNT dissociation is incomplete or that HIF1α effectively compensates for HIF2α transcriptional deficiency in these tumor cells (119). In some other studies the authors reported the development of resistance to HIF2α/ARNT inhibitors by acquisition of mutations in the *EPAS1* gene (104, 120). Despite the fact, that targeting HIF2α transcriptional activity with small molecule inhibitors showed some promising results in controlling RCC primary tumor growth, none of the published reports investigated the impact these compounds might have on tumor cell migration and invasion. Total lack of this data in the literature is especially puzzling since patients with metastatic RCC tumors show a significantly worse overall survival and are faced with limited treatment options in comparison to patients with non-metastasizing kidney tumors. Therefore, in the current study we aimed to address this gap in the current understanding of HIF2 inhibition in RCC invasion and metastasis. Moreover, since HIF2α was reported to efficiently interact with multiple proteins, we explored the possibility of a synthetic lethality for inhibiting RCC invasion. In particular, since many of the alternative interacting partners of HIF2α are linked to epigenetic regulation of gene

expression, next section presents a short overview of the connection between HIF signaling and epigenetics.

1.6. Epigenetic repressor complex PRC2 cooperates with hypoxia signaling to promote RCC progression and metastasis

Connection between epigenetics and hypoxia became evident from several observations. As it was mentioned before, physiological hypoxia constitutes a part of the normal microenvironment during embryonic development where HIFs drive cell differentiation and determine cell fate (40). Also, it was found that hypoxia is necessary for the maintenance of embryonic cells *in vitro* (121). Epigenetic inheritance involves reversible changes of chromatin by acetyl, methyl, phosphoryl groups which are catalyzed by histone modifying enzymes. N-terminal tails of core histones undergo covalent modification by acetylation of lysines, methylation of arginines and lysines, phosphorylation of threonines and serines, ADP-ribosylation of glutamic acids, ubiquitylation and sumoylation of lysines. Histone lysin acetylation, a mark of the euchromatin, is balanced by histone acetyltransferases (HAT, for example p300/CBP HAT) and histone deacetylases (HDAC), both of which can directly interact with HIFs and facilitate HIF transcriptional activity serving as co-activators (23, 122-124).

Exploration of the crosstalk between different epigenetic modifiers and HIFs lead to the discovery of a unique role of DNA methyltransferases and histone demethylases in the tumor hypoxic response. For example, epigenetic silencing of the erythropoietin gene by DNA methylation at the CpG island at its promoter was shown to be a maladaptive response to chronic (sustained) and intermittent hypoxia (43). It has been discovered that different histone demethylases, particularly JmjC/KDMs, which together with PHDs comprise a large group of 2-oxoglutarate

(2-OG)-dependent dioxygenases, are mediators of hypoxia-driven epigenetic changes in multiple tumors. Being direct oxygen sensors with very low Km values for O_2, demethylases quickly adapt to hypoxic conditions and work independently of HIFs as was shown by *in vitro* experiment with short term hypoxia (125). However, under long term hypoxia protein levels of these enzymes increase, which is the result of HIF-driven transcription of their genes, and comprises an important compensatory mechanisms of adaptation to low oxygen levels in the cell (51).

During tumorigenesis, HIFs are known to cooperate with PcG components of the polycomb repressor complexes 1 (PRC1) and 2 (PRC2) (126-129). Polycomb group proteins (PcG) are evolutionarily conserved epigenetic regulators that mediate gene silencing via trimethylation of lysine 27 of the histone H3 by PRC2 followed by lysine K119 ubiquitination of the histone H2A by PRC1(130).

Most of the studies show that tumors upregulate the repressive H3K27me3 and that global H3K27me3 reprogramming is a hallmark of cancer (131). Tumor cells achieve this by decreasing demethylase activity in response to insufficient oxygen in the microenvironment or by enhancing activity/expression of the components of the polycomb repressor complex 2 (104, 132-136). EZH1, which is the core enzymatic subunit of PRC2, was shown to correlate with the tumor stage in ccRCCs (104). Moreover, functions of its paralog EZH2 are also altered in many tumors. It was shown, that EZH2 knockdown strongly affects global H3K27me2/3 levels, whereas EZH1 knockdown was shown to only marginally affect this phenotype (131, 137-140). A simplified scheme of the canonical (within the PRC2 complex) and non-canonical (PRC2-independent) EZH2 functions is depicted in the Figure 7.

Canonical function of EZH2 is expressed by mono-, di-, and trimethylation of histones H3, which leads to gene repression. EHZ2 mediates repression of many tumor suppressors, such as transcriptional repression of the metastasis suppressor

RKIP in breast and prostate cancer (141), or is involved in maintenance of the silenced state of tumor suppressor loci, such as *INK4A*^{ARF} or *P21* (136) (135, 141, 142).

Interestingly, EZH2 protein levels in the tumor tissue, but not H3K27me3 levels, were suggested to have a prognostic value and inform treatment decisions for patients with late-stage renal cell carcinoma (143). This might be due to the dual role of EZH2 as was reported in many studies (129, 144-146). Despite the fact, that the most recognized role of EZH2 is to repress tumor suppressors, it has been also reported to act as a direct transcriptional co-activator (130, 132). In addition, EZH2 was shown to be capable of methylating other proteins than histones and thus to control adhesion and migration of cells (147-149).

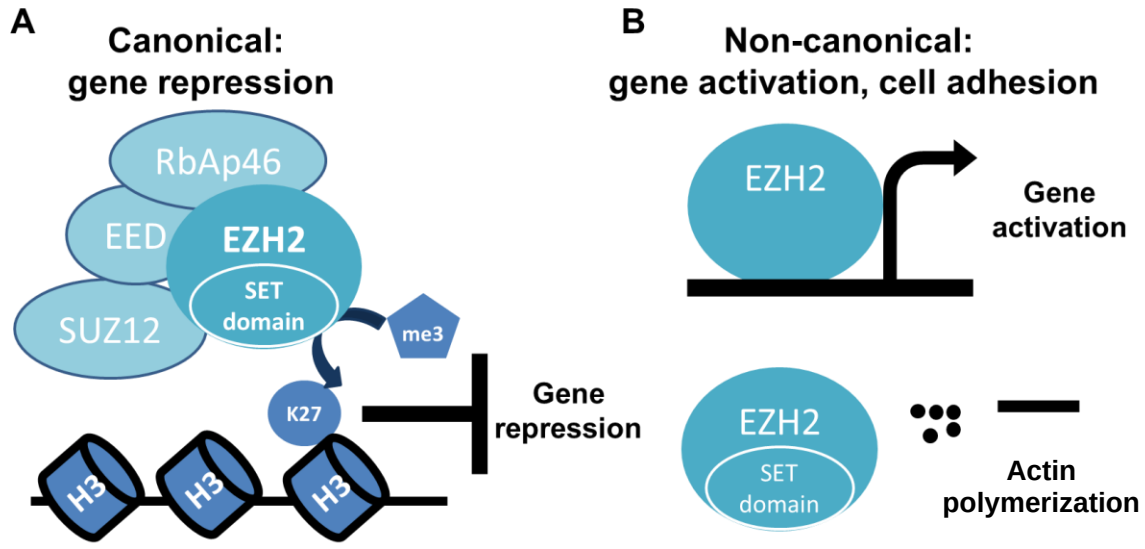

Figure 7. Canonical and non-canonical functions of EZH2 in gene regulation. A. EZH2 is the enzymatic component of PRC2 and primarily mediates the repression of genes by trimethylation of histone H3 at lysine 27. Acquisition of such a mark leads to chromatin condensation and gene silencing (135, 146). **B.** EZH2 is also known to function as a co-activator of gene transcription, regulator of actin polymerization and methylation-dependent turnover of adhesion proteins (130, 134, 145, 148, 150).

Accumulated evidence indicates the importance of the extra nuclear EZH2, hence its non-canonical functions in tumor progression. Particularly, it was established

that increased expression of EZH2 in prostate and breast tumors contributes to their metastatic capacity via regulation of actin-dependent cell adhesion and migration (150, 151). As shown by the group of I-hsin Su, EZH2 mediates Talin1 methylation and cleavage through interaction with VAV1, thereby enhancing the turnover of adhesion proteins and promoting tumorigenesis (147, 148, 152). This mechanism was also shown to contribute to leukocyte migration and induction of immune tolerance (147, 152).

The exact role of the other PRC complex, PRC1, is much less investigated. Until present, a few studies showed that HIFs upregulate the expression of the core PRC1 component BMI1 leading to induction of EMT in proximal tubular cells of the kidney (126). Additionally, combined targeting of EZH2 and BMI1 proved to be significantly more effective in managing severely hypoxic glioblastoma tumors than either monotherapy (127).

Overall gene transcription in hypoxia was shown to be tightly regulated by balancing methylation, demethylation and acetylation events that are maintained by the crosstalk between demethylases, polycomb group protein (PcG) methyltransferases, and histone acetylates (51, 122, 123, 131, 153, 154).

In summary, hypoxia and particularly HIF2α were shown to play a significant role in cancer progression and metastasis, especially in hypoxia-driven tumors as ccRCC. Both transcriptional (ARNT-dependent) and non-transcriptional (ARNT-independent) mechanisms of action are responsible for the pro-tumorigenic functions of HIF2α which results from the many interactions of the protein with different co-activators. Moreover, HIF2α was shown to be able to epigenetically reprogram tumor cells, although exact mechanisms how HIF2α signaling is regulating particular features of tumor cells, e.g. invasion, remain largely elusive.

1.7. Objectives of the study

Heterodimeric hypoxia inducible transcription factors were shown to control majority of the response mechanisms of cells to an oxygen-deficient microenvironment. Despite their significance in normal physiological processes, HIFs are known to control various aspects of tumor growth, as neoangiogenesis, glucose metabolism, proliferation, self-renewal, immune response, and importantly – tumor migration and invasion. In RCCs HIF2α, but not HIF1α, was shown to play a significant role in tumor development and progression, thus recently a novel class of inhibitors was developed that disrupts the formation of functional HIF2α/ARNT heterodimers. However, first clinical trials with these inhibitors did not prove to be successful. Moreover, up till now no data is available on the impact of these inhibitors on RCC tumor cell invasion and metastasis.

Considering the current absence of any EMA/FDA approved drugs that could prevent metastasis formation and the poorly studied role of HIF2α in RCC tumor cell invasion and metastasis, we set out the following aims for this project:

1. Investigate HIF2α-dependent mechanisms contributing to tumor cell migration and invasion.
2. Assess novel inhibitors that disrupt the HIF2α/ARNT heterodimer for their ability to block tumor cell invasion.
3. Explore alternative transcriptional and non-transcriptional mechanisms by which HIF2α controls invasion in hypoxia-driven tumors.
4. Identify possible targets for development of new therapeutic approaches to prevent HIF2α-mediated tumor cell invasion and metastasis.

2. Results

2.1. Invasion of ccRCC tumor cells is dependent on HIF2α

2.1.1. Overexpression of pVHL leads to degradation of HIF2α and decreased invasion in ccRCC cells

To study the mechanisms underlying HIF2α-dependent tumor invasion and metastasis we utilized a set of ccRCC lines (68, 155-157) (kindly provided by Prof. Almut Schulze) in which HIF2α was constitutively expressed due to the VHL loss of function in the control lines, and a similar set of lines where a functional pVHL was reconstituted. *HIF1A* is frequently not expressed due to chromosome 14q deletions commonly occurring in ccRCC resulting in complete loss or significant reduction in HIF1α protein levels (81, 100, 157). Reconstitution of the pVHL in these cells resulted in a very efficient degradation of HIF2α as shown by immunoblotting (Fig. 1A). In further experiments we focused on two ccRCC cell lines from the panel: A498 and 786O renal cell carcinomas which were published to be efficiently growing *in vivo* (81, 98, 100, 117). First, we tested the invasion potential of these cells in an *in vitro* modified Boyden chamber invasion assay. The ability of cells to invade through the basement membranes is critical to a number of important biological processes, such as cell metastasis, embryo implantation during early development, and inflammation (158, 159). In the Boyden chamber assay invasive cells secrete proteases that enzymatically degrade the matrigel matrix which enables the invasion through the pores of a PET membrane along the FBS gradient. Cells that successfully passed through the membrane are fixed and their nuclei stained with DAPI, which is used to estimate cell numbers. To exclude any artifacts coming from unequal seeding, pictures of the upper chamber are taken to normalize the number of invaded cells. Thus, when we tested our ccRCC lines in this assay a significant reduction in the invasion of cells upon pVHL reconstitution

was observed, in accordance with the significantly decreased HIF2α levels (Fig. 1B).

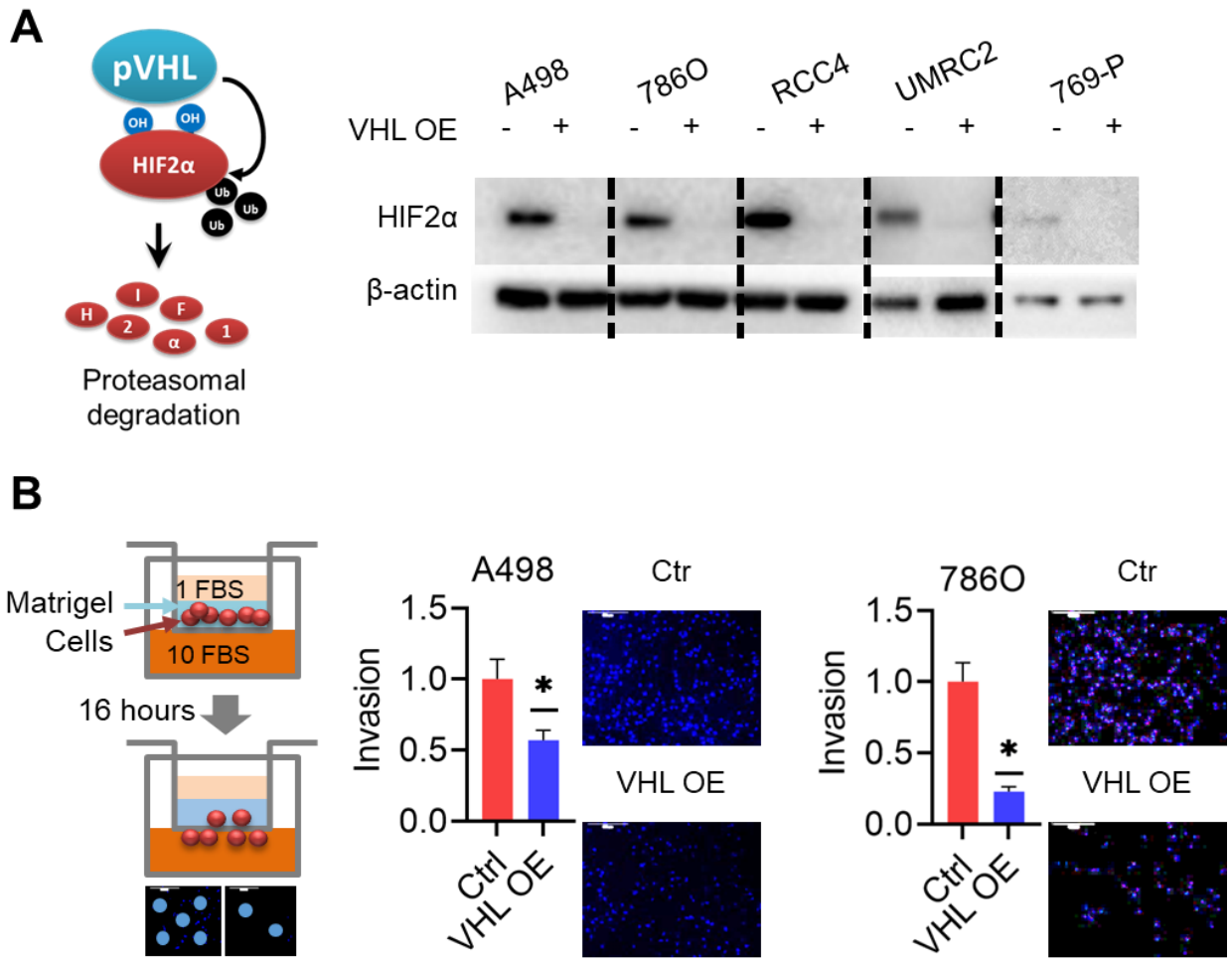

Figure 1. Reconstitution of pVHL in ccRCC cells leads to accumulation of HIF2α and decreased invasion. A. Reconstitution of ccRCC cells with pVHL leads to degradation of HIF2α. Protein lysates from ccRCC cells with stably reconstituted pVHL were subjected to immunoblotting for HIF2α levels. **B.** Boyden chamber matrigel invasion assay (scheme, left) showed significant reduction in invasion of ccRCC cells upon pVHL reconstitution. Scale bars 500 µm. Error bars represent standard error of the mean of three biological replicates. Representative pictures of at least three independent repeats.

2.1.2. Silencing of HIF2α suppresses invasion of ccRCC cells similar to pVHL reconstitution

Next, we assessed whether invasion of RCC cells depends on HIF2α or other pVHL targets. For this, we generated A498 cells where HIF2α was targeted with an shRNA. Then, we compared invasion of A498 cells overexpressing the shRNA against HIF2α to non-silencing shRNA (control) in wild type and VHL-reconstituted cells (Fig. 2A).

We could observe a significant reduction in HIF2α protein as well as some well-known HIF2α downstream targets, like glucose transporter GLUT1 or epidermal growth factor receptor (EGFR), as shown by immunoblot analysis (Fig. 2A).

In addition, real-time qPCR revealed a strongly decreased expression of HIF2α downstream target genes (including several known EMT markers), such as VEGF, PAI, and E-cadherin, upon HIF2α knockdown (Fig. 2B). Importantly, targeting of HIF2α resulted in a significantly reduced invasion which was comparable to that of pVHL-reconstituted cells (Fig. 2C). Overall, these data suggest that invasion of ccRCC cells primarily depends on HIF2α and is reduced upon downregulation of HIF2α.

2.2. Disruption of the HIF2α/ARNT heterodimer does not impact invasion or migration of tumor cells

2.2.1. HIF2α/ARNT inhibitors PT2385 and PT2399 have no effect on invasion of ccRCC cells

Recently developed HIF2 inhibitors that disrupt HIF2α/ARNT heterodimerization and dissociation of the transcription factor from the chromatin were shown to block downstream target transcription, efficiently reduce colony formation, and primary tumor growth *in vivo* (81, 117). To assess if such inhibitors would also impact

invasion, we treated ccRCC cells with PT2385 and the next-generation compound, PT2399, and tested the cells in a modified Boyden chamber matrigel assay as described in section 1.1.

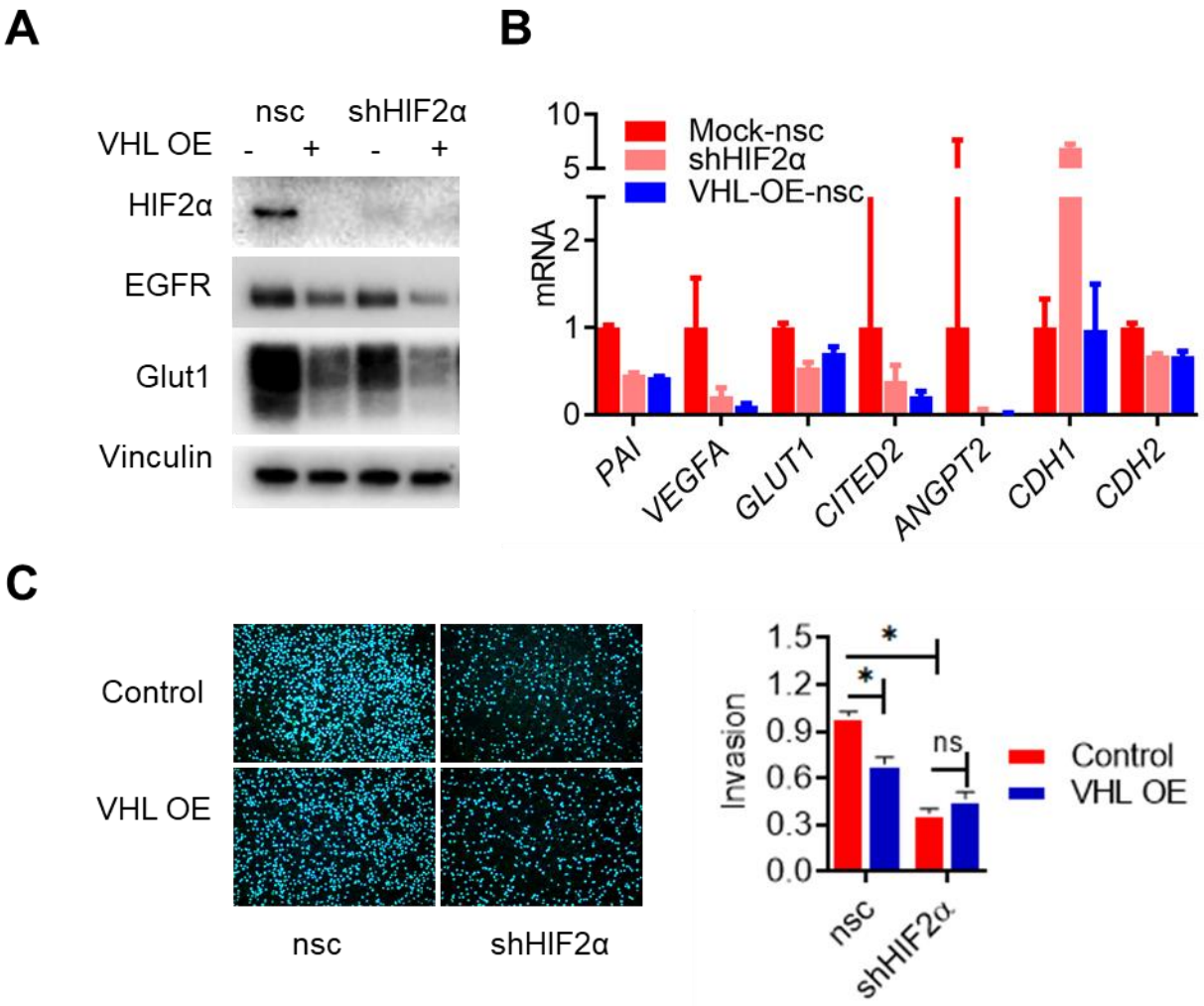

Figure 2. Silencing of HIF2α reduces invasion in ccRCC cells to the level of cell with VHL reconstitution. A. Immunoblots of total cell lysates from A498 cells expressing a non-silencing control (nsc) or an shRNA against HIF2α showing significant downregulation of HIF2α and its downstream targets. **B.** Targeting of HIF2α with shRNA in A498 cells results in reduction of downstream target gene expression comparable to cells were HIF2α is degraded due to VHL reconstitution. Error bars represent technical replicates. **C.** Boyden chamber matrigel invasion assay results with cells harboring an shRNA against HIF2α and VHL reconstitution. Knockdown of HIF2α significantly reduces invasion of A498 cells comparable to the level of VHL-overexpressing cells. DAPI-stained nuclei, scale 500 µm. Error bars represent standard error of the mean from replicates.

Inhibitor-treated cells were compared to pVHL-reconstituted lines as a relevant HIF2α-deficient condition as a positive control. We found that PT2385 could not reduce invasion *in vitro* compared to pVHL-reconstituted cells (Fig. 3A, B). The next generation inhibitor PT2399 also had no effect on invasion (Fig. 3C).

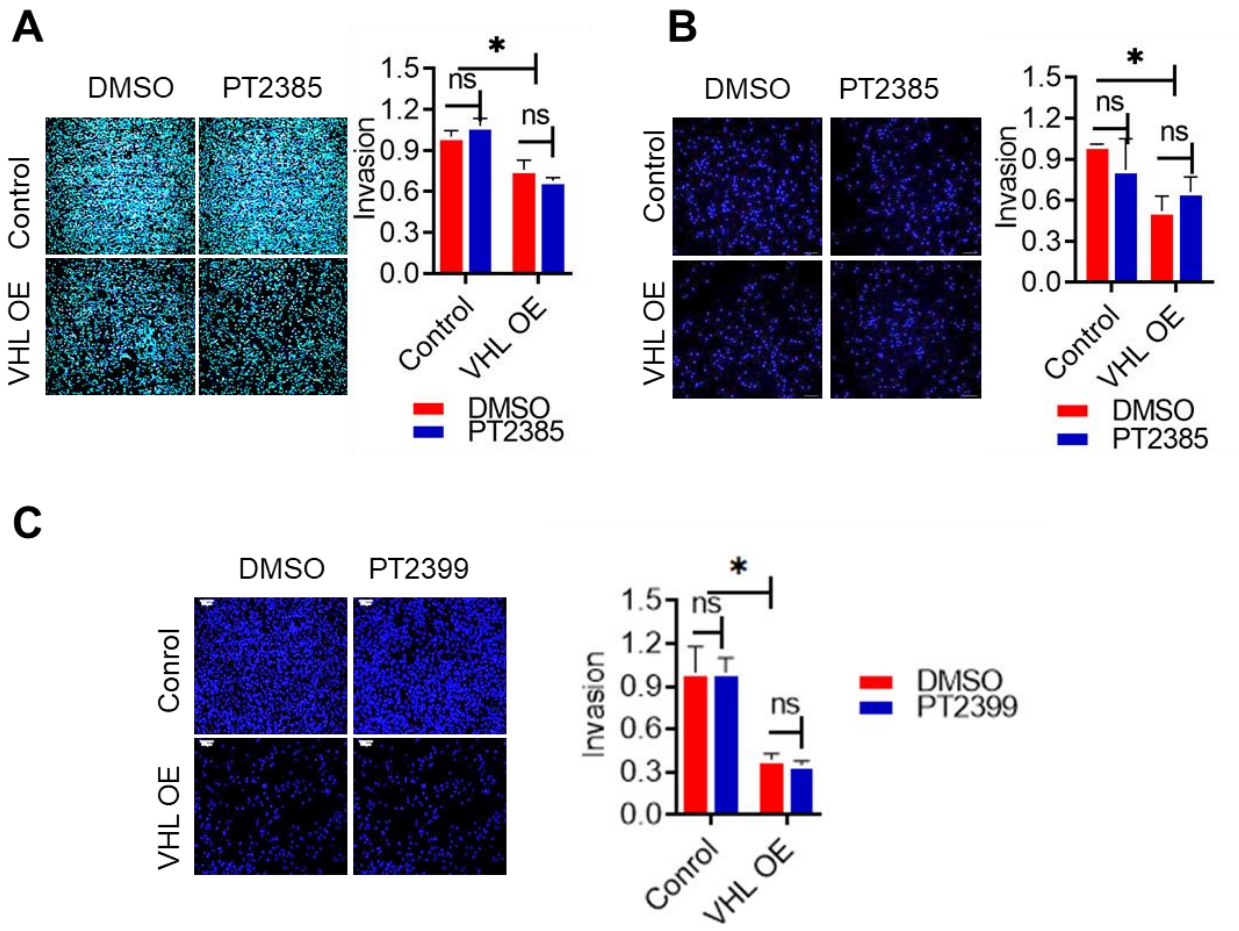

Figure 3. Targeting of HIF2 with HIF2α/ARNT inhibitors does not suppress invasion. **A.** A498 control cells and cells with pVHL reconstitution upon treatment with PT2385 (for 48 h with 0.5 μM) showed no change in their invasion capacity. Error bars represent standard error of the mean of three replicates. Representative results of at least three independent experiments. **B.** Similar to A498 cells, 786O ccRCC cells with or without pVHL reconstitution showed no changes in invasion upon PT2385 treatment. **C.** Control or VHL-reconstituted 786O cells were treated with the next generation HIF2α/ARNT inhibitor, PT2399, and subjected to the modified Boyden chamber matrigel assay. No changes in invasion were observed even upon treatment with relatively high concentrations of the compound (5 μM). Scale bars 500 μm. Error bars represent standard error of the mean of the technical replicates.

Additionally, we tested whether PT2385 could affect migration of A498 cells in a wound healing migration assay (Fig. 4). We found that migration of A498 cells with reconstituted pVHL was significantly reduced compared to the control cells overexpressing the empty vector treated with DMSO or PT2385. Over the same period of time, migration of A498 cells treated with the PT2385 inhibitor was similar to the control (DMSO), suggesting that PT2385 has no effect on cell migration. These observations indicate that disruption of the HIF2α/ARNT heterodimer does not lead to decreased invasion, suggesting that such inhibitors might have only a partial therapeutic effect on metastasis.

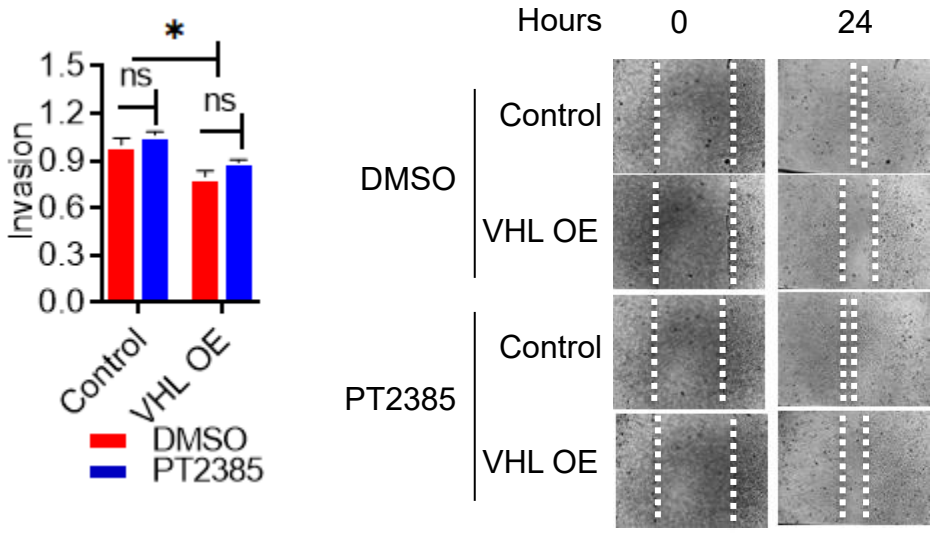

Figure 4. Inhibition of HIF2α with the PT2385 HIF2α/ARNT inhibitor does not affect migration of RCC cells. A498 control and VHL-overexpressing 768O cells were tested for migration in the wound healing assay. Cells were pretreated with 0.3 μM PT2385 for 24 hours prior to wound generation and kept in medium with the inhibitor for the duration of the assay. Error bars represent standard error of the mean of three replicates. Quantification represents one of three independent experiments.

2.2.2. HIF2 inhibitor disrupts the heterodimer, but only partially represses transcriptional downstream targets

To assess the extent of HIF2α/ARNT heterodimer disruption by PT2385, A498 and 786O cells were treated with increasing concentrations of the compound. Immunoprecipitation with subsequent immunoblotting showed efficient dissociation of the heterodimer even at relatively low concentrations (0.2-0.5 μM) which is in line with the published reports (117) (Fig. 5A). Next, we tested if inhibitor treatment would impact the expression of some well-known HIF2α downstream target genes. For this, we compared mRNA expression of those genes in cells after the treatment with relatively low or high concentrations of PT2385 compared to two controls: DMSO-treated cells and the pVHL-reconstituted line (Fig. 5B).

We observed that expression of *VEGFA* and *GLUT1* in A498 cells, and *VEGFA, OCT4*, *CCND1*, *ANGPT1*, and *PAI* in 786O cells (Fig. 5C) was decreased upon PT2385 treatment, with mRNA levels similar to those in the pVHL-reconstituted cells (Fig. 5B). Surprisingly, some of the well-cited HIF2α downstream targets which are known to regulate EMT, as *CYPA* and *CDH1* in 786O cells, or *MMP9* and *MMP13* in A498 cells, did not at all respond to PT2385 treatment. Moreover, we found that treatment with higher concentrations of the compound did not further suppress transcription of most of the genes. These observations suggest that the HIF2α-dependent transcriptome is much wider and is not restricted to the HIF2α/ARNT heterodimer. Thus, we might speculate about the existence of alternative ways how HIF2α regulates downstream target gene expression in addition to the well-studied ARNT heterodimer-dependent mechanisms of HIF2α action.

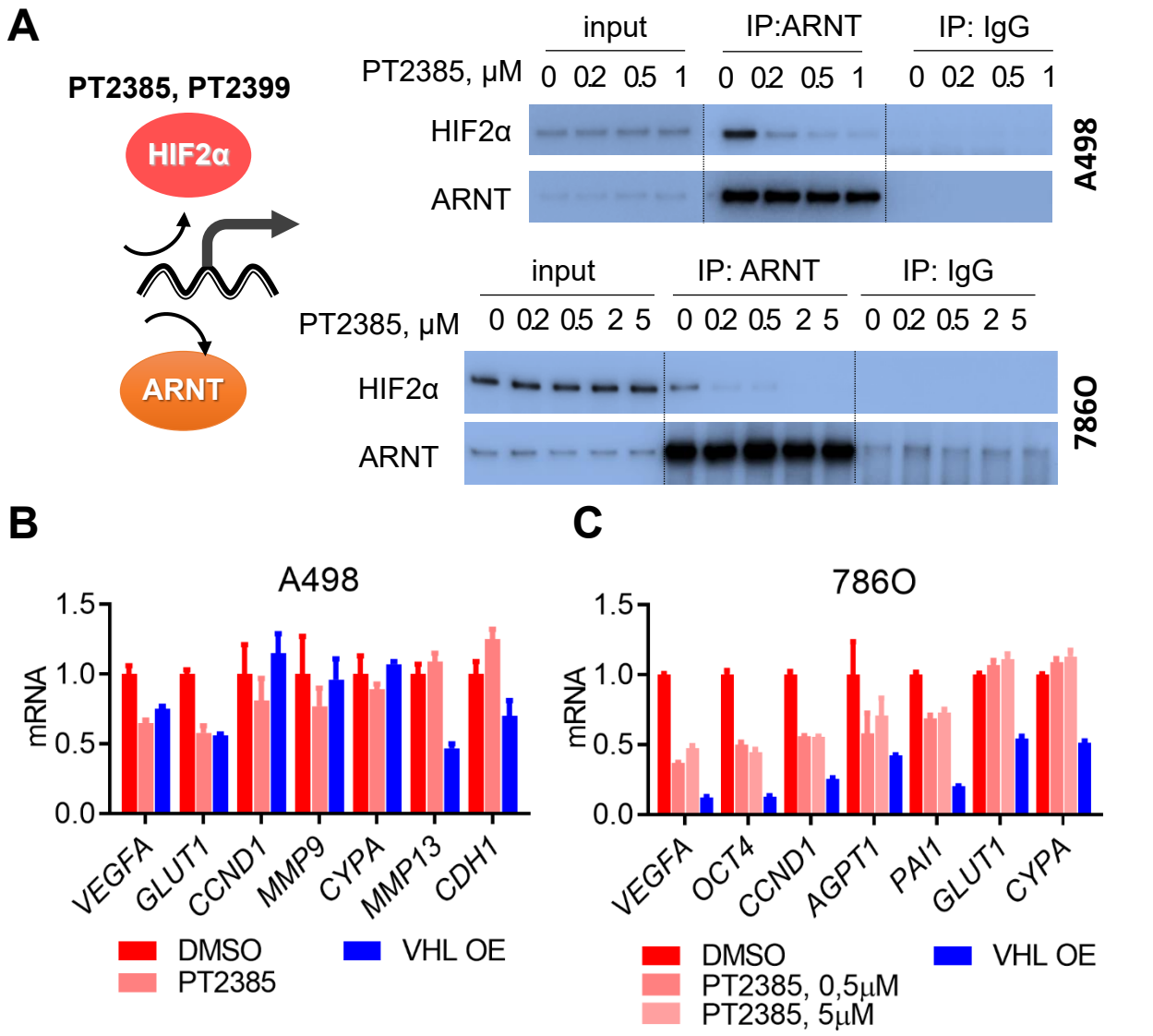

Figure 5. PT2385 inhibitor effectively disrupts the HIF2α/ARNT heterodimer, but only partially represses HIF2 target genes. A. Co-immunoprecipitation of HIF2α and ARNT: wild type A498 and 786O cells were treated with increasing concentrations of PT2385 or DMSO (control). Immunoprecipitation of ARNT revealed concentration-dependent disruption of the heterodimer upon inhibitor treatment. **B.** HIF2α target gene expression after treatment with the PT2385 inhibitor analyzed by qPCR. A498 cells treated for 48 hours with 0.2 μM PT2385 showed only a partial target gene repression**.** Error bars indicate standard error of the mean of technical triplicates. **C.** 786O cells treated for three days with the indicated concentrations of PT2385 or DMSO (control). mRNA expression was analyzed by qPCR. Expression was normalized to hRPS14. Relative mRNA expression was set in reference to the corresponding control, i.e. to DMSO-treated samples. Error bars indicate standard error of the mean of technical triplicates.

2.2.3. Generation and validation of the HIF2α QMY mutant that cannot heterodimerize with ARNT

To further explore the ARNT-independent role of HIF2α in tumor cell invasion and metastasis and exclude the possible off-target effects of the tested inhibitors, we generated a mutant HIF2α which cannot bind ARNT. Based on the published crystal structure of the HIF2α/ARNT heterodimer, three amino acids glutamine 322, methionine 338, and tyrosine 342, which are close to the PASB domain of HIF2α, were identified to be crucial for assembling of the transcriptionally active HIF2α transcription factor and its recruitment to the chromatin (160, 161). Therefore, using mutagenic PCR we generated a triple-mutant of HIF2α in which the abovementioned amino acid residues were replaced by glutamate, glutamate, and threonine, respectively: Q322E, M338E, Y342T (Fig. 6A). This mutant, further referred to as QMY mutant, was used in subsequent *in vitro* and *in vivo* assays.

First, we explored if the introduced mutations indeed abrogate the interaction with ARNT. First, we performed co-immunoprecipitation assays with the generated A498 cells that stably overexpress either the HA-tagged WT or the HA-tagged QMY version of HIF2α (Fig. 6). We observed that WT HIF2α efficiently interacted with ARNT, while the QMY mutant could not bind ARNT after a HIF2α-pull down (Fig. 6B, anti-HA pull down, left). This result was further verified by immunoprecipitation of ARNT and detection of the co-immunoprecipitated HA-tagged HIF2α (Fig. 6B, anti-ARNT pull down, right). These results indicate that mutations of the three key amino residues are sufficient to disrupt the HIF2α/ARNT complex. The verified constructs we further used to generate stable cells by overexpression of HA- or Flag-tagged human WT and QMY HIF2α.

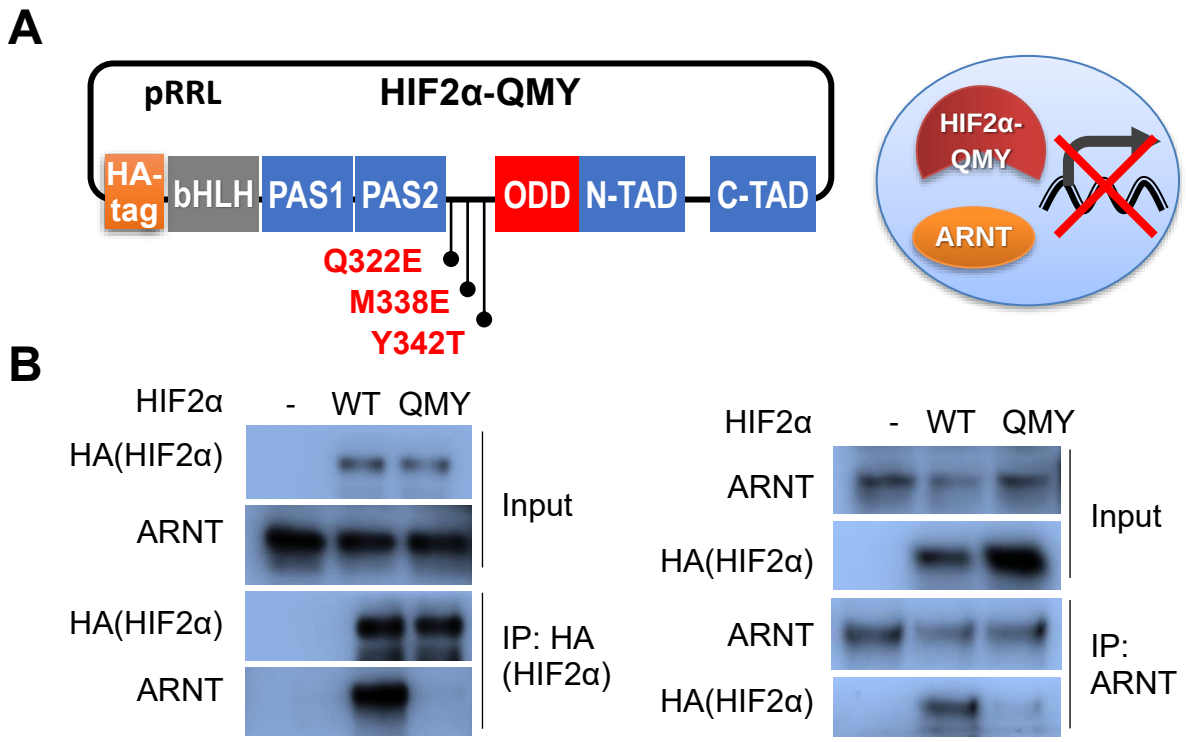

Figure 6. Generation of the QMY mutant of HIF2α that does not bind ARNT. A. Schematic protein structure of the HIF2α QMY mutant. Mutagenic PCR was used to mutate three amino acids found to be critical for HIF2α-ARNT heterodimer formation and transcriptional activity of HIF2 (residues marked in red; HA-tag was added to the N-terminus of the protein). **B.** Co-immunoprecipitation of the HIF2α QMY mutant and ARNT. A498 cells were generated to stably overexpress the empty vector (control), HA-tagged wild type (WT) or mutant (QMY) HIF2α. Cell lysates were prepared and immunoprecipitation in native conditions was performed with anti-ARNT or anti-HA antibodies. Precipitated proteins were detected by immunoblotting with the indicated antibodies.

HIF2α was shown to be expressed at high levels in CRC as the result of the hypoxic microenvironment and thus to contribute to invasion and metastasis in these tumors. Therefore, we generated HIF2α knockout human HCT116 colorectal carcinoma cells using the CRISPR-Cas9 technology and then introduced WT and mutant HIF2α to these cells. To mimic the hypoxic tumor microenvironment of CRC and stimulate the accumulation of the HIF2α protein, we treated the HCT116 control, WT, and QMY cells (all VHL-proficient) with deferoxamine (DFO). DFO

inhibits proline hydroxylases and prevents HIF2α hydroxylation and thus – its recognition by the endogenous pVHL.

First, to exclude any effect of endogenous HIF2α we generated CRISPR-Cas9 HIF2α-knockout HCT116 cells. Then, Flag-tagged WT and QMY versions of HIF2α were introduced with the help of a transposon vector. Similar to A498 cells, co-immunoprecipitation of HIF2α with anti-Flag antibodies in HCT116 cell lysates revealed that WT could efficient co-precipitate ARNT, while the QMY mutant could not (Fig. 7).

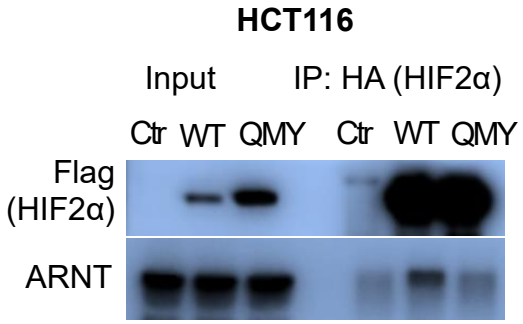

Figure 7. HIF2α QMY mutant does not interact with ARNT in HCT116 human colorectal carcinoma cells. Co-immunoprecipitation of the WT and QMY HIF2α with endogenous ARNT in HCT116 cells treated with DFO. Cell lysates prepared and immunoprecipitation under non-denaturing conditions was performed with anti-HA beads. Precipitated proteins were detected by immunoblotting with the indicated antibodies.

2.2.4. QMY mutant stimulates invasion to the same extent as WT HIF2α in ccRCC and CRC cells

Next, we proceeded to assess invasion of the generated cells in the modified Boyden chamber matrigel assay. QMY HIF2α promoted invasion to the same extent as the WT HIF2α in both A498 and 786O cells (Fig. 8). Moreover, we found similar effect of the QMY HIF2α mutant on invasion in HCT116 cells (Fig. 9). Hence, we conclude that the invasive phenotype is HIF2α-dependent, but independent of the heterodimerization with ARNT. The impact of HIF1α can be excluded, since neither of the tested RCC lines expresses the protein; although

HIF1α is present in the HCT116 line, invasion was relatively weak in the control cells and was significantly enhanced by the overexpression of HIF2α.

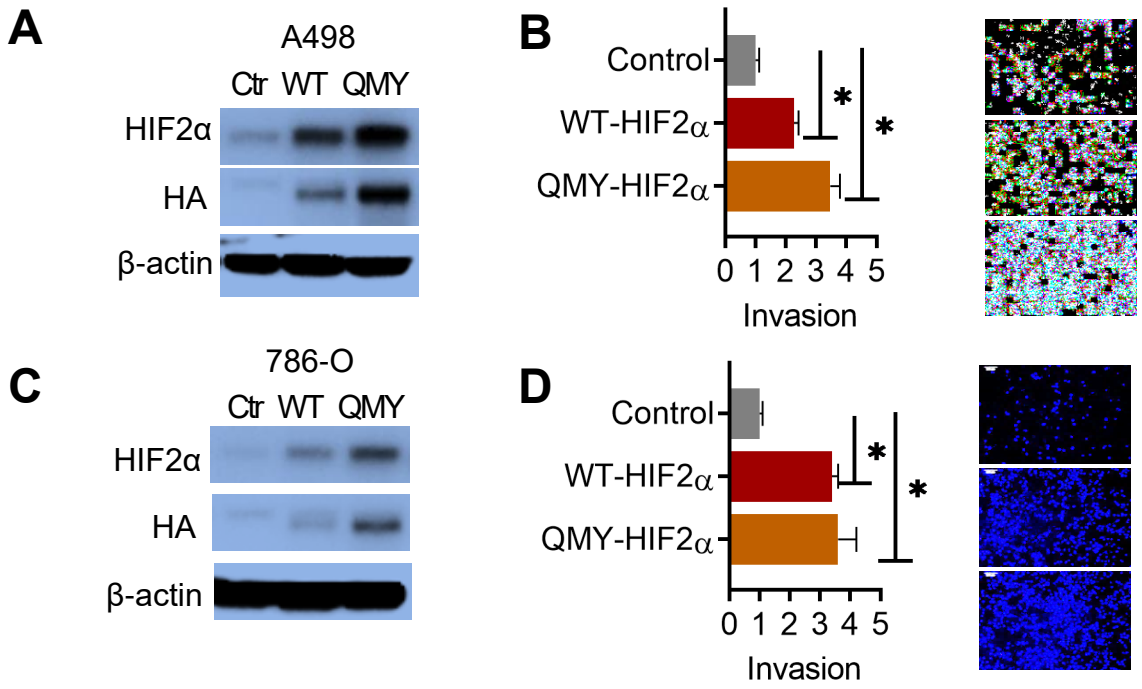

Figure 8. Overexpression of the QMY mutant of HIF2α promotes invasion similar to the wildtype protein in ccRCC cells. A. Immunoblots of total cell lysates from A498 stably expressing mCherry-control, HA-tagged WT or QMY HIF2α. Total cell lysates subjected to immunoblotting with indicated antibodies against endogenous and HA-tagged HIF2α. **B**. WT and QMY HIF2α mutant are equally potent in stimulating invasion *in vitro*. A498 cells overexpressing the respective versions of HIF2α were tested for invasion in the modified Boyden chamber assay. Scale bars 500 µm. Error bars represent standard error of the mean. Representative results of several independent experiments. **C**. Immunoblots of total cell lysates from 786O stably expressing the mCherry-control, HA-tagged WT or QMY HIF2α. Total cell lysates subjected to immunoblotting with indicated antibodies against endogenous and HA-tagged HIF2α. **D**. Overexpression of WT or QMY HIF2α stimulates invasion of 786O cells to the same extent. 786O were tested for invasion in the modified Boyden chamber assay. Scale bars 500 µm. Error bars represent standard error of the mean. Representative results of several independent experiments.

In these experiments we also used the bHLH truncation-mutant (Fig. 10, scheme) of HIF2α that lacks the DNA binding domain and compared the three versions of HIF2α to the empty-vector control cells for their ability to invade in matrigel.

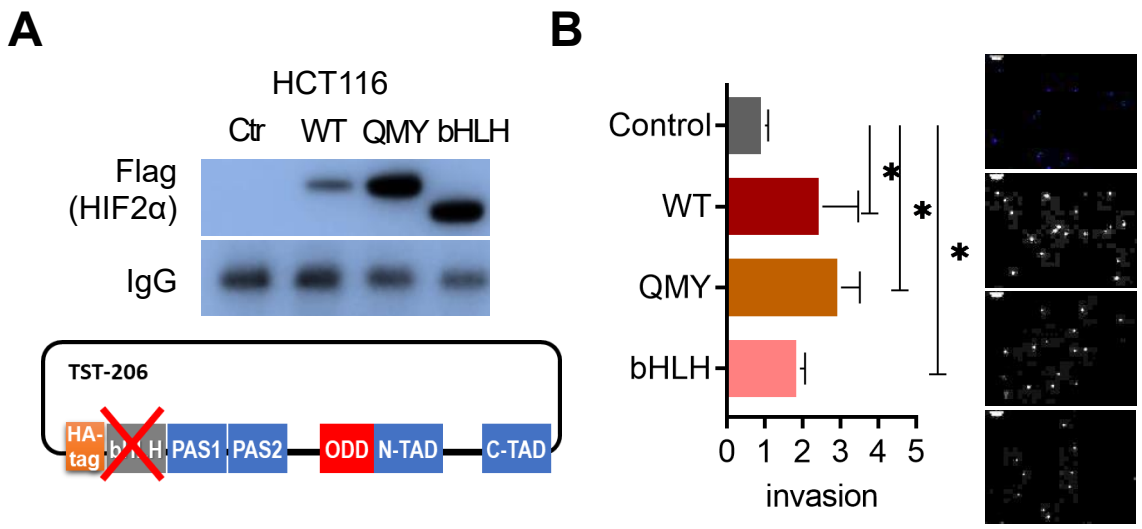

Figure 9. Overexpression of the QMY and bHLH HIF2α mutants promotes invasion equally to the wildtype HIF2α in CRC cells. A. HCT116 HIF2α knockout cells reconstituted with the WT, QMY, or bHLH HIF2α were pretreated overnight with 100 μM DFO to ensure HIF2α stabilization and subjected to immunoprecipitation with mouse anti-Flag antibodies. IgG served as a loading control. Scheme represents the structure of the bHLH mutant of HIF2α. Representative immunoblot of at least three independent experiments. **B.** Boyden chamber invasion assay comparing HCT116 cells overexpressing WT, QMY or bHLH HIF2α. Cells were treated with 10 μM DFO for 72 hours prior to invasion to allow for HIF2α accumulation. Error bars represent standard error of the mean of biological triplicates. Scale bars 500 μm.

Due to the lack of the DNA binding domain which is required for binding to the hypoxic response elements and heterodimerization with ARNT, the bHLH mutant is expected to be transcriptionally inactive. However, overexpression of the bHLH-deficient HIF2α mutant could still promote invasion in comparison to the control line (Fig. 9C), although it was somewhat weaker compared to the WT or QMY HIF2α. Taken together, these results show that neither disruption of the HIF2α/ARNT heterodimer, nor deletion of the DNA binding domain of HIF2α reduces invasion of RCC and CRC cells, suggesting that HIF2α might utilize alternative ways to control this phenotype of tumor cells.

2.2.5. Targeting ARNT with a shRNA does not suppress invasion in renal carcinoma cells

In the following experiments we aimed to assess the contribution of ARNT to the invasion phenotype of tumor cells. For this, we targeted ARNT with a shRNA in the established set of 786O cells (control, and those overexpressing WT and QMY HIF2α), and compared their invasion in the modified Boyden chamber assay (cells transduced with a non-targeting shRNA were used as relevant controls). Firstly, we verified the knockdown efficiency by immunoblotting. We observed an efficient knockdown of the ARNT protein to barely detectable levels in all lines (Fig. 10A). Importantly, targeting ARNT did not affect the levels of HIF2α as verified by the immunoblot (Fig. 10A).

Interestingly, Boyden chamber invasion assay results showed that targeting ARNT does not lead to reduction of cell invasion neither in the control, nor in the WT- or QMY-overexpressing cells (Fig. 10B). In fact, we found that invasion was even slightly increased upon ARNT knockdown in all cell lines. These results further support our hypothesis that HIF2α controls invasion in an ARNT-independent way.

2.3. QMY mutant promotes metastasis equally to WT HIF2α

2.3.1. *In vivo* QMY mutant induces metastasis in an orthotopic transplantation of RCC cells, but not in a passive metastasis model

In the previous sections we showed that HIF2α-ARNT binding is not required for tumor cell invasion *in vitro.* Next, we set out to investigate if HIF2α-ARNT interaction is playing a role in metastasis. For this, 786O cells were used which were shown to be suitable for studying ccRCC metastasis *in vivo* (98, 162-164).

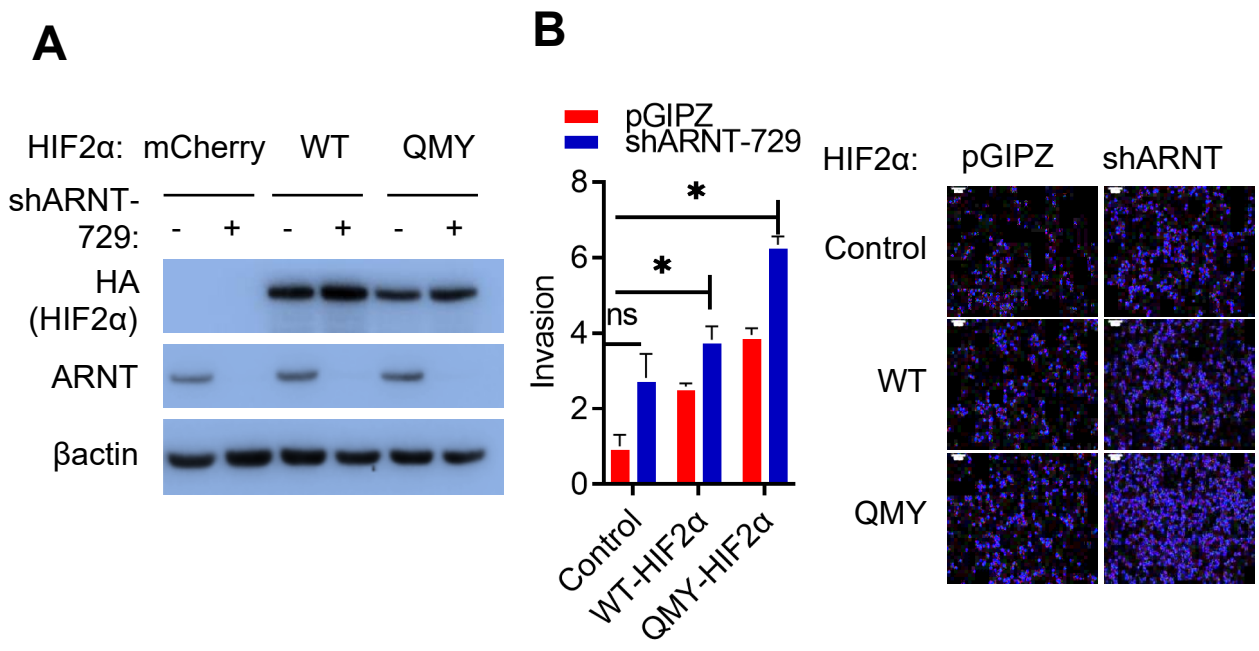

Figure 10. Targeting ARNT with a shRNA does not suppress invasion of WT or QMY HIF2α-overexpressing RCC cells. A. Immunoblots of total cell lysates from 786O cells showing a significant reduction in ARNT protein levels. Cells were generated to stably express pGIPZ empty vector or a shRNA against ARNT in mCherry control, WT, or QMY HIF2α-overexpressing cells. Total cell lysates subjected to immunoblotting with indicated antibodies. **B.** Modified Boyden chamber invasion assay results with shRNA against ARNT in 786O cells overexpressing mCherry control, WT or QMY HIF2α. Error bars represent standard error of the mean of technical replicates. Representative results of two independent experiments. *p<0.05

786O cells overexpressing mCherry control, WT and QMY HIF2α were used in two different models of *in vivo* metastasis (Fig. 11A):

1) passive metastasis model where 786O cells colonized the organs after being injected into the tail vein of immunodeficient NOD scid gamma NMRI-Foxn1nu/nu (NSG) mice. In this model the primary organ of metastatic colonization are the lungs. Superficial metastatic nodules in the lungs were quantified as a final readout in the experiment;
2) spontaneous metastasis model in which cells were transplanted orthotopically into the kidney of NSG mice and after approximately 35 days (sufficient for

primary tumor growth and invasion) superficial metastases in the lungs and the liver were assessed.

With the passive metastasis model we could observe only very few distinct superficial metastatic nodules (0 to 6 metastases) in the lungs of all three groups, indicating that the allocated time for assessing metastases needs to be optimized since many nodules did not reach sufficient size to be easily detectable (Fig. 11B). More detailed histological investigation is, however, required to estimate micrometastases in the whole organ. Nonetheless, in this experiment we could see a significant increase in lung colonization by the WT HIF2α-overexpressing 786O cells compared to the control, while QMY HIF2α-overexpressing cells failed to form sufficient numbers of macrometastases.

In the spontaneous metastasis model after an orthotopic transplantation we could detect clear metastatic nodules in the lungs of all the experimental groups. However, we encountered a high variability in the numbers of lung metastases between the groups: from 3 to 6 in the control, 4 to 9 in the WT, and 4 to 116 in the QMY group (Fig. 11C). Surprisingly, in this experiment overexpression of the QMY mutant dramatically enhanced metastatic colonization of the lungs by 786O cells, which was not the case with WT HIF2α-overexpressing cells. Interestingly, in case of both models some animals transplanted with WT and QMY HIF2α-overexpressing 786O cells also developed liver metastases, with the highest numbers observed in the spontaneous metastasis model after injection of QMY HIF2α cells. Nevertheless, it is difficult to draw any final conclusions from these preliminary experiments since both models require further optimization, Based on the fact that we observed a significant increase in lung metastasis with the QMY mutant after an orthotopic (and hence –a more physiological) model of metastasis, we speculate that the mutant HIF2α can be even more potent in stimulating metastases than the WT version of the protein.

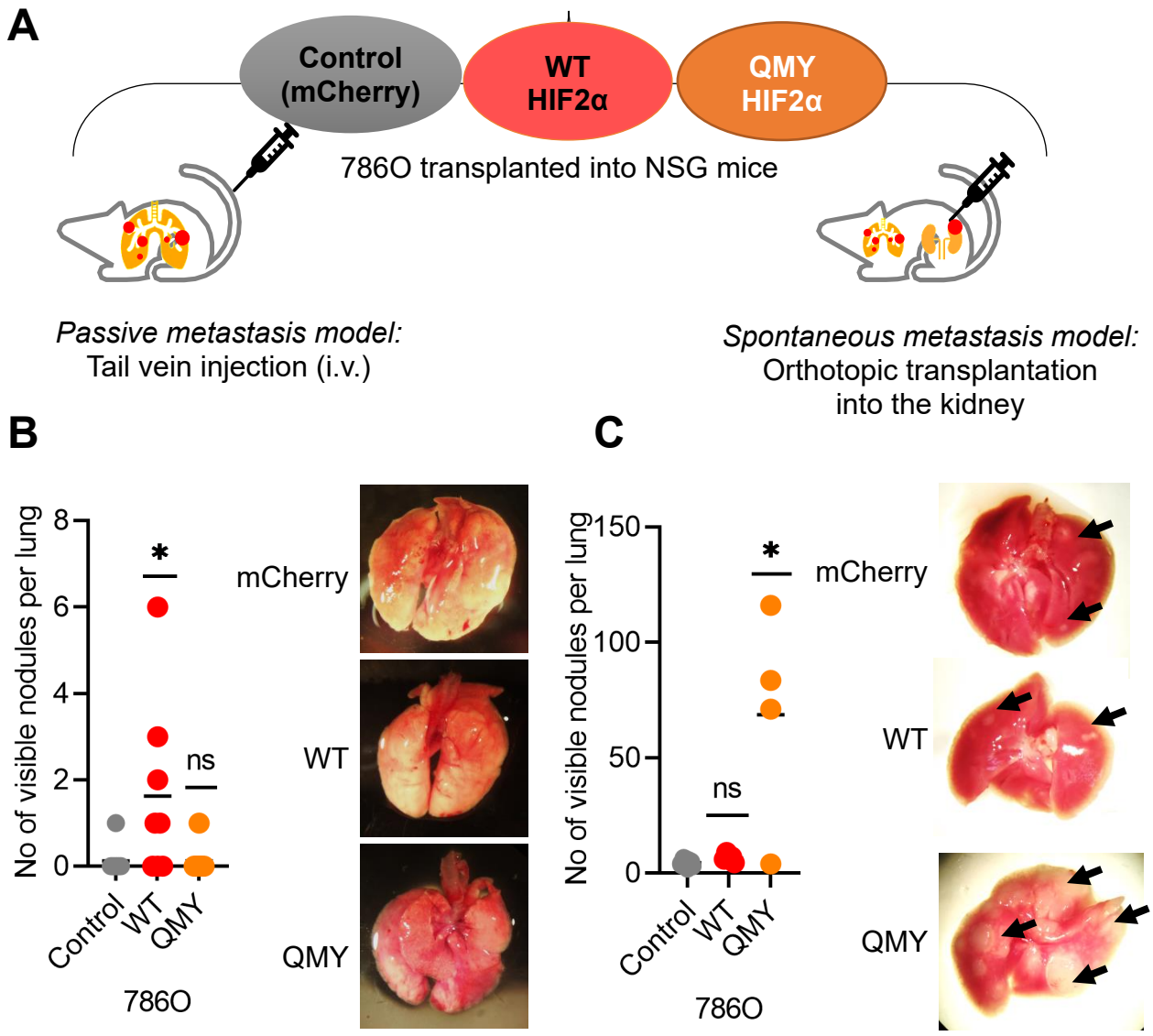

Figure 11. QMY mutant induces metastasis after an orthotopic transplantation of RCC cells, but not in a passive metastasis model. A. Schematic representation of *in vivo* passive and spontaneous metastasis models used in the study. 786O cells were delivered i.v. or by orthotopic transplantation into the kidney. **B.** Quantification of superficial lung metastases showed that WT HIF2α, but not the QMY mutant, significantly increases metastatic colonization in the lungs. Quantification represents the average number of metastases in each group. Representative pictures of lungs from control, WT and QMY HIF2α injected mice. *p<0.05. **C.** Quantification of spontaneous lung metastases showed that QMY HIF2α, but not WT HIF2α, significantly promotes metastasis after an orthotopic transplantation of 786O cells. Quantification represents the average number of metastases in each group. Representative pictures of lungs from control, WT and QMY HIF2α 786O-injected mice. *p<0.05. All animal experiments performed in collaboration with Dr. Angel Cuesta, CIB M.

2.3.2. QMY HIF2α mutant promotes colonization equally to the WT HIF2α in a passive colorectal cancer metastasis model

High expression of HIF2α rather than HIF1α is attributed to progression of colon tumors, thus we also analyzed the role of HIF2α-ARNT interaction in metastasis of colorectal cancer. For this experiment we employed the MCO2 mouse colorectal carcinoma line (kindly provided by Dr. Daniel Dauch) and took advantage of the established splenic seeding passive metastasis model.

First, to test whether human WT HIF2α is able to interact with mouse ARNT, a co-immunoprecipitation assay was performed in MCO2 mouse colorectal carcinoma cells that overexpressed the protein (Fig. 12A). In this assay cells were pretreated with the hypoxia mimetic DFO to allow for HIF accumulation. HIF2α was then precipitated with anti-HA antibodies and the co-precipitated endogenous mouse Arnt was detected by immunoblotting with an appropriate rabbit ani-Arnt antibody. As a result, we could see an efficient interaction between human WT HIF2α and mouse ARNT, which was not the case for the overexpressed QMY mutant of human HIF2α (Fig. 12A). This result justified the employment of MCO2 cells in the planned *in vivo* experiments.

As the previous *in vivo* studies, these experiments were performed in collaboration with Dr. Angel Cuesta at the Margarita Salas Center for Biological Research (CIB M), Spanish National Research Council (CSIC), Madrid, Spain, according to all local and international (FELASA) animal welfare and experimentation regulations.

To study the impact of WT and mutant HIF2α on CRC metastasis, we used the standard model of passive metastasis via the splenic seeding in which tumor cells colonize the liver (Fig. 12A, right). Since this is a well-established model, we observed successful formation of multiple liver metastases in every group (Fig. 12B). Despite the fact, that the exact numbers of superficial liver metastases could

not be accurately estimated due to their abundance, a very pronounced pro-metastatic activity was apparent in both the WT and QMY HIF2α groups compared to the control. We could confirm equal colonization of the livers by the QMY mutant and WT HIF2α-overexpressing MCO2 cells by quantifying the tumor area in hematoxylin-eosin stained slices of the respective livers (Fig. 12C). Overall, these data confirm our hypothesis that HIF2α does not require ARNT binding, but rather utilize other ways to induce metastasis.

2.4. Identification of the PT2385-independent transcriptome by RNA sequencing

2.4.1. RNA sequencing identifies the HIF2α-dependent, but PT2385-independent gene expression profile in RCC cells

Based on the previously described *in vitro* data, disruption of the HIF2α/ARNT heterodimer with the PT2385 inhibitor can only partially influence downstream target gene expression leaving many HIF2α-dependent genes unaltered. Therefore, we applied RNA sequencing to identify the PT2385-independent genes which are supposed to control invasion and metastasis. For that, we performed RNA sequencing of the following samples: 1) A498 cells treated with the PT2385 inhibitor; 2) A498 cells where HIF2α was successfully knocked down with a shRNA; 3) pVHL-reconstituted cells where HIF2α is degraded by the ligase; and 4) control cells turreted with DMSO or expressing a non-targeting control shRNA. First, we identified the HIF2α-dependent genes in the HIF2α knockdown cells and analyzed the intersection with the set of genes which were deregulated after PT2385 inhibitor treatment.

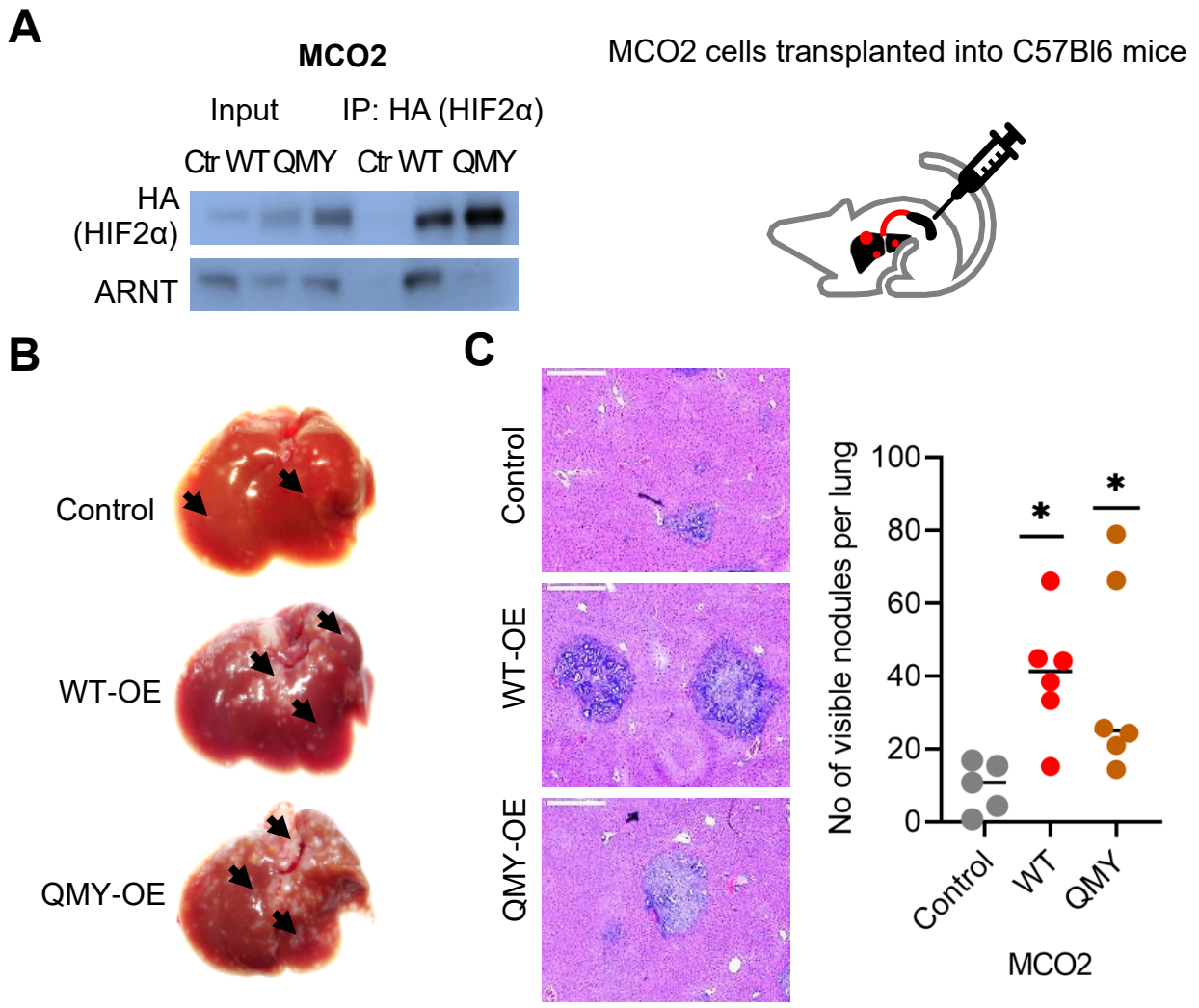

Figure 12. QMY HIF2α mutant promotes metastasis equally to the WT HIF2α in a splenic seeding CRC passive metastasis model. A. Mouse ARNT interacts with human HIF2α. Co-immunoprecipitation of human HIF2α-WT, and -QMY mutant with mouse Arnt in MCO2 cells transduced with an empty vector (control), HA-tagged wild type (WT) or mutant (QMY) HIF2α. Immunoprecipitation in native conditions was done with anti-HA antibodies and detected by immunoblotting. Scheme of the *in vivo* splenic seeding passive metastasis model. MCO2 mouse colorectal carcinoma cells were generated to stably overexpress WT or QMY-HIF2α (empty vector used as a control). Cells were seeded into the livers via an intrasplenic injection. **B**. Representative pictures of livers colonized with MCO2 cells showing that QMY-HIF2α overexpressing cells have the same capacity to form liver metastasis as cells overexpressing the WT-HIF2α (arrows indicate lung metastases). **C**. Representative pictures of hematoxylin-eosin stained MCO2 control, WT or QMY-HIF2α tumor nodules in the liver of C57Bl6 mice. Scale 500 µm. Quantification of the average tumor area per slice per liver. *p<0.05. Experiments performed in collaboration with Angel Cuesta.

As a result, we could identify 321 genes found in both conditions (Fig. 13A) which were further clustered into commonly or differentially regulated genes as shown in the depicted heat map (Fig, 13B). Then, similarly deregulated genes were compared to the published datasets based on gene set enrichment analysis (GSEA) to identify the most significantly enriched gene signature pathways (Fig. 13B, right).

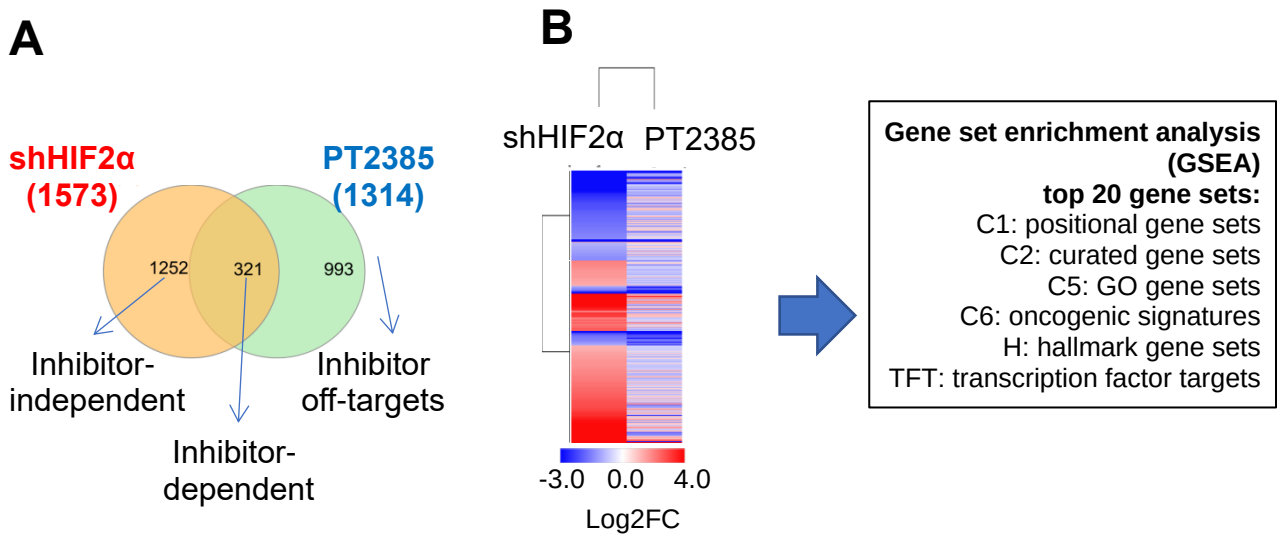

Figure 13. RNA sequencing identifies HIF2α- and PT2385-dependent transcriptomes. A. Venn diagram showing an overlap between HIF2α- and PT2385-dependent transcriptomes. Comparison of genes that were significantly altered after targeting HIF2α with a shRNA to the set of genes deregulated after PT2385 treatment in A498 cells. FDR<0.05. **B.** Heatmap of differentially expressed genes that were commonly regulated by PT2385 and HIF2α (321 genes). Log_2FC with the cut-offs ±1.

At first, we identified genes expression of which was significantly altered by PT2385 inhibitor treatment, and which should represent the HIF2α/ARNT targets. These are genes which were similarly up- or downregulated by the HIF2α knockdown and PT2385 treatment (with the cut-off value of two-fold change; Fig. 14A). Gene set enrichment analysis of the top five significantly enriched

pathways revealed classical HIF2α targets regulating the general hypoxic response and glycolysis (Fig. 14A, right plot).

Interestingly, *CXCR4*, *IGFBP3*, *EGLN3*, which were earlier shown to play a role in metastasis of 786O cells *in vivo* (98, 115, 117), were repressed to the same level in both HIF2α knockdown cells and after PT2385 treatment (data not shown).

2.4.2. RNA sequencing identifies the PT2385-independent transcriptome

Next, a group of genes from the HIF2α/PT2385 commonly deregulated cohort was isolated mRNA levels of which were marginally affected by PT2385, i.e. change in their expression was below a two-fold threshold (Fig. 14B). Interestingly, GSE analysis showed enrichment for pathways involved in cadherin signaling, stem cell genes, and epigenetic regulation by the polycomb repressor complex 2 component EZH2 (Fig. 14B, right).

Yet, for us the most interesting was the group comprising 1252 significantly deregulated genes which were absent from the transcriptome profile of PT2385 treated cells, but dependent on HIF2α. We designated this group of genes as "PT2385-independent" (Fig. 14C). GSE in this cohort showed enrichment for pathways regulating cell adhesion, anchoring to extracellular matrix, intracellular signaling, and most significantly – EZH2 targets (Fig. 14C, right).

Taken together, based on the obtained sequence analysis we may speculate that tumor invasion and metastasis are processes which HIF2α controls independently of ARNT by collaborating with other interacting partners as the epigenetic regulator EZH2, or other transcription factors like catenin, HNF1A, or HNF4A.

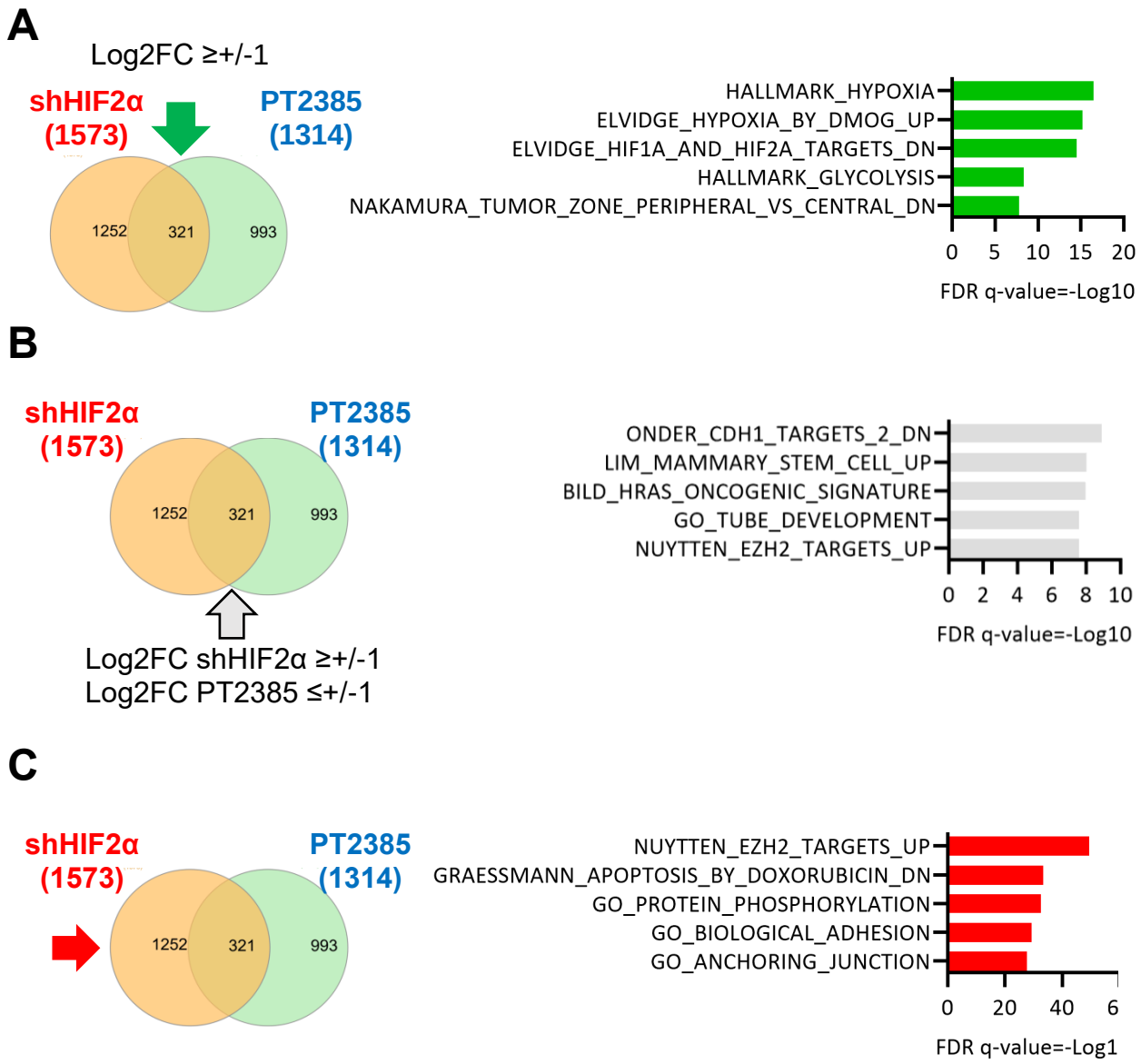

Figure 14. RNA sequencing identifies a PT2385-independent transcriptome in renal carcinoma cells. A. Venn diagram depicting commonly regulated genes between PT2385-treated cells and cells with a shRNA against HIF2α. GSEA plot represents top five enriched pathways. **B.** Highlighted is a subset of genes that are marginally affected by the PT2385 inhibitor (below the threshold), but significantly deregulated by the shRNA against HIF2α. GSEA plot represents top five pathways enriched for these genes. **C.** Venn diagram and GSEA plot of the top five enriched pathways showing genes which are dependent on HIF2α, but are not affected by the PT2385 inhibitor.

2.4.3. RNA sequencing identifies common HIF2α-EZH2 downstream targets

Based on the RNA sequencing data described above, we decided to focus on the most significantly enriched gene set involving the polycomb repressor complex (PRC2) targets. For further analysis we took only HIF2α, but not PT2385 dependent genes. In particular, we looked for the intersection between the found gene list and the published gene set from a study by Nuytten et al (138) who identified EZH2-dependent genes after an EZH2 knockdown by siRNA in PC3 cells (curated gene set C2). Heat map in Fig. 13B shows that in total 104 genes were found in the intersection (Fig. 15), which represents genes expression of which becomes upregulated after targeting EZH2 or HIF2α.

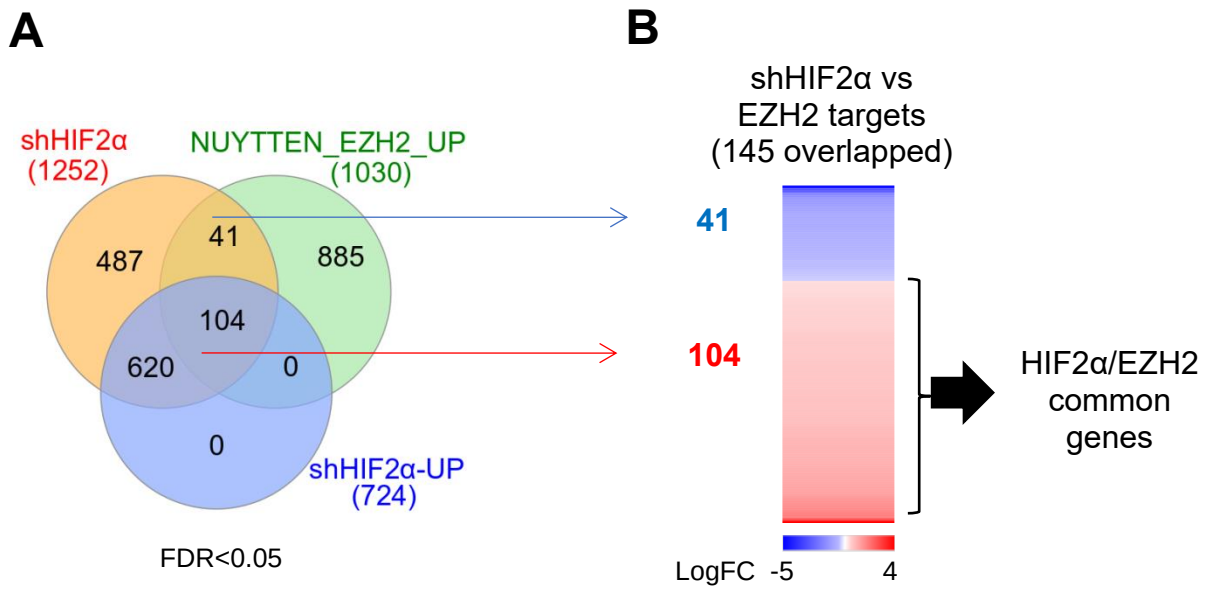

Figure 15. RNA sequencing identifies common HIF2α-EZH2 downstream target genes. A. Venn diagram showing an overlap between HIF2α- and EZH2-dependent, but PT2385-independent target genes. **B.** Heat map with the identified 104 genes that become upregulated after targeting EZH2 and HIF2α with siRNA or shRNA, respectively ("Nuytten EZH2 targets UP", based on the Curated gene set (C2) (138). $Log_2FC \geq 0.4$, FDR<0.05.

These results suggest that HIF2α collaborates with EZH2 to repress a set of genes which might be involved in regulation of invasion and metastasis.

2.4.4. Overexpression of either the QMY mutant or WT HIF2α represses the identified common HIF2α/EZH2 target genes

Based on the results of the previous section, we could see that targeting HIF2α or EZH2 leads to an upregulation of a number of genes. Therefore, in the next experiments we aimed to investigate whether overexpression of HIF2α could suppress the identified HIF2α/EZH2 common target genes and to which extent this transcriptome phenotype would be dependent on HIF2α/ARNT binding. For this, we undertook an unbiased approach and looked at RNA sequencing profiles of WT- and QMY-overexpressing A498 cells and compared the list of significantly deregulated genes from those cells with all significantly deregulated genes after shHIF2α that were PT2385-independent. In general, we found fewer significantly deregulated genes in QMY compared to WT HIF2α-overexpressing cells (Fig. 16A). We could identify 105 target genes which overlapped between these three groups (heat map showing these genes depicted in Fig. 16B). Gene set enrichment analysis based on the curated gene set (C2) shows five most significantly deregulated pathways which overlap with up- and downregulated genes in WT and QMY (Fig. 16C). We found that genes repressed by the WT and QMY HIF2α are significantly enriched in the published Nuytten dataset (138) where expression of these genes was shown to increase upon targeting EZH2 with siRNA, or silenced by a H3K27me3 mark. These results are in line with the findings described in the previous section, suggesting that HIF2α collaborates with EZH2 to repress a certain set of genes.

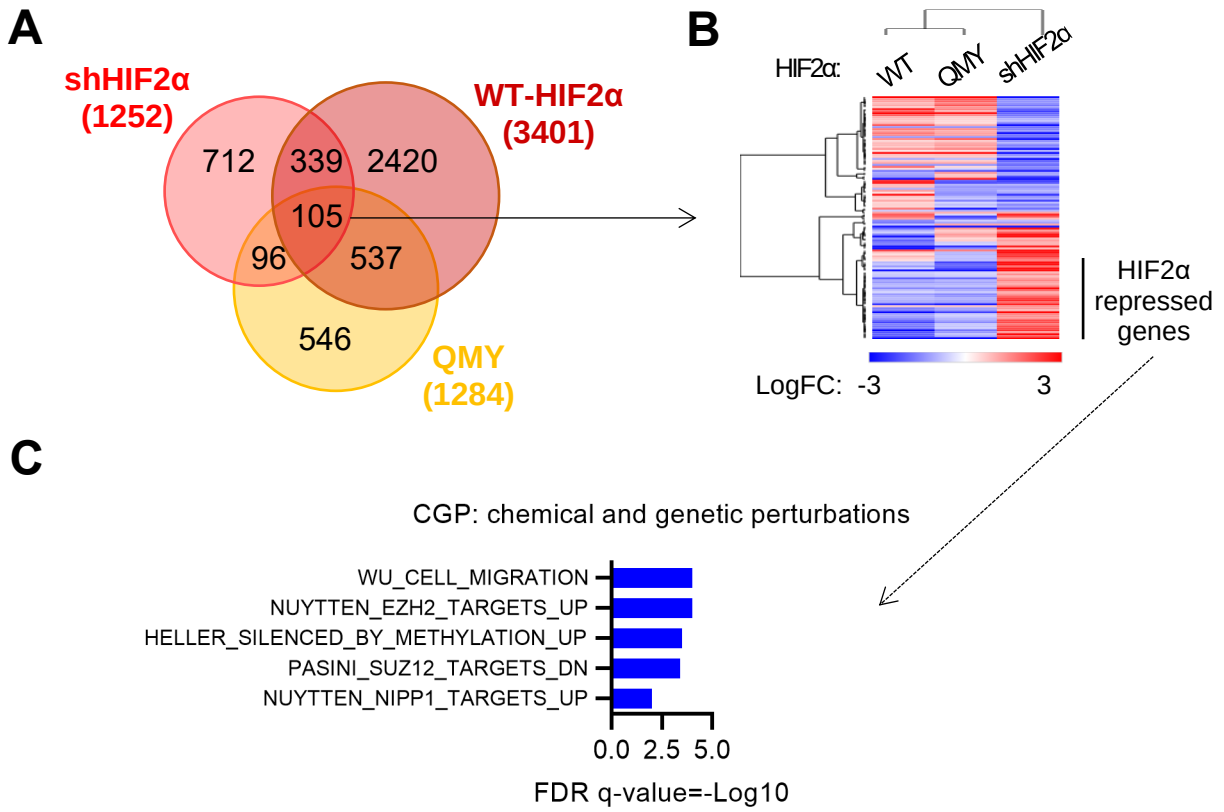

Figure 16. WT and QMY HIF2α repress common HIF2α/EZH2 target genes. A. Venn diagram representing an intersection between significantly deregulated genes in cells overexpressing WT or QMY HIF2α and shHIF2α that are PT2385-independent. FDR≤0.1. **B.** Heat map showing deregulated genes between the shHIF2α, WT and QMY gene sets, that are independent of the PT2385 inhibitor. FDR<0.1. **C.** Depicted are GSEA results for WT and QMY HIF2α target genes that are regulated in accordance with the published Curated gene sets (C2) dataset (138), i.e. genes that are repressed by WT and QMY HIF2α and increased upon targeting EZH2 or by inhibiting histone trimethylation. FDR≤0.1.

2.4.5. Overexpression of the QMY mutant results in a similar profile to WT HIF2α transcriptome in MCO2 tumor cells isolated from liver metastases

Based on the findings describe in the previous sections, next we aimed to investigate which downstream targets of HIF2α and respective pathways are involved in controlling metastasis in an HIF2α/ARNT heterodimer-independent fashion. For that, we employed RNA sequencing and analyzed tumor cells from the metastatic liver nodules of MCO2 cells from the experiment described in section 2.3.2. (Fig. 17).

We resected the metastases liver nodules from four livers of mice in each experimental group, isolated RNA from the samples and used that for RNA-Seq. First, we identified the tumors with most similar transcriptome profiles using principal component analysis since tumors within each group showed quite heterogeneous gene expression patterns (Fig. 17A, upper panel). This might be explained by some technical reasons: to obtain a reasonable amount of RNA several small nodules from a mouse liver had to be taken in case of the control group, while for mice bearing QMY or WT HIF2α-overexpressing MCO2 cells in most of the cases one or very few tumor nodules were sufficient.

Next, for RNA sequencing analysis we focused on the closest clusters and took two samples from each group to calculate the statistically significant changes in gene expression (Fig. 17A, lower panel). Expression levels of top 100 significantly deregulated genes from each sample are represented in the heat map in Fig. 15B. From this set of genes we then identified those which are similarly repressed or upregulated by WT and QMY HIF2α in MCO2 tumors, and compared the final gene set with the published datasets. Several gene set enrichment analysis databases were used in the analysis: positional gene sets (C1), curated gene sets (C2), GO gene sets (C5), oncogenic signatures (C6), hallmark gene sets (H), and transcription factor targets (TFT), based on which we identified the top significantly enriched gene sets. The final result of this complex analysis is depicted in Fig. 17C, where twelve top significantly enriched sets of commonly deregulated target genes (six up- and six downregulated) between WT and QMY HIF2α are presented.

In all, we could identify the pathways that are most likely driving the metastatic phenotype in MCO2 CRC cells, among which particularly interesting for us were the components of the epigenetic machinery that conveys the histone H3K27me3 repressive mark (catalyzed by PRC2), genes regulating locomotion and anchoring

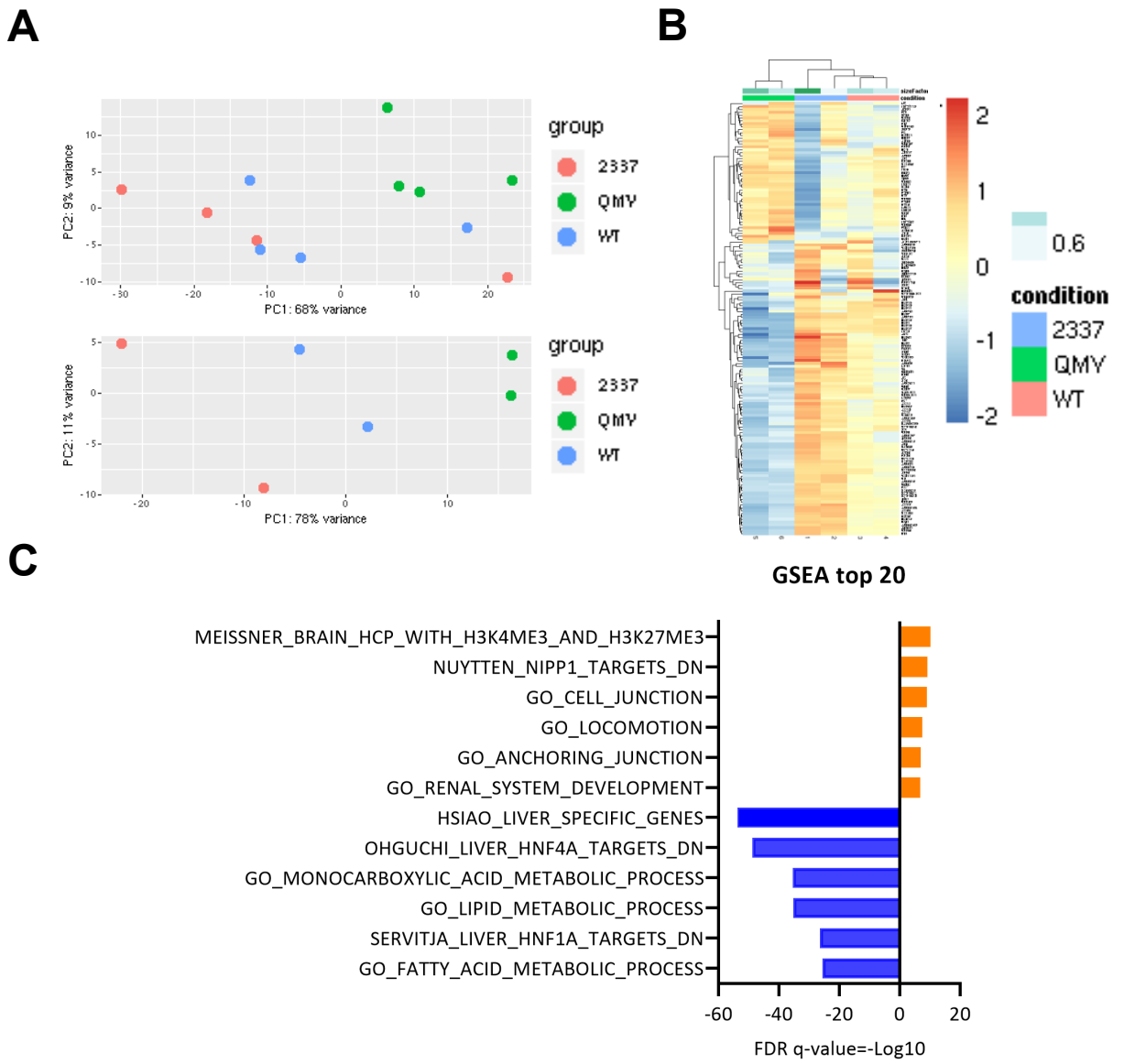

Figure 17. Transcriptome profile of QMY-overexpressing MCO2 cells from liver metastatic nodules is similar to that of the WT HIF2α-overexpressing MCO2 nodules. A. Principal component analysis of RNA-Seq metadata from control, WT and QMY-overexpressing HIF2α tumor nodules. Two samples with high sequencing quality were taken from each group for further analysis. **B.** Heat map of Log_2FC of the top 100 significantly deregulated genes from MCO2 liver tumor nodules of two samples from each group. Adjusted p value <0.1. **C.** Gene expression profiles of MCO2 WT and QMY HIF2α-overexpressing tumors were compared to published gene sets from the GSEA database. Plot representing the top significantly enriched pathways is depicted. Genes which are associated with the EZH2 enzymatic product – H3K27me3, and NIPP1(inhibitor of PP1 phosphatase) are highly enriched. FDR<0.1; Log_2FC cut-off ±1.

junctions, and genes controlled by HNF1A and HNF4A that were commonly regulated by WT and QMY HIF2α (Fig. 17C). Overall, these results were instrumental in the identification of HIF2α dependent, but ARNT-independent regulators of metastasis that are controlled by HIF2α on the transcription level

2.5. HIF2α regulates PRC2 activity in ccRCC and CRC cells

2.5.1. HIF2α regulates H3K27me3 levels in ccRCC and CRC cells

To investigate the connection between HIF2α, EZH2 activity, and H3K27me3 levels in ccRCC and CRC cells we employed several lines: HCT116 cells in which we knocked out HIF2α with CRISPR/Cas9, and two RCC lines, A498 and 786O, overexpressing pVHL. Immunoblotting showed significant reduction in H3K27me3 levels in cells where HIF2a was depleted either due to the pVHL reconstitution or upon HIF2α CRISPR knockout (Fig. 18A).

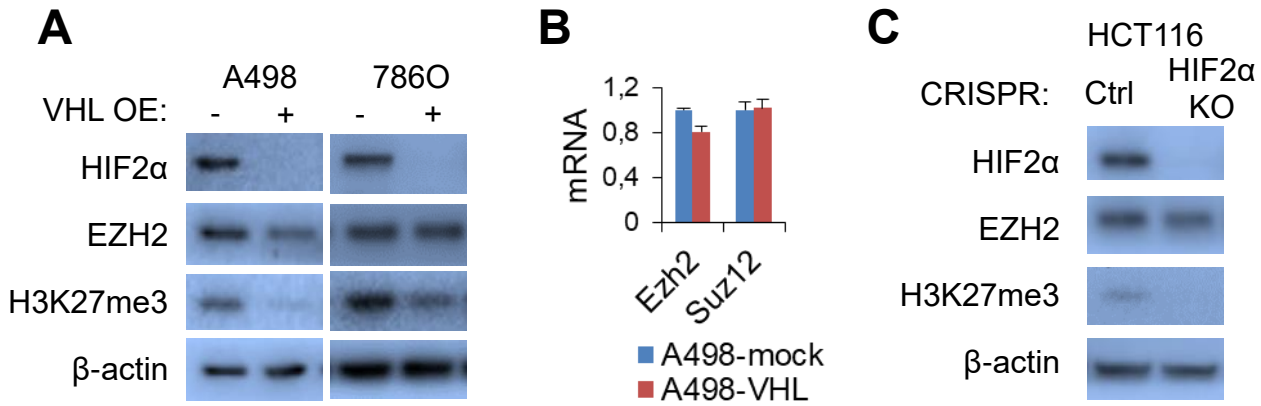

Figure 18. HIF2α regulates H3K27me3 levels in ccRCC and CRC cells. A. HIF2α deficiency correlates with low H3K27me3 levels. Immunoblots of total cell lysates from ccRCC cells with reconstituted pVHL which results in HIF2α degradation. **B.** mRNA analysis showed unaltered levels of EZH2 and Suz12 in A498 cells. pVHL-overexpressing cells served as a HIF2α negative control. **C**. Immunoblots of total cell lysates from HCT116 cells where HIF2α was knocked out using CRISPR/Cas9 genome editing.

Interestingly, we saw no significant changes in EZH2 protein levels in 786O cells, and very mild effects on EZH2 in A498 or HCT116 cells despite the dramatic

downregulation in the H3K27me3 mark in all lines. Importantly, with these experiments we may exclude any possible direct effects of pVHL on H3K27me3 levels, since in pVHL-proficient HCT116 cells H3K27me3 levels decreased upon the HIF2α KO (Fig. 18C). These results suggest that HIF2α might activate EZH2 functions and thus promote the trimethylation of histone H3 (H3K27me3).

2.5.2. HIF2α directly interacts with the PRC2 component EZH2

To address the question if HIF2α can directly bind to EZH2 we performed several interaction studies, including a proximity ligation assay (PLA) and co-immunoprecipitation experiments. PLA allows for *in situ* detection of protein-protein interactions at a single molecule resolution. Protein interactions are scored by a positive PLA signal which is amplified by a polymerase chain reaction after the incubation with specific PLA probes against the proteins of interest. We detected a strong PLA signal after EZH2 and anti-HA immunostaining for the QMY mutant and the WT HIF2α (Fig. 19A).

Interestingly, the PLA signal was also detected in the cytoplasm indicating possible HIF2α/EZH2 interactions outside the cell nuclei which suggests that EZH2/HIF2α complexes might exert some DNA- or transcription-independent functions. Additionally, immunoblot of cell lysates immunoprecipitated with the anti-HA conjugated agarose beads showed efficient co-precipitation of EZH2 in both WT and QMY HIF2α overexpressing cells (Fig. 19B). Together, these results confirm that HIF2α can efficiently bind EZH2 independently of ARNT.

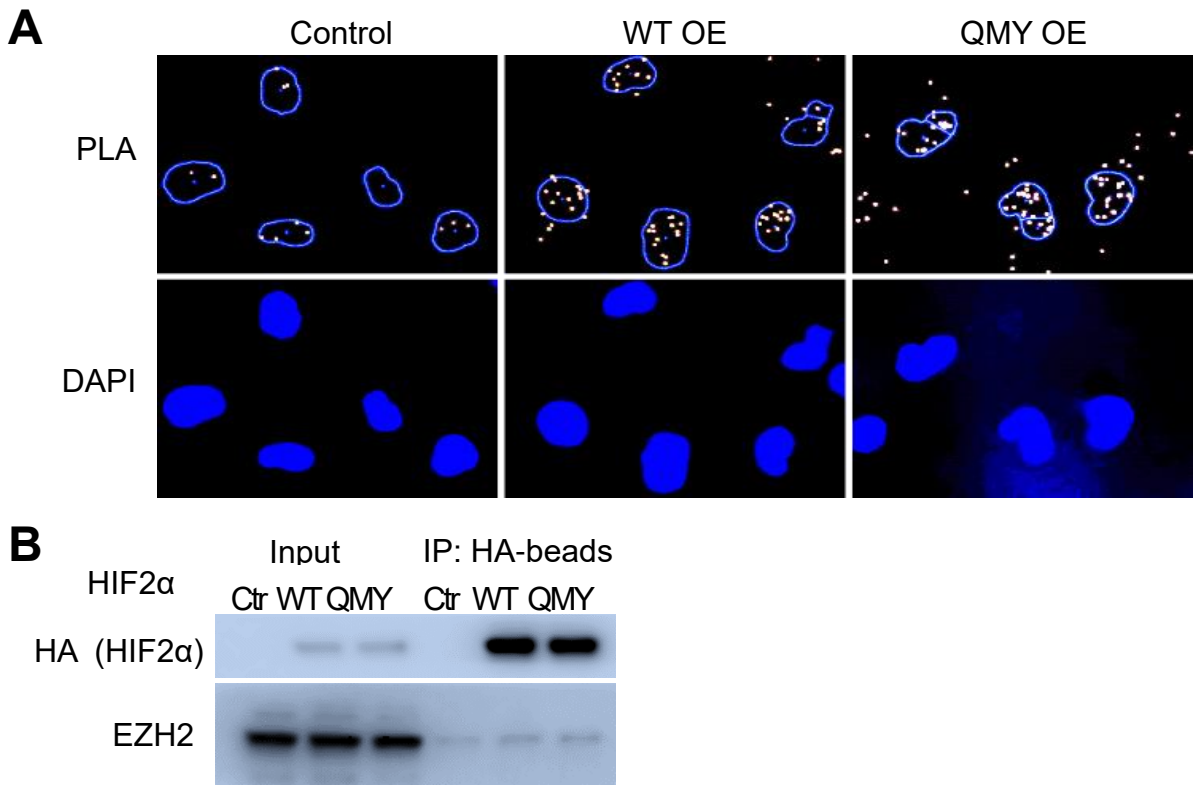

Figure 19. HIF2α directly interacts with EZH2. A. Proximity ligation assay in A498 cells showing that HIF2α QMY mutant interacts with EZH2 to the same extent as WT HIF2α. 60 x. **B.** HIF2α QMY mutant interacts with EZH2 similarly to WT HIF2α. Co-immunoprecipitation of EZH2 with either of the two HIF2α protein versions in 786O cells. Cell lysates in non-denaturing conditions were prepared and incubated with anti-HA conjugated agarose beads. Precipitated proteins were detected by immunoblotting with the indicated antibodies.

2.5.3. Identified HIF2α/EZH2 downstream target genes show increased levels of the H3K27me3 repressive mark

Trimethylation of histone H3 at lysine 27 (H3K27me3) is a known repressive mark which is associated with gene silencing. The methyltransferase EZH2 as a part of the multiprotein polycomb repressor complex 2 (PRC2) is responsible for conveying this mark on the histones. To assess if HIF2α can directly mediate gene repression via enhanced trimethylation of histone H3K27 at target genes, chromatin immunoprecipitation (ChIP) experiments were performed with A498 cells that overexpress the HA-tagged pVHL and the respective control line (transduced with an empty vector). As a result of this ChIP experiment, we could identify many

genes regulatory regions of which were characterized by high peak score values of H3K27me3 in HIF2α-proficient cells (compared to pVHL-overexpressing control cells; Fig. 20).

Gene name	Chromosome	Start	End	Peak score	Annotation
GPRC5B	chr16	19969123	19974429	136.2	Intergenic
MAP1B	chr5	71353424	71355364	43.3	Intergenic
MX2	chr21	42725072	42726376	42845	Intron (NM_058186, intron 7 of 7)
OAS1	chr12	1,13E+08	113309220	62.6	Intron (NR_145127, intron 8 of 22)
PARP12	chr7	1,4E+08	139820409	46.8	Intron (NM_030647, intron 8 of 19)
PI3	chr20	43778636	43779136	26420	Intergenic
RRAS2	chr11	14256313	14258036	42935	Intron (NM_006108, intron 7 of 16)
SAMD9	chr7	92709918	92722928	336.7	Intergenic
SAMD9L	chr7	92761857	92763555	34.7	Exon (NM_152703, exon 5 of 5)
SLC1A3	chr5	36733679	36734179	42953	Intergenic

Figure 20. Identified HIF2α/EZH2 downstream target genes are enriched in H3K27me3 peaks in HIF2α-proficient cells. Summary of H3K27me3 ChIP sequencing (ChIP-Seq) results for some of the identified HIF2α/EZH2 target genes in A498 cells. HIF2α/EZH2 target genes are characterized by increased H3K27me3 in their gene regulatory sites. Formaldehyde-crosslinked chromatin from A498 control and pVHL-reconstituted cells was immunoprecipitated with anti-H3K27me3 antibodies and rabbit IgG as a control. Precipitated DNA and decrosslinked inputs were used to construct the libraries. Peak scores represent ratio of tags compared to the appropriate input.

These results suggest that HIF2α can directly impact the expression of those genes through regulation of EZH2-mediated trimethylation of H3 histones on regulatory regions of these genes. Particularly, we saw that high HIF2α protein levels were associated with silencing of the identified genes as the result of elevated H3K27me3 levels.

As the next step, we aimed to test our hypothesis by employing an EZH2 inhibitor: in case the suggested mechanism is correct, we would expect the expression of HIF2α/EZH2 target genes to increase significantly upon EZH2 inhibitor treatment

in HIF2α-proficient cells. For this, we first measured mRNA levels of the genes upon HIF2α knockdown and pVHL reconstitution in A498 cells to clearly identify HIF2α repressed genes. Thus, we found *MX2*, *OAS1*, *SAMD9*, *SAMD9L*, *PI3*, and *SLC1A3* to be repressed by HIF2α (Fig. 21A).

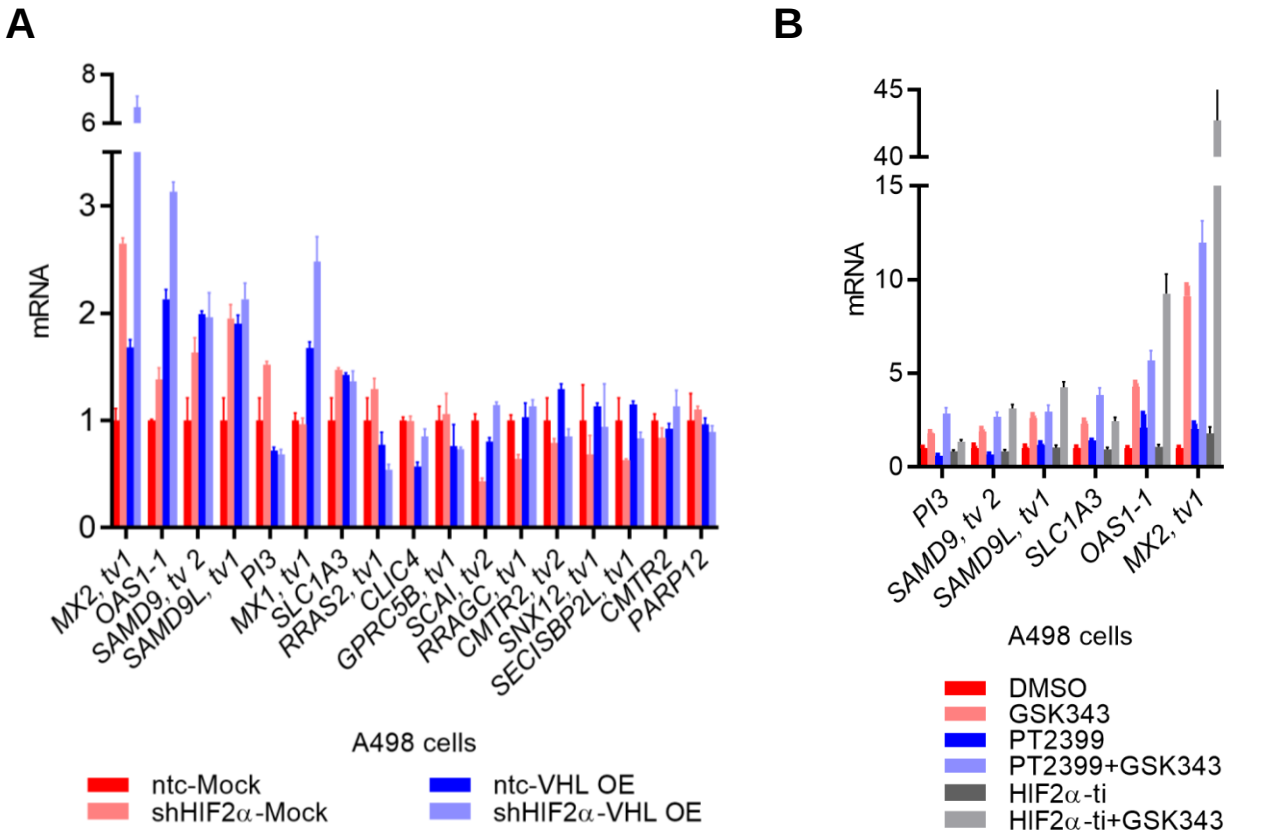

Figure 21. Inhibition of EZH2 activity with GSK343 shows synergism with HIF2α inhibitors for common HIF2α/EZH2 target genes. A. Expression of genes with high H3K27me3 peaks that were found to be commonly repressed by HIF2α and EZH2. mRNA levels analyzed by qPCR in A498 cells after a HIF2α KD and pVHL reconstitution. Expression was normalized to HPRT. **B.** Parental A498 cells were treated for 48 hours with 1 μM PT2399, 5 μM GSK343, 5 μM HIF2α translation inhibitor (ti), or the indicated combination of the drugs (DMSO treated cells served as the control)**.** mRNA expression of the indicated genes was analyzed by qPCR. Expression was normalized to RPS14. Relative mRNA expression was set in reference to the corresponding DMSO-treated control sample. Error bars indicate standard error of the mean of technical duplicates; tv –transcript variant.

Next, A498 cells were treated with the EZH2 inhibitor GSK343, HIF2α/ARNT inhibitor PT2399, and an inhibitor of HIF2α translation (designated HIF2α ti). The

EZH2 inhibitor GSK343 competes with S-adenosine methionine in the reaction of lysine methylation on histone H3 and thus should remove the repressive marks from the target genes, while treatment with the HIF2α translation inhibitor should theoretically affect all processes regulated by HIF2α (independently of the binding with ARNT). Consequently, we found that *MX2, OAS1,* and *SAMD9L* became strongly upregulated upon GSK33 inhibitor treatment (Fig. 21B). Interestingly, combination of GSK33 with the HIF2α translation inhibitor proved to be synergistic in upregulating mRNA levels of those target genes suggesting that EZH2 and HIF2α act in concert. We also found the EZH2 inhibitor to be much more potent compared to PT2399 or HIF2α ti. Nonetheless, either of the combinations (GSK343-PT2399 or GSK343- HIF2α ti) was more potent than GSK343 treatment alone.

Overall, these results show that pharmacological targeting of both EZH2 and HIF2α results in a synergistic effect on the commonly regulated downstream genes. Thus, it is tempting to speculate about the potential of using such a combination as a treatment approach for managing metastatic ccRCC or other HIF2α-dependent tumors.

2.5.4. Analysis of H3K27me3 and EZH2 ChIP sequencing results in combination with transcriptome profiling by RNA sequencing revealed a broader range of HIF2α/EZH2 target genes

We took advantage of the obtained results from high-throughput RNA and ChIP sequencing data and applied another strategy to identify potential HIF2α/EZH2 co-regulated genes apart from GSEA. In addition to the H3K27me3 ChIP, we performed an EZH2 ChIP with subsequent deep sequencing. Both EZH2 and H3K27me3 ChIP sequencing was performed using control and pVHL-reconstituted cells as the relevant HIF2α-proficient and HIF2α-deficient conditions.

First, to identify genes which are specifically HIF2α-dependent, but independent of pVHL, we compared RNA sequencing results from shHIF2α and pVHL-reconstituted A498 cells normalized to appropriate controls. Then, genes expression of which was primarily affected by the HIF2α KD (FDR≤0.1) and not pVHL reconstitution (FDR≥0.1) were taken for further analysis. Next, to further explore the hypothesis that HIF2α mediates the activity of EZH2 and repression of its downstream targets we focused on the group of genes which were upregulated upon HIF2α silencing, but downregulated upon WT and QMY HIF2α overexpression in A498 cells. Then we looked at EZH2 and H3K27me3 ChIP sequencing profiles and identified regions which were enriched in both EZH2 and H3K27me3 peaks in A498 HIF2α-proficient cells. Resultantly, we found 21 regions with EZH2 and 58 regions with H3K27me3 enriched peaks which are summarized in Fig. 22.

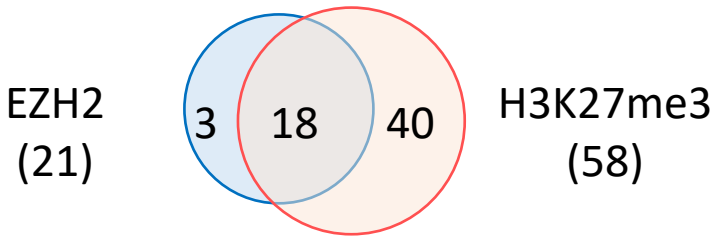

Figure 22. Identification of EZH2/HIF2α target genes upregulated in HIF2α KD A498 cells that show EZH2 and H3K27me3 enrichment in ChIP. Diagram representing HIF2α-dependent, but pVHL-independent genes proximal regions or gene bodies of which show peaks of EZH2 and H3K27me3 identified by ChIP-Seq.

Among these genes, 18 showed an overlap between EZH2 and H3K27me3 ChIP sequencing datasets indicating that HIF2α controls silencing of those genes by recruiting EZH2 and promoting trimethylation of the associated H3 histones.

2.6. High EZH2 expression and low expression of the identified HIF2α/EZH2 target genes correlates with poor prognosis in RCC patients

As the next step in our study, we wanted to identify genes suppressed by the HIF2α/EZH2 axis expression of which correlates with ccRCC patient survival and metastasis. For that, we employed the publicly available KM-plotter tool and the cBio portal to assess TCGA data on RCC patient survival and metastasis.

First, we analyzed the overall survival of ccRCC patients with high or low expression of the identified commonly repressed HIF2α/EZH2 genes. As a result of this analysis, we could narrow down the list of the potential 105 HIF2α/EZH2 repressed targets to 18 genes downregulation of which correlated with a bad prognosis in patients with ccRCC tumors (Fig. 23A).

Importantly, we could see a clear correlation between EZH2 mRNA levels and tumor stage in ccRCC patients (Fig. 23B, left), as well as with the metastasis status of these patients (Fig. 23B, right). Taken together, we propose a model in which HIF2α interacts with EZH2 to represses a set of genes that results in ccRCC tumor progression, metastasis, and significantly decreased survival of patients.

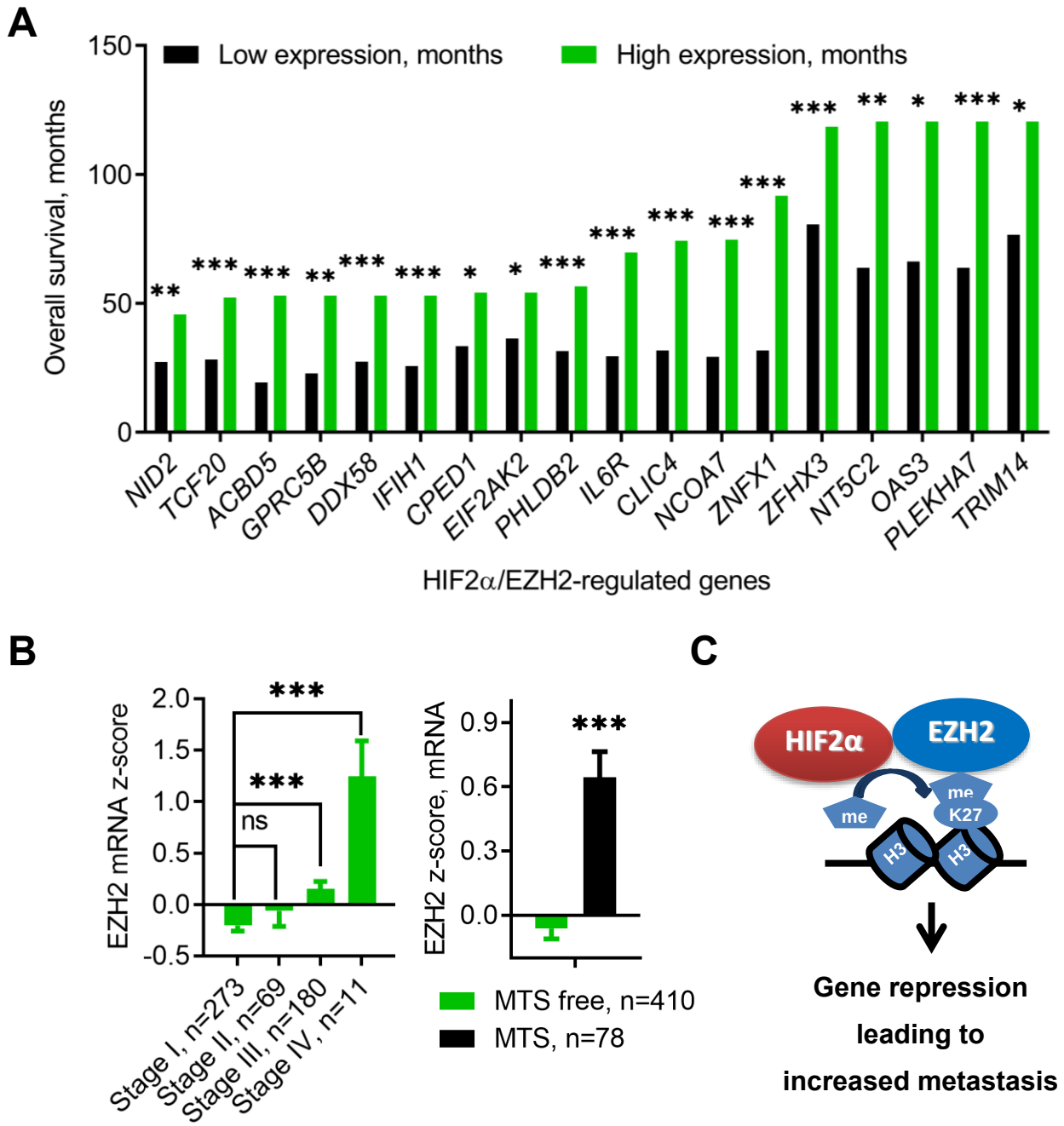

Figure 23. High EZH2 expression and low expression of the identified HIF2α/EZH2 target genes correlate with poor prognosis in RCC patients. A. Analysis of patient survival using the KM-plotter tool showed that ccRCC patients presenting with a low expression of the identified HIF2α/EZH2 target genes have a significantly worse overall survival in comparison to patients with high expression of these genes. **B.** High EZH2 mRNA z-scores correlate with advanced tumor stage and metastasis in ccRCC patients. **C.** Proposed model according to which HIF2α cooperates with PRC2 component EZH2 to downregulate a limited set of genes that leads to increased metastasis.

2.7. Targeting of the PRC2 component EZH2 reduces invasion of WT and QMY HIF2α-overexpressing ccRCC cells

To further validate our hypothesis, we performed experiments where EZH2 activity was reduced either by inhibitor treatment, or through targeting of EZH2 with a siRNA, which we predicted to result in decreased invasion of tumor cells in the modified Boyden chamber assay.

First, we tested whether inhibition of EZH2 would reduce the levels of H3K27me3 in control, WT or QMY HIF2α-overexpressing ccRCC cells. Treatment of cells with 5 μM GSK343 resulted in a pronounced reduction in H3K27me3 levels compared to DMSO-treated controls as verified by immunoblots (Fig. 24A).

Importantly, protein levels of neither HIF2α, nor EZH2 were altered upon inhibitor treatment suggesting that expression of these proteins does not itself dependent on gene silencing by H3K27me3. Residual HIF2α protein in the control reflects the endogenous protein.

Inhibition of EZH2 activity for 96 hours resulted in a significant reduction of invasion of A498 and 786O cells overexpressing the WT and QMY HIF2α compared to the DMSO-treated controls (Fig. 24B). Interestingly, invasion was significantly more suppressed in A498 cells compared to the 786O line suggesting that A498 cells are more dependent on the H3K27me3-mediated gene silencing for maintaining their invasive phenotype.

Next, we explored if targeting EZH2 with a siRNA would result in a similar reduction of invasion. Immunoblots from total lysates of 786O cells 72 hours post transfection confirmed a pronounced reduction in EZH2 and as a consequence – also diminished H3K27me3 levels (Fig. 24C). In the Boyden chamber invasion assay we observed a significantly decreased invasion of QMY HIF2α overexpressing cells compared to the control cells that were transfected with a non-

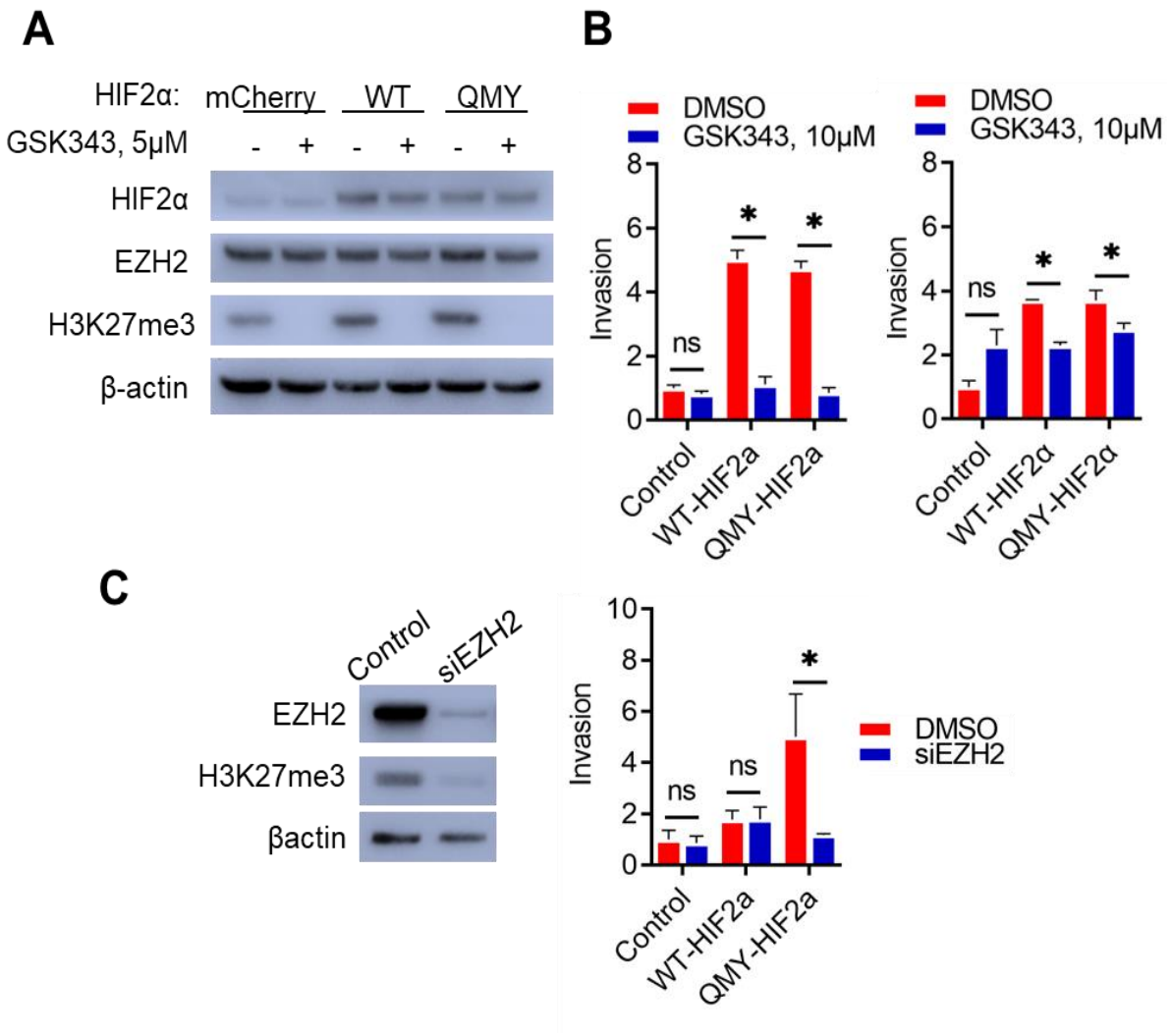

Figure 24. Inhibition of EZH2 enzymatic activity or EZH2 targeting with a siRNA suppresses invasion of QMY and WT HIF2α overexpressing ccRCC cells. A. EZH2 inhibitor GSK343 significantly reduces H3K27me3 levels in A498 stably expressing the mCherry-control, HA-tagged WT or QMY HIF2α. Cells were treated for 4 days with 5 μM GSK343 prior to analysis. Total cell lysates were subjected to immunoblotting with indicated antibodies. **B.** Inhibition of EZH2 in A498 (left) and 786O (right) cells overexpressing either the WT or QMY HIF2α leads to a significant reduction in invasion. Modified Boyden chamber invasion assay was performed using cells treated with GSK343 as indicated in A. Error bars represent standard error of the mean of three biological replicates. **C.** Targeting EZH2 with a siRNA results in reduction of EZH2 and H3K27me3 levels (left) and decreased invasion of 786O cells overexpressing the QMY HIF2α mutant. Three days after siRNA transfection total cell lysates were subjected to immunoblotting with the indicated antibodies. Modified Boyden chamber invasion assay performed with cells 72 hours post-transfection. Error bars represent standard error of the mean of three biological replicates. *$p<0.05$

targeting siRNA (Fig. 24C, right). In this experiment we observed a high variation in the number of WT HIF2α invading cells after targeting EZH2, which proved to be statistically insignificant in comparison to the NTC-control.

Overall, these data show that targeting of the EZH2 or inhibition of its enzymatic activity results in a significant reduction of invasion in ccRCC cells overexpressing the WT and QMY HIF2α, but not in control cells.

2.8. Identification of WT and QMY HIF2α interacting partners

2.8.1. HIF2α localization is not restricted to the nucleus

HIF2α has already been shown to possess some non-canonical ARNT-independent functions, for example in controlling translation of multiple proteins, facilitating cilia formation during inflammation, or microtubule organization in renal cancer (85, 89, 96, 139). Hence, in the current study we aimed to investigate whether disruption of the HIF2α/ARNT heterodimer would result in the redirection of HIF2α to other pathways that ultimately lead to invasion and metastasis.

Despite the identified collaboration between HIF2α and EZH2 in gene repression by chromatin modification in the nucleus, we believe that HIF2α could play some significant functions in other compartments of the cell. To explore such a possibility, we first tested whether HA-tagged WT and QMY HIF2α could be localized somewhere beyond the nucleus. For that, we performed immunostaining with an anti-HA antibody and compared the localization of both proteins in ccRCC and CRC cells. Resultantly, we could detect a strong cytoplasmic signal of both WT and QMY HIF2α in the tested cell lines (Fig. 25A, B). The staining proved to be highly specific since the signal was not observed in mCherry-expressing or other control cells (Fig. 25A, B, upper rows).

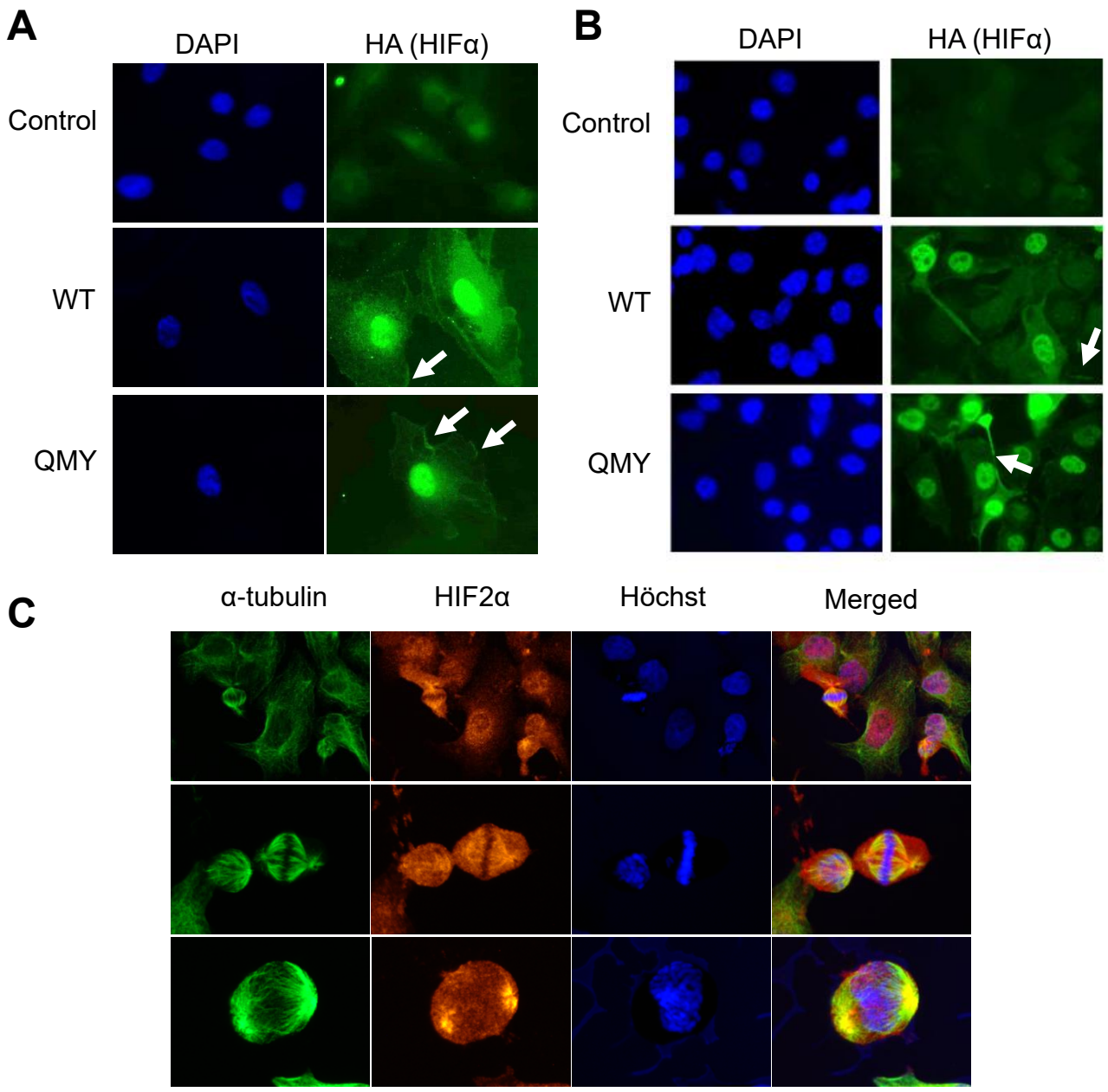

Figure 25. HIF2α localization is not restricted to cell nuclei. A. QMY and WT HIF2α proteins are localized in various compartments of in the cell. A498 cells stably expressing the indicated HIF2α protein were seeded on coverslips, fixed, and stained for HIF2α with the anti-HA antibody and DAPI. 60 x. **B.** MCO2 cells showing nuclear and cytoplasmic localization of both HIF2α versions. Cells were pre-treated with 100 μM DFO to allow for QMY and WT HIF2α accumulation. Immunofluorescent staining done with the anti-HA antibody and DAPI. 60 x. **C.** Hela cells after being allowed to re-enter mitosis following 16 hours of treatment with 9 μM of the CDK1 inhibitor RO-3306. Immunostaining with anti-HIF2α and anti-α-tubulin antibodies. Mitotic nuclei were stained with Höchst. Confocal microscopy, 40 x.

Interestingly, in accordance with the previously published data we could see that both WT and QMY HIF2α-overexpressing cells are associated with the primary cilia (Fig. 25B, indicated with white arrows). In addition, we observed an accumulation of HIF2α at the edges of cells which was also not evenly distributed along the perimeter, but rather shifted to one or the other pole of the cell (Fig. 25A). Such a polarized pattern is characteristic of the focal adhesions suggesting that HIF2α might be associated with these structures. Importantly, we could observe that both WT and QMY HIF2α showed a similar pattern of distribution in the cells.

Collectively, these results suggest that after disrupting the HIF2α/ARNT heterodimer HIF2α might become involved in other pathways that regulate invasion of tumor cells. In addition to cilia, we could also record the association of endogenous HIFα with mitotic spindles and microtubules of dividing cells (Fig. 25C). This was the case, for example, in HeLa cells entering mitosis after an arrest in the G2 phase.

Overall, these results suggest that HIF2α might not only participate in transcriptional regulation of tumor cell invasion, but that it might also become a part of other protein complexes which regulate cell proliferation, and possibly also invasion and migration.

2.8.2. Identification of WT and QMY HIF2α interacting partners by mass spectrometry

Considering the possible role of HIF2α outside the cell nuclei, we decided to identify all HIF2α interacting partners by the interaction with which HIF2α could exert its transcription-independent functions. For that, we first performed a series of experiments to optimize conditions for concentrating the HIF2α protein. 786O and HCT116 cells overexpressing WT and mutants of HIF2α were taken for this

purpose. In addition to QMY, we also decided to analyze the bHLH-deficient HIF2α mutant: since the bHLH mutant would not interact with the chromatin this could aid in the identification of HIF2α interacting partners that act independently of DNA binding.

To concentrate HIF2α protein, we performed immunoprecipitation with anti-FLAG antibody in lysates of HCT116 cells which were pretreated overnight with DFO before the pulldown. We managed to concentrate a reasonable amount of HIF2α protein that was detectable after SDS-PAGE electrophoresis followed by a Coomassie stain (G250 brilliant blue) of the gel. Pulled down HIF2α was detected as a band at the protein size corresponding to 115 kDa (Fig. 26A). Immunoblots verified that the pulldown was specific for HIF2α since we could easily detect the co-immunoprecipitated ARNT as a typical interacting partner, which indicates that the protein-protein interactions were preserved (Fig. 26B).

As the next step, we prepared anti-HA pulldowns to concentrate HIF2α from 786O cells. SDS-PAGE with subsequent Coomassie stain of the resulting gel did not show a dramatic accumulation of HIF2α at the expected size (Fig. 26C). Despite this fact, immunoblots showed significant enrichment for HIF2α protein after immunoprecipitation, as well as the co-precipitated ARNT protein (Fig. 26D). Therefore, we subjected the immunoprecipitates derived from HCT116 cells with WT, QMY, and bHLH mutants of HIF2α for further mass spectrometric analysis.

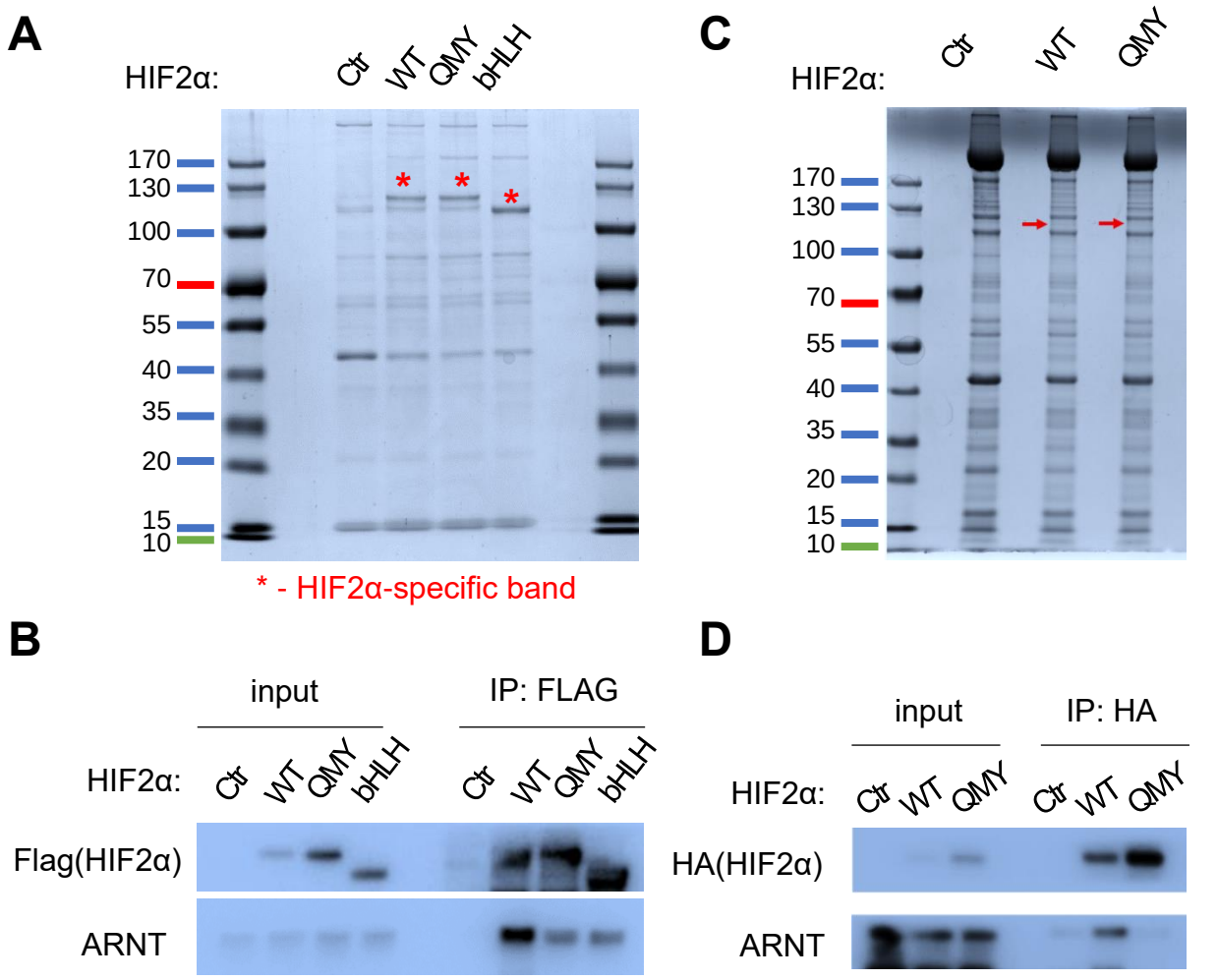

Figure 26. Identification of HIF2α interacting partners by mass spectrometry. A. Pull down of the WT, QMY, and bHLH HIF2α proteins. HCT116 cells were generated to stably overexpress FLAG-tagged HIF2α proteins. Cells were treated overnight with 100 μM DFO to allow for HIF2α accumulation. Cells were lysed in non-denaturing conditions and immunoprecipitated with the anti-FLAG antibody. The eluate was subjected to immunoblotting and the resulting gel stained with Coomassie. **B.** Verification of the FLAG-pulldown of HIF2α proteins by immunoblotting. ARNT was used as a positive control. **C.** Pulldown of endogenous WT and QMY HIF2α in ccRCC cells. 786O cells stably expressing indicated HIF2α proteins were lysed in non-denaturing conditions and immunoprecipitated with anti-HA conjugated dynabeads. The eluate was subjected to immunoblotting and the resulting gel stained with Coomassie. **D.** Verification of the HA-pulldown by immunoblotting. Co-immunoprecipitated ARNT was used as a positive control of a HIF2α interacting partner in immunoblotting.

2.8.3. Mass spectrometry identifies common interacting partners between WT, QMY, and bHLH HIF2α proteins

Mass spectrometric analysis of immunoprecipitated HIF2α from HCT116 cells was performed in collaboration with Prof. Andreas Schlosser at the core mass spectrometry facility at the Rudolf-Virchow center (RVZ) in Würzburg. Eluted proteins were fragmented by tryptic digestion and subjected to mass spectrometry. To determine the proteins enriched in FLAG-pulldowns of WT, QMY and bHLH mutants of HIF2α, each sample was first normalized to the pulldowns from control cells transduced with an empty vector.

In the end, we could identify over 52 proteins interacting with WT, QMY and bHLH HIF2α with a significance value of 1 and 2 comprising 26.3 % of all identified interactors. The numbers of interacting proteins varied depending on the exact sample with a maximum of 174 in the case of bHLH HIF2α, 131 in QMY HIF2α, and 63 interacting partners with the WT HIF2α (Fig. 27A). When we apply more stringent criteria of selection, 25 interacting proteins comprising 17.2 % of the whole interactome are found as common binders. With such settings, the QMY mutant has slightly more interactors compared to bHLH, comprising 121 and 114 proteins respectively, with only 27 proteins in the case of WT HIF2α.

Such a significant variation between the samples might be explained in part by differences in protein expression (Fig. 27B), but also due to a different efficiency of the pulldown: in general, protein levels of the bHLH mutant were lower than that of the QMY or WT HIF2α, but after immunoprecipitation became higher compared to the other HIF2α proteins as detected by the Coomassie stain (Fig. 27A). This indicates that bHLH was more efficiently pulled down with the anti-FLAG antibody, which might in turn result in the identification of a greater number of interacting partners. Alternatively, QMY or bHLH mutants might be more accessible to the FLAG antibodies compared to the WT protein. In addition, the

bHLH mutant is expected to possess a slightly different interactome since it has a much weaker (or most probably no) DNA binding capacity.

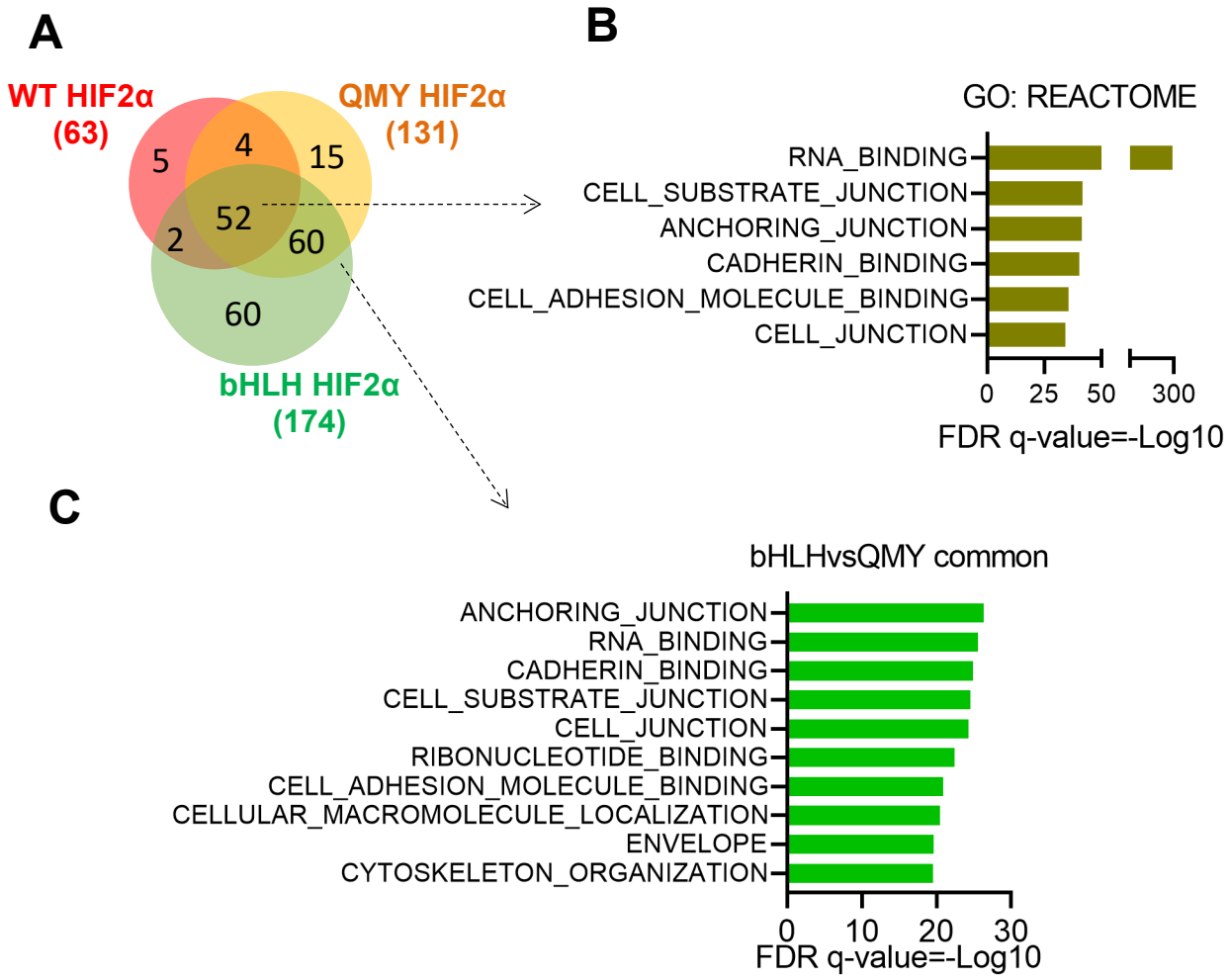

Figure 27. Mass spectrometry identifies common interacting partners of WT, QMY, and bHLH HIF2α. A. Venn diagram showing the number of unique and shared proteins between the WT, QMY, and bHLH HIF2α. Identified proteins were normalized to the immunoprecipitate from control cells. **B.** Functional classification of the identified proteins shared by the WT, QMY, and bHLH HIF2α based on gene ontology. Most of the identified interacting partners are related to regulation of translation, anchoring, extracellular matrix organization, cell contacts, and adhesion. **C.** Functional classification of the 212 proteins interacting only with QMY and bHLH HIF2α based on gene ontology (GO: REACTOME).

Next, we performed a gene set enrichment analysis to identify the pathways where ARNT- and DNA-independent HIF2α proteins are involved by employing the "Gene ontology: Reactome" and "Panther: Protein class" databases. Most

significantly enriched among the interacting partners were proteins from the RNA-binding and translation regulatory pathways. In addition, several other protein groups were represented including some members of the cytoskeleton, cell adhesion, and extracellular matrix (Fig. 27B). Based on these results, we may speculate that HIF2α contributes to tumor cell invasion and metastasis by regulating pathways which require neither ARNT, nor DNA binding.

2.8.4. Identification of the top significant interacting proteins regulating cell adhesion common to both WT and QMY HIF2α

Having identified the broad spectrum of all interacting partners of HIF2α, we wanted to narrow down the list of potential invasion- and metastasis-associated proteins to those which are interacting with HIF2α independently of ARNT. We found clathrin, δ-catenin (CTNND1), and IQGAP3 among the top significant interacting proteins shared by WT, QMY, and bHLH HIF2α (Fig. 28), all of which were previously implicated in controlling metastasis. Interestingly, after comparing the QMY and bHLH HIF2α interactomes, clathrin and catenin groups were found to be represented by several members, including alpha- and beta-catenin, as well as E-cadherin (CDH1). This result suggests that free HIF2α (which is not bound to DNA or ARNT) would efficiently interact with cell adhesion- and extracellular matrix-associated proteins and thus exert a strong impact on tumor cell invasion and metastasis.

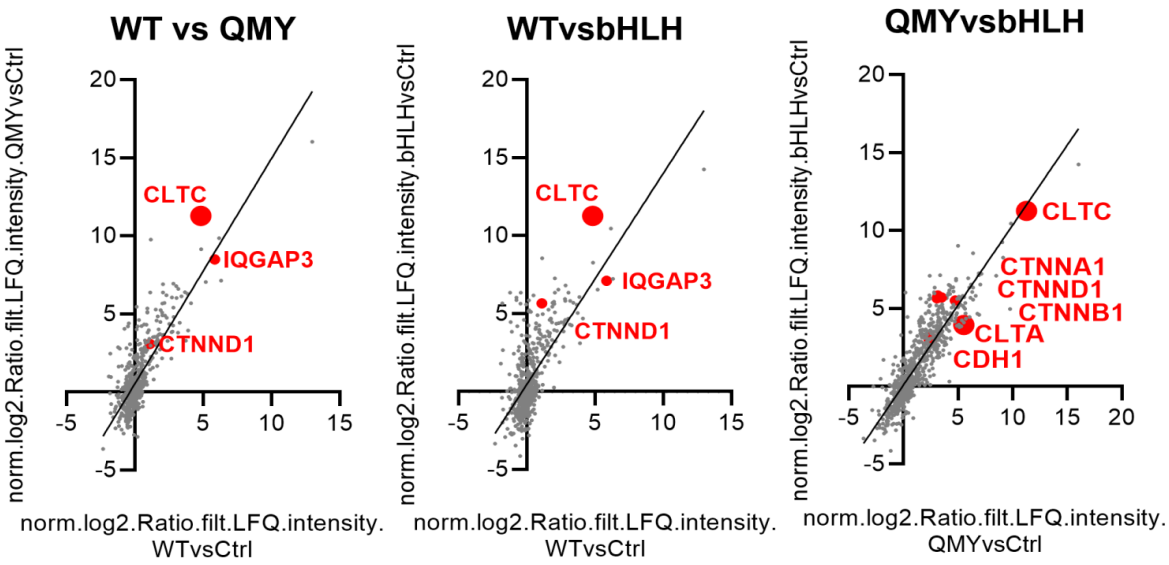

Figure 28. Identification of common WT and QMY HIF2α interacting proteins regulating cell adhesion. Normalized protein ratios showing the most significant interacting partners with the WT, QMY, and bHLH HIF2α. Identified proteins were normalized to the empty vector control sample. Each point represents a single protein. δ-catenin and IQGAP are among the top interacting partners upregulation of which is associated with tumor invasion and metastasis.

2.8.5. WT and QMY HIF2α interact with p120 in RCC cells

As the next step, we wanted to validate the identified HIF2α interaction partners described in the previous section in ccRCC cells. For this, immunoprecipitation of HA-tagged HIF2α with anti-HA beads was performed in 786O cell lysates. Immunoblots showed efficient co-precipitation of δ-catenin (p120) which was similar between WT and QMY HIF2α-overexpressing cells. Co-precipitation of IQGAP was comparatively weaker, but still comparable between the WT and mutant HIF2α (Fig. 29A). Interaction with clathrin could not be verified in either WT or QMY HIF2α, which indicates that in ccRCC 786O cells HIF2α interactome might be different from that in HCT116 cells and should be thoroughly verified across different tumor types.

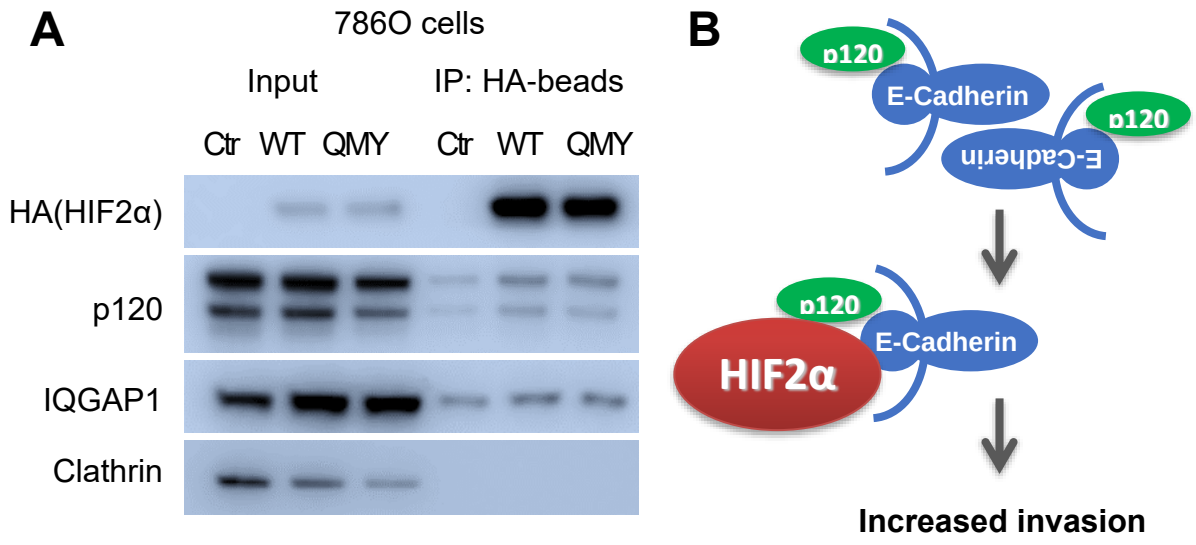

Figure 29. Validation of some of the identified common WT and QMY HIF2α interacting partners in 786O cells. A. Validation of mass spectrometry results in 786O cells confirming δ-catenin (catenin D1, p120) and IQGAP interaction with WT and QMY HIF2α. Immunoblots made from eluates after anti-HA pulldown from cell lysates in non-denaturing conditions. Cells expressing mCherry were used as a negative control. **B.** Suggested model of HIF2α-dependent regulation of invasion and metastasis through the interaction with catenin D1 and E-cadherin.

To sum up, based on the validation results we believe that HIF2α binding to delta-catenin as the common interaction partner in both CRC and RCC cells represents an important regulatory mechanism how HIF2α contributes to tumor invasion and metastasis in an ARNT-independent manner.

2.8.6. β-Catenin shows decreased half-life in HIF2α-proficient cells

One of the central functions of p120 is to regulate stability and membrane localization of the entire cadherin-catenin complex (165, 166). E-cadherin is one of the crucial components of adherens junctions and is known to accumulate at cell-to-cell contacts. Therefore, we set out to test how interaction of HIF2α with p120 or catenin family members that was detected by mass spectrometry and verified in co-immunoprecipitation would affect the cadherin/β-catenin complex.

For this, we examined E-cadherin and β-catenin protein half-life in HIF2α-proficient and deficient cells in a cycloheximide decay assay. Protein half-life was determined by addition of the protein translation inhibitor cycloheximide for several time points. Thereby, new protein synthesis was blocked and thus the turnover rate of a protein could be estimated by immunoblot analysis.

HCT116 cells were pretreated with $CoCl_2$ to chemically mimic hypoxia, followed by the cycloheximide decay assay. Cobalt can inactivate the proline hydroxylase enzymes by occupying their iron-binding site and in addition can also bind directly to HIF2α at the pVHL-binding site resulting in stabilization of the HIF2α protein (167) As we expected, E-cadherin and β-catenin were rapidly degraded in HIF2α-proficient HCT116 cells compared to HIF2α CRISPR knockout cells as can be seen by the decreasing levels of both proteins over time shown by immunoblotting (Fig. 30A).

WT and QMY mutant HIF2α were also shown to regulate the stability of β-catenin in A498 ccRCC cells. Particularly, we observed an even more intense degradation of β-catenin in QMY HIF2α-overexpressing cells compared to cells with WT HIF2α or in the control (Fig. 30B).

Interestingly, similar results to the QMY HIF2α were observed in cells treated with the PT2385 inhibitor where the turnover rate of β-catenin was higher compared to DMSO-treated or pVHL-reconstituted cells. Importantly, pVHL reconstitution resulted in increased overall levels and higher stability of β-catenin. We speculate that upregulation of β-catenin in this context might lead to suppression of migration and invasion. This effect might be due to reduced β-catenin-mediated transcription or destabilization of the anchoring junctions, with both hypotheses requiring further investigation.

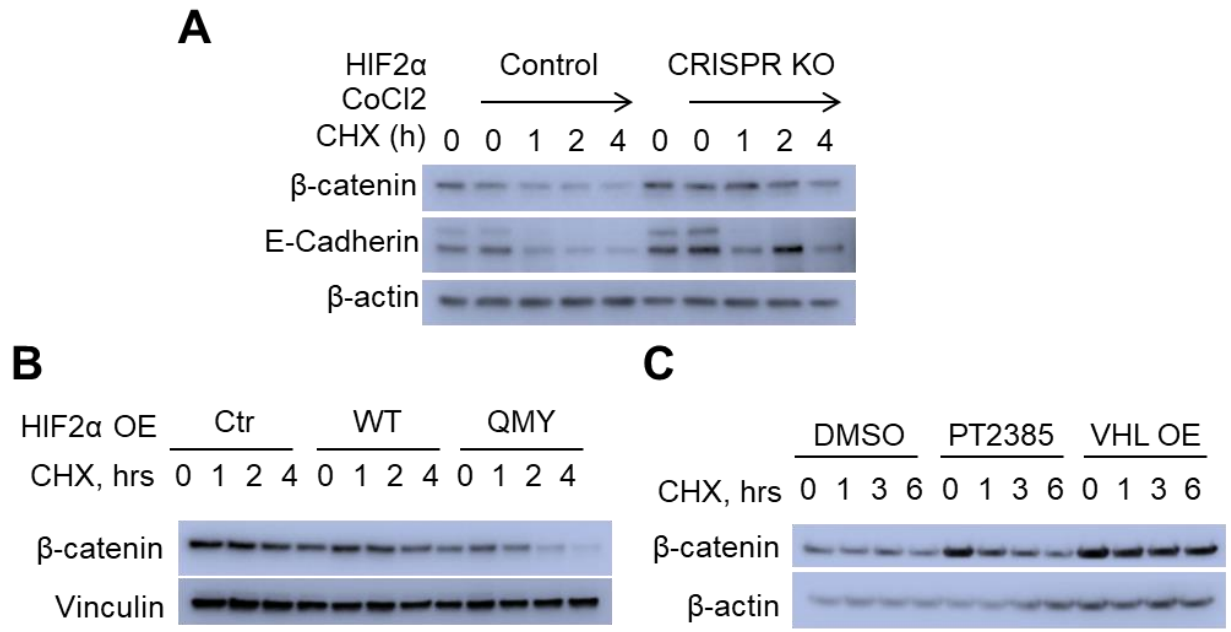

Figure 30. β-catenin shows decreased half-life in HIFα-proficient cells. A. Cycloheximide decay assay in control and HIF2α CRISPR KO HCT116 cells. Cells were pretreated with $CoCl_2$ followed by the incubation with cycloheximide for the indicated timepoints. Cells were lysed and analyzed by immunoblotting with the indicated antibodies. **B.** Turnover of β-catenin proved to be higher in WT and QMY HIF2α-overexpressing A498 cells than in the control line. Cells were treated with cycloheximide for the indicated timepoints. Total lysates were analyzed in immunoblotting with the indicated antibodies. **C.** Turnover of β-catenin increases after treatment with the PT2385 inhibitor. A498 cells were treated with 0.5 μM PT2385 overnight and then subjected to cycloheximide decay assay. pVHL-reconstituted cells which served as a HIF2α-deficient control showed much higher β-catenin levels with no apparent change in its turnover. Total lysates were analyzed by immunoblotting with the indicated antibodies.

Curiously, treatment with the PT2385 inhibitor initially elevated the levels of β-catenin, nevertheless the protein proved to be highly unstable and its levels were rapidly reduced to those observed in untreated HIF2α-proficient cells.

Overall, these results suggest that HIF2α can induce degradation of β-catenin and E-cadherin independently of ARNT binding and that this regulatory loop might be even more enhanced when excess of ARNT-free HIF2α is available. Thus, we speculate that HIF2α regulates motility and invasion also through mediating β-catenin turnover.

3. Discussion

Mechanisms that enable clear cell renal carcinomas as well as other hypoxia-driven tumors to invade and metastasize remain to be fully elucidated. In this study we show that HIF2α controls tumor invasion apart of its major ARNT-dependent transcriptional activity by recruiting the PRC2 component EZH2, as well as through a non-transcriptional mechanism by destabilization of the E-cadherin/β-catenin complex. Pharmacological inhibition of EZH2 activity in ccRCC cells resulted in a significant reduction of invasion *in vitro* which was in striking contrast to HIF2α-ARNT inhibitors or direct targeting of ARNT, neither of which showed any effects. Consequently, we hypothesize that dissociation of HIF2α from ARNT may even result in enhanced invasion and metastasis by involvement of alternative pathways that do not require its transcriptional activity.

3.1. HIF2α rather than pVHL controls invasion in ccRCC and CRC cells

One of the major goals of this study was to investigate the mechanisms of HIF2α-driven invasion in ccRCC and CRC cells. Preliminary analysis of the TCGA database revealed that pVHL loss of function does not significantly correlate with the metastatic status in ccRCC patients (data not shown). This observation is in line with previous reports (28, 52, 98, 168), suggesting that RCC invasion and metastasis are regulated by several mechanisms, and that pVHL cannot be considered as the most robust prognostic factor. Nonetheless, since pVHL is primarily known to regulate degradation of the hypoxia inducible factors (169), and considering that HIF2 is known as the predominant HIF isoform in renal cancer (52, 81), we assessed whether HIF2α is driving invasion and metastasis. First, we reconstituted several established ccRCC lines that harbor a loss of *VHL* with a functional pVHL protein and observed significantly reduced invasion of the

reconstituted lines *in vitro*. A similar reduction in invasion was observed with a constitutive HIF2α knockdown in pVHL-deficient cells. Moreover, this effect could not be further enhanced even upon a HIF2α knockdown in pVHL-reconstituted cells, suggesting that HIF2α, but not pVHL, is the main determinant of invasion in RCC cells. These results are in line with previous publications where HIF2α was reported to regulate invasion by activation of EMT (34, 170, 171), supporting the notion that pVHL is only contributing to invasion via the regulation of HIFs (98, 99).

It is well established that HIF2α forms a heterodimer with ARNT to transcriptionally activate various downstream target genes and thus fuel tumor progression (13, 45, 80). Hence, several inhibitors were developed to disrupt the heterodimer and repress the downstream target genes (48, 81, 117). Application of these inhibitors in mouse orthotopic or xenograft models of kidney cancer resulted in reduced primary tumor growth and in some cases even tumor regression. However, in the recent clinical trials (e.g., ClinicalTrials.gov, NCT03401788) these inhibitors have not meet the expectations so far (7, 120), which is possibly linked to their low activity against metastatic tumors. Considering that nowadays cancer patients primarily die of metastases, but not the primary tumor (168, 172, 173), we raised the question if dissociation of HIF2α from ARNT would affect invasion and metastatic dissemination.

3.2. HIF2α promotes invasion and metastasis in an ARNT-independent manner

Several groups have previously reported that treatment with HIF2 inhibitors results in decreased HIF2α downstream target gene expression, reduced proliferation, and delayed tumor growth *in vivo* (17, 48, 81, 100, 161). In this project we aimed to

study the impact of these inhibitors on cancer cell invasion and metastasis. For this, first we titrated the PT2385 HIF2α/ARNT inhibitor and could confirm an efficient and dose-dependent disruption of the heterodimer formation in several RCC lines. Indeed, expression of the HIF2α downstream targets, such as the glucose transporter GLUT1, pro-angiogenic factor VEGFA, stem cell and cell cycle regulator Oct4, and CCND1 became significantly reduced in response to PT2385 treatment. Nevertheless, disruption of the HIF2 heterodimer by either the PT2385, or a more potent inhibitor PT2399 (81, 117) had no effect on invasion or migration in the tested ccRCC cells. One possible explanation for this, of course, could be that these inhibitors only partially repressed the downstream HIF2α target genes, since even increased concentrations of the applied drugs could not further reduce mRNA levels of most of these genes to the levels observed in pVHL reconstituted cells.

To exclude the possibility that invasion of the tumor cells was sustained due to an incomplete inhibition of HIF2α/ARNT-mediated transcription of some downstream targets, we generated the QMY HIF2α mutant that is incapable of binding ARNT. Selection of the amino acids to be mutated was based on the recently published HIF2α/ARNT heterodimer crystal structure where three crucial residues required for the interaction were described (160). Hence, this allowed us to generate a purely genetic model to study the role of HIF2α/ARNT-mediated transcription in invasion of mouse and human ccRCC and CRC cells. Importantly, in our experiments we overexpressed the QMY and WT HIF2α on top of a knockdown or CRISPR KO of the endogenous *EPAS1*. Surprisingly, overexpression of the QMY HIF2α mutant promoted invasion to the same extent as the wild type version of the protein. Moreover, we also observed a significantly increased invasion of CRC cells upon the overexpression of a HIF2α mutant that lacks a DNA-binding domain (the bHLH mutant). From these experiments we may conclude that first, HIF2α is

driving tumor cell invasion in an ARNT-independent manner, and second, that HIF2α might employ several pathways (including DNA-binding independent ways) to regulate invasion. The latter hypothesis is supported by the observation that invasion of the bHLH mutant was increased in comparison to the control, but lower than that in the QMY mutant. Based on these findings we might envisage two different explanations how HIF2α regulates invasion: by transcriptional regulation through cooperation with other transcription factors, or by transcription-independent mechanism/s.

Overall, the obtained results were surprising in light of the publications describing the activation of EMT by the HIF2α/ARNT heterodimer which was assumed to be the mechanism how HIF2α regulates tumor cell invasion (13, 51, 64, 69, 75, 78, 119, 125, 174). Therefore, we decided to directly interrogate the role of the second subunit in the heterodimer, ARNT, by targeting the protein with a shRNA. In line with the previous findings, targeting of ARNT did not reduce invasion. In fact, we even observed a slight, but statistically significant increase in invasion of QMY and WT HIF2α-overexpressing cells upon the knockdown of ARNT. This result corresponds to the published data showing that downregulation of ARNT promotes metastasis in colorectal cancer by activating the fibronectin/integrin β1/FAK axis (174).

Having established that HIF2α regulates tumor cell invasion in an ARNT-independent manner *in vitro,* we investigated the possibility whether this was also true for metastasis *in vivo.* To address this question, we employed three mouse metastasis models: a spontaneous and passive metastasis model with human 786O ccRCC cells, and one CRC model of passive metastasis using the MCO2 mouse colorectal carcinoma line.

In accordance with the obtained *in vitro* data, we observed that cells overexpressing the QMY mutant of HIF2α could efficiently colonize the lungs after an orthotopic

transplantation of 786O cells into the kidney, or the liver in the splenic seeding passive metastasis model. Nevertheless, experiments with the 786O human RCC cells proved to be inconclusive since in the model of passive metastasis increased lung colonization was observed only in WT HIF2α-overexpressing cells, while the number of metastatic nodules formed by QMY HIF2α-overexpressing cells was similar to the control group. Naturally, spontaneous metastasis models are in general more physiological and clinically relevant since they encompass all the metastasis steps (from the primary tumor growth, invasion, and intravasation, to the formation of macrometastasis), in contrast to passive metastasis models which recreate only the last steps in metastasis and lack all the initial stages (34, 99, 175).

Overall, based on the obtained results we may speculate that the QMY mutant promotes metastasis to a much higher degree than the WT HIF2α which could not only explain the poor clinical results with the HIF2 inhibitors, but also hint at a specific resistance mechanism to this class of drugs. However, additional *in vivo* studies are required to conclusively explore this phenomenon. First of all, seeding conditions (time and cell number) in the next experiments would have to be optimized since much fewer numbers of macroscopic lung nodules were observed in the passive metastasis model than in spontaneous metastasis. Lastly, detailed histological assessment is required to assess the full degree of lung colonization in each model of ccRCC since micrometastases which are invisible to the naked eye could not be accounted for.

Strong supportive evidence for the hypothesis that HIF2α controls metastasis in an ARNT-independent manner was obtained with MCO2 cells in the passive CRC liver metastasis model. Here, overexpression of the WT or QMY HIF2α was shown to equally increase liver colonization, which in both cases was significantly higher in comparison to the control cells. The fact that much stronger results were observed with the syngeneic MCO2 cells than with the xenografted ccRCC cells

might be explained by the contribution of the local immune microenvironment to metastasis formation in the syngenic system. Hypoxia was previously shown to suppress immune cell functions and thus promote primary tumor progression and metastasis. For example, in several previous reports it was shown that tumors can induce a pre-metastatic niche by creating a local immunosuppressive microenvironment (e.g. by recruitment of T regulatory cells, T-reg) and by inducing the M2 pro-tumorigenic polarization of the tumor associated macrophages, with both processes being mediated by HIF1/2α (38, 176). In particular, the hypoxic tumor microenvironment stimulates the production of interleukin-10 (IL-10) and CCL-2, and 15-lipoxygenase-2 (15-LOX2) by macrophages, while T-reg cells were shown to significantly suppress the activity of CD4+ T cells under hypoxic conditions (4, 177). In addition, HIFs can support the inflammatory micromilieu that facilitates tumor cell invasion, for example by inducing pro-inflammatory cytokine secretion, such as TNFα and MCP-1 in tumor-associated monocytes (12, 142, 178). Moreover, HIFs can influence the expression of many pivotal transcription factors, effectors, and inhibitory signals in cytotoxic CD8+ T-cells thus contributing the tumor immune escape and progression (66).

Considering the severe immunodeficiency of the NSG mice used in the experiments with human 786O cells (lack of mature T and B cells, NK killer cells, impaired macrophage and dendritic cell activity, multiple deficiencies in cytokine signaling pathways (179), we cannot exclude the possibility that the expected effects of the WT and QMY HIF2α were blunted due to the absence of the pro-tumorigenic support from local immune cells. Thus, it would be highly interesting to repeat the *in vivo* studies with a syngeneic ccRCC model. Unfortunately, at present no mouse renal tumor models are available that would fully recapitulate the phenotype of human ccRCCs. One of the few transplantable models available is based on the orthotopic transplantation of RenCa cells in immune competent

BALB/c mice (175, 180). However, when tested in immunoblot, these cells showed high levels of expression of the functional pVHL, high protein levels of HIF1α, but no detectable HIF2α protein (data not shown). Based on these molecular features which clearly set this line apart from typical human RCC tumors, we decided against using these cells in our *in vivo* studies.

Overall, our *in vivo* data strongly indicate that HIF2α does not only drive invasion, but also metastasis in an ARNT-independent manner. In the next sections we will explore the mechanisms by which HIF2α promotes metastasis focusing on the ARNT-independent transcriptional gene regulation, and non-transcriptional (protein-protein mediated) mechanisms governing tumor cell invasion and metastasis.

3.3. HIF2α/ARNT heterodimer-independent genes are crucial for tumor invasion and metastasis

HIF2α is thought to primarily control transcription by forming a heterodimer with ARNT (7, 17). Therefore, high expectations were raised after the development of inhibitors that disrupt the heterodimer regarding their potential as chemotherapeutic agents (81, 117, 161). Indeed, qPCR analysis in A498 and 786O cells treated with PT2385 revealed a significant repression of some published HIF2α target genes, while response of other genes was different between the lines. Interestingly, expression of a significant fraction of the tested genes was unaffected by the treatment. The latter finding is an indication that genes that control invasion and metastasis might be independent of the HIF2α/ARNT heterodimer. Therefore, to identify the HIF2α-dependent genes that control tumor invasion and metastasis we performed RNA sequencing with control and PT2385-treated cells. The rationale

behind this experiment was that inhibitor treatment would enable us to exclude the genes that are not essential for invasion.

As expected, gene set enrichment analysis of RNA-Seq results from PT2385-treated cells and cells harboring a HIF2α knockdown revealed many classic hypoxia response genes to be downregulated, e.g. genes involved in glycolysis, angiogenesis, and cancer stem cell genes. Interestingly, a substantial fraction of the deregulated genes was unaffected by the inhibitor but responded to the knockdown. This data is in line with a recently published study by Person et al. showing that ARNT-dependent HIF2α transcriptional activity cannot explain the full HIF2α-controlled transcriptional profile observed in neuroblastomas (119). Curiously, mRNA levels of CXCR4, a gene which was recently published to regulate metastasis of 786O cells *in vivo* (98), were repressed by both PT2385 treatment and HIF2α knockdown. Nonetheless, since PT2385 did not affect invasion in the matrigel assay in contrast to the significantly reduced invasion upon the HIF2α knockdown, we could not confirm CXCR4 as a major factor in controlling the invasive phenotype in RCC cells. In contrast to CXCR4, many known regulators of invasion and metastasis, including metalloproteinases, adhesion and anchoring proteins remained unaffected by the PT2385, but were responsive to the HIF2α knockdown.

To further corroborate the list of ARNT-independent HIF2α target genes, we performed RNA-Seq on cells overexpressing the WT or mutant versions of HIF2α. Here, we observed a significant portion of the genes to be commonly regulated by WT HIF2α and the QMY mutant. Since the QMY-overexpressing cells showed invasion equal to that of cells overexpressing the WT HIF2α, we conclude that HIF2α-dependent genes responsible for invasion are not regulated by the HIF2α/ARNT heterodimer. Considering the fact, that HIFα subunits cannot bind

DNA alone, we reasoned that HIF2α might interact with other transcription factors to promote invasion of QMT-expressing cells.

Interestingly, it has been previously shown that HIF1α functionally cooperates with c-Jun to induce expression of many known hypoxia-regulated genes (181, 182), and binds p53 resulting in transcriptional regulation of extracellular matrix components and tumor progression (183). We cannot exclude the same for HIF2α since we could also see quite efficient interaction between HIF2α and c-Jun in co-immunoprecipitation assays (data not shown). In support of our findings, ChIP sequencing published by several groups indicates that c-Jun and HIF2α have similar DNA-binding motifs and that c-Jun as an enhancer protein directly interacts with HIF2α (11, 28, 35, 176). Additionally, HIF2α was shown to cooperate with other transcription factors, such as c-Myc, FOXO1, or SMAD (11, 26, 27, 181). For example, it was shown that HIF2α stabilizes c-Myc/Max complexes promoting c-Myc binding to DNA at E-boxes and resulting in an enhanced transcriptional activity and cell proliferation under hypoxia in RCC tumors and multiple other cell lines (64). Later it was also shown that c-Myc binds HIF2α to regulate downstream targets which maintain self-renewal in cancer stem cells via Nanog and Sox2 (113). Curiously, neither of the studies where HIF2α was shown to interact with other transcription factors addressed the role of these newly discovered heterodimers in tumor cell invasion and metastasis.

3.4. HIF2α regulates tumor cell invasion by cooperation with the PRC2 component EZH2

To identify the HIF2α interacting partner that mediates tumor cell invasion and metastasis, we performed gene set enrichment analysis of HIF2α-dependent genes that are not affected by the inhibitor, but become upregulated by both WT and

QMY HIF2α overexpression. One of the most significantly deregulated groups among the identified sets of genes were the targets of EZH2 or genes associated with the H3K27me3 repressive histone mark (product of EZH2 enzymatic activity). In addition, analysis of ccRCC and CRC cells showed that pVHL reconstitution and the resulting low HIF2α levels correlate with decreased levels of H3K27me3. Moreover, H3K27me3 levels dropped significantly upon a CRISPR KO of HIF2α in CRC or HeLa cells (data not shown). These results are in line with the previously published reports showing increased H3K27me3 levels in hypoxia (125, 184, 185), although there are also contradicting reports in the literature (104, 132). For example, in a study by Chakraborty et al. the authors showed that pVHL reconstitution increases H3K27me3 levels due to decreased KDM6B demethylase activity in UMRC2 RCC cells (104). In another such study by the Massague laboratory the authors showed increased H3K27me3 ChIP-Seq peaks at *CXCR4* in 786O cells upon pVHL reconstitution, however they did not analyze total H3K27me3 levels (98). In line with our findings, in the study by Liu et al. the authors showed that total H3K27me3 levels are significantly higher in a set of RCC tumors compared to normal tissue samples, leading the authors to suggest H3K27me3 as a diagnostic and prognostic marker in RCC (143). Similarly, other studies noted higher H3K27me3 in association with hypoxia, as in the mouse model of limb ischemia (Mitic et al., 2015), or after exposing MCF7 cells to hypoxia *in vitro* (184, 185). Such discrepancy in the reports promted us to further investigate the role of EZH2 and H3K27me3 in RCC invasion and metastasis. Analysis of mRNA and protein levels of EZH2 and Suz12 (another major component of PRC2) showed no difference in the expression of these genes between control and pVHL-reconstituted ccRCC cells.

In a previous report N-Myc was shown to interact with EZH2 and redirect its activity to N-Myc target genes resulting in the transcriptional repression of the

latter (186). Therefore, we hypothesized that HIF2α could directly interact with EZH2 and similarly to the N-Myc/EZH2 dimer and repress downstream target gene expression. Indeed, we could show that both WT and QMY HIF2α bind to EZH2 (the HIF2α/EZH2 dimers were primarily located in the nuclei of cells as assessed by the PLA assay). Therefore, we suggested a model where HIF2α recruits EZH2 to silence invasion suppressor genes that results in decreased metastasis.

Cooperation between pVHL and PRC2 has already been reported: it was shown that loss of pVHL is associated with enhanced EZH1/2 activity and elevated trimethylation of H3K4/H3K27 (98, 104, 184, 185). In addition, high HIF1α levels were published to correlate with increased EZH2 expression, but low PRC2 activity in triple-negative breast cancer compared to other breast cancer subtypes (132). However, until present there are no studies where direct interaction between HIFs and EZH2 was reported.

To further explore the suggested mechanism, we performed ChIP sequencing with EZH2 and H3K27me3 and found high variability in peak distribution over chromatin on the broad scale with some overlapping and some independent peaks, which is in line with the published data (153, 187, 188). Several identified peaks coincided with the published H3K27me3 peaks identified by ChIP-Seq in 786O cells (98). We observed both acquisition and loss of H3K27me3 marks in pVHL-reconstituted cells compared to the control as was also previously reported by the Tan laboratory (28). Comparing EZH2 and H3K27me3 ChIP-Seq results revealed many overlapping EZH2 and H3K27me3 peaks which indicates the canonical EZH2 function as a conveyor of the repressive histone mark (Wassef et al., 2019). Nevertheless, some H3K27me3 peaks were independent of EZH2 suggesting that those regions might be specifically catalyzed by EZH1, another PRC2 enzymatic component (104, 131). In some rarer cases we observed exclusive EZH2 peaks with no accompanying H3K27me3 marks. The latter might indicate a non-

canonical function of EZH2 as a transcriptional co-activator that is independent of PRC2, a function that has already been reported, yet in all remains poorly studied (130, 134).

To assess if the repressive H3K27me3 marks would translate into decreased gene expression, we overlaid the obtained gene expression profiles from mRNA sequencing with the identified H3K27me3 ChIP-Seq peaks. Admittedly, the correlation between the two datasets proved to be quite heterogeneous with all possible scenarios, e.g. moderate H3K27me3 peaks with low corresponding mRNA levels, or strongly repressed genes showing weak H3K27me3 peaks. These results indicate on the complexity of gene expression regulation, and might be the result of regulation by additional epigenetic machinery, such as histone demethylases (104, 184), or differential recruitment and activity of the PRC1 complex (187).

Next, we focused on identifying the invasion suppressor genes that become repressed by the HIF2α/EZH2 axis by analyzing RNA sequencing results of HIF2a knockdown, WT and QMY HIF2a-overexpressing cells. The suggested mechanism of action of the HIF2α/EZH2 complex would be in line with the current knowledge on canonical EZH2 functions in gene silencing as a component of the polycomb group protein 2 repressor machinery (129, 132, 189).

By integrating all the ChIP-Seq data with mRNA-Seq results we could identify the common HIF2α/EZH2 regulated genes which according to the canonical function of EZH2 would become suppressed by the HIF2α/EZH2 heterodimer. To support the hypothesis that these are also the HIF2α-regulated genes that contribute to tumor invasion and metastasis, we performed database analysis using the publicly available TCGA repository. Particularly, we could show that patients with low expression of the identified genes showed significantly decreased overall survival. In addition, when segregated by their metastatic status, patients with metastases showed a significantly increased EZH2 mRNA z-scores than metastasis-free

patients. Role of EZH2 in cancer as a repressor of tumor suppressors was already confirmed for many tumors including multiple myeloma, osteosarcoma, hepatocellular carcinoma, ovarian, and breast carcinoma, which goes in line with our hypothesis (133, 134, 136, 139, 190, 191). For example, EZH2 was shown to represses the *ARHI* tumor suppressor gene in ovarian cancer, or *TP53* and *NOTCH1* in hepatocellular carcinoma (133, 134).

As an example of the identified HIF2α/EZH2 downstream target genes, we found both WT and QMY HIF2a to downregulate *MX2* and *OAS1* in ccRCC cells. *MX2* was published to be functionally involved in the regulation of melanoma proliferation, with low *MX2* mRNA levels in primary melanoma tumors associated with worse patient survival (192). In another study *OAS1* expression was inversely correlated with the progression of breast and prostate cancers (193). Particularly, by employing immunostainings of tumor samples from patients with infiltrative ductal carcinoma of the breast and prostate adenocarcinomas the authors observed low OAS1 protein in high-grade tumors (193). In addition, it was shown that cells of the deadliest form of breast cancer – the so-called triple negative breast cancer, have significantly repressed *OAS1*, *OAS2*, and *OAS3* genes (194), while *OAS2* expression was in addition reported to be a negative prognostic marker in metastatic colorectal cancer (195).

To further corroborate the link between EZH2 activity and HIF2α-mediated invasion of RCC cells, we employed the S-adenosyl-L-[methyl-^{3}H]methionine (SAM) competitive EZH2 inhibitor GSK343. It competes with endogenous SAM and was published to significantly reduce H3K27me3 levels (196). We observed that GSK343 could equally decrease invasion in RCC cells expressing the WT HIF2α and the QMY mutant, but not in the control line.

Interestingly, targeting of EZH2 with a siRNA resulted in much weaker effects on invasion. Much stronger effects of the inhibitor on invasion rather than siRNA-

mediated gene silencing of EZH2 might be explained by the catalytic-independent functions of EZH2 in RCC cells (130, 197). Indeed, tumor type- and context-dependent functions of EZH2 must be considered before planning to target the protein. For example, in acute myeloid leukemia EZH2 primarily functions as an oncogene, targeting of which may be beneficial for the patient. On the contrary, EZH2 acts as a tumor suppressor during AML induction, and thus should not be interfered with (198). Similarly, in AR positive prostate cancer EZH2 was shown to exert both tumor suppressor and oncogenic functions, yet EZH2 inhibitors were shown to synergize with AR antagonists to suppress prostate cancer progression *in vitro* and *in vivo* (130). Thus, it would be important to clarify which pathways and processes become affected after inhibition of the catalytic activity of EZH2 or its complete knockdown in ccRCC during metastasis.

For instance, to further investigate if enzymatic activity of EZH2, but not its alternative functions, is required for tumor cell invasion, we could generate an EZH2 mutant in the catalytic SET domain of the protein. Overexpression of this mutant in ccRCC or CRC cells bearing the WT and QMY HIF2a would allow to clearly dissect the ARNT-independent role of HIF2a and trimethylation-dependent functions of EZH2 in hypoxic tumors. In addition, since H3K27 is not the only substrate of EZH2, other non-histone substrates of EZH2 should be investigated as well.

Hypothesis about the HIF2α/EZH2 regulatory axis driving tumor cell invasion could be further strengthened by comparing affinity of ARNT and EZH2 to HIF2α. This could be done in a clinically relevant manner; in an experiment where HIF2α was first pharmacologically dissociated from ARNT and then ARNT and EZH2 binding to the released HIF2α analyzed by a Co-IP or in a PLA assay. Without such data, we cannot exclude the possibility that even the highly unstable pool of the HIF2α protein at normoxic conditions is sufficient to interact with EZH2 and work

independently of ARNT. For example, it was recently shown that basal HIF1α levels are maintained by a pVHL-antagonizing deubiquitinase Usp8 in normoxia, which are even sufficient to exert some transcription activity (87).

Nonetheless, based on the obtained results we may speculate that HIF2α sensitizes the tumor cells to EZH2 inhibition. Hence, it would be important to test this hypothesis by analyzing the correlation between the response to EZH2 inhibitors and HIF2α protein levels in RCC and CRC patients.

In previous experiments we saw decreased invasion upon pVHL reconstitution, or in WT and QMY HIF2α-overexpressing cells upon EZH2 inhibition. However, in all these experiments invasion could be only partially reduced (e.g. by 60 % compared to the control line). As mentioned above, HIF2α can interact with many other proteins raising the possibility that HIF2α regulates invasion of tumor cells independently of transcription. To explore this hypothesis, we performed mass spectrometry to identify all possible HIF2α interacting partners.

3.5. Mass spectrometry reveals HIF2α interacting partners that may contribute to tumor cell invasion

To explore the HIF2α interactome we employed HCT116 cells since a much more efficient enrichment for WT and QMY HIF2α proteins was achieved after immunoprecipitation in these cells compared to 786O ccRCC cells. This can be partially explained by the different protein tags used to label the HIF2α proteins in CRC and ccRCC cells, or simply by much greater expression of the tagged proteins in HCT116 cells after DFO treatment compared to the non-stimulated expression of the proteins in 786O cells. Nonetheless, since the primary focus of this project were kidney tumors, top HIF2α interacting partners found in CRC were further validated also in ccRCC cells.

Overall, mass spectrometry identified around 1500 interacting partners of HIF2α after normalization to the control cells, with many identified proteins overlapping between wild type, QMY and bHLH HIF2α mutants. A significant part of the shared proteins when characterized functionally proved to be involved in translation, which is in line with the published data by the group of S. Lee. In particular, they could show that HIF2α in cooperation with eIF4E regulates protein translation by directly binding to hypoxia response elements on mRNA (86, 88, 96). The eIF4/HIF2α complex was shown to activate G-proteins and thus impact the transmission of extracellular signals coming from receptor tyrosine kinases. Nonetheless, surprisingly no connections to cell invasion or metastasis was made in the mentioned studies.

Identification of the interacting partners that are involved in translation nicely validated our experimental setup, thus we focused next on those interaction partners that are involved in cell adhesion and remodeling of the extracellular matrix. Additionally, we also identified the common interacting partners of QMY and bHLH HIF2α (a group of 212 proteins). This group of proteins was of special interest for us since it represents HIF2α interactome upon its dissociation from ARNT and DNA. Based on gene ontology analysis, cell adhesion and junction proteins, and cadherins were among the most enriched proteins in this group. Some examples of the top interactors shared by the WT, QMY, and bHLH HIF2α were IQGAP3, clathrin, and δ-catenin (CTNND1) (165, 199-207).

In previous reports increased *IQGAP3* expression was associated with an EMT phenotype, poor response to radiation therapy, decreased survival and worse prognosis (207). Additionally, *IQGAP3* expression has been suggested as an novel diagnostic marker and therapeutic target for colorectal (207), breast (208), ovarian (206), liver (205) and pancreatic tumors (209-211). Based on the mass spectrometry results, we might speculate that HIF2α functionally interacts with

IQGAP3 in CRC as well as ccRCC cells, yet a more detailed analysis how this interaction emerges after pharmacological targeting of HIF2 should be undertaken.

Other top HIF2α interactors detected by mass spectrometry in HCT116 cells were clathrin and several adaptor protein 2 isoforms (AP2A1, AP2A2, AP2B2, and AP2M1), all of which are known regulators of clathrin-mediated endocytosis and play a significant role in cell migration (212, 213). Moreover, we could identify several integrins, such as RAB11 (interacting with all HIF2α protein versions) and RAB35 (interacting with QMY and bHLH HIF2α). Combined, these findings suggest that HIF2α might be involved in clathrin-dependent turnover of integrins. Though the direct HIFα (either HIF1α or HIF2α) interaction with Ras-related RAB protein family members has not been reported yet, it has been shown that hypoxia promotes invasion of carcinoma cells *in vitro* by mobilizing Rab11-dependent recycling of integrin α6β4 (214). Similarly, breast cancer tumors were shown to produce high numbers of extracellular vesicles that are the results of HIF-driven upregulation of RAB22 (215). Other evidence shows that increased Rab11b in the brain microenvironment promotes the recycling of cargo proteins required for breast cancer brain metastasis formation (216). Overall, our data suggest that independently of its ARNT and DNA binding HIF2α might be involved in endocytosis of membrane proteins, signal transfer from the extracellular matrix into the cells, and direct regulation of motility through association with integrins.

Another significant finding was that HIF2α can directly interact with p120. Interestingly, this interaction has not been reported so far. The major function of p120 is the maintenance of the epithelial phenotype of cells by stabilization of adherence junctions via binding to E-cadherin. Destabilization of the p120/E-cadherin complex was previously reported to contribute to tumor development and progression (165, 166). Therefore, we hypothesized that upon the inhibitor-mediated dissociation of the HIF2α/ARNT heterodimer HIF2α might interact with

p120 and lead to the destabilization of p120/E-cadherin complexes and enhanced RCC tumor cell invasion. In fact, a similar mechanism was already shown where p120 dissociated from E-cadherin upon MORG2 binding that resulted in enhanced invasion of breast cancer cells (200, 217). Alternatively, HIF2α could be regulating p120 degradation, similar to a previous publication where Smurf1 was shown to mediate p120 degradation after TGFβ stimulation (218). Lastly, HIF2α could be involved in p120 translocation to the nucleus as the transcription factor Glis2 which was shown to increase p120 nuclear localization and result in suppression of neural differentiation (219). Importantly, by sequestering p120 from E-cadherin HIF2α might also interfere with canonical and non-canonical Wnt signaling (202). A link to Wnt signaling we could already see from the identified cadherin and Wnt signature genes in RNA sequencing. This particular link could be further validated by comparing the Wnt signature genes form our RNA-Seq with the published β-catenin ChIP or RNA sequencing datasets (220, 221). Such analysis would also help to identify possible p120/HIF2α downstream target genes that regulate tumor cell invasion and metastasis, however additional RNA-Seq and ChIP-Seq experiments would be required in ccRCC and CRC cells upon p120 knockdown, since such datasets are currently unavailable.

In addition to binding p120, we could show HIF2α to reduce the overall protein levels and promote the turnover of β-catenin and E-cadherin, the other two significant interacting partners of HIF2α identified by mass spectrometry. In fact, we could identify more catenin family members as well as cadherins as significant binding partners with QMY and bHLH HIF2α, suggesting that HIF2α which is released from ARNT and DNA actively cooperates with the cadherin-catenin protein family members to destabilize E-cadherin/β-catenin complexes. This hypothesis we could indeed validate by a protein turnover cycloheximide decay assay in HCT116 cells.

Validation of the identified top interactors that were able to bind HIF2α in RCC cells confirmed p120-, β-catenin-, and IQGAP3-HIF2α complex formation, but no interaction to clathrin could be detected in these cells. Moreover, when we analyzed stability of β-catenin in 786O cells overexpressing WT and QMY HIF2α in a cycloheximide decay assay we observed that in QMY HIF2α-overexpressing cells β-catenin turnover was much stronger than in WT HIF2α-overexpressing or control RCC cells. Similarly, we could also see enhanced β-catenin degradation after treatment with the PT2385 inhibitor. Although we cannot completely exclude any transcriptional regulation of β-catenin by the HIF2α versions, we hypothesize that HIF2α primarily enhances β-catenin turnover which was published to destabilize cell-to-cell contacts and increase tumor cell invasion (222, 223).
In conclusion, by analyzing the HIF2α interactome we could show that HIF2α associates with multiple proteins that regulate adherens junctions, cell-to-cell contacts, and adhesion to extracellular matrix components, and thus through these non-transcriptional programs contributes to tumor cell invasion, migration, and metastasis.

3.6. Synopsis and prospects

An overall summary of our results is presented in Figure 1. Based on the obtained data, we believe that HIF2α utilizes transcriptional, as well as non-transcriptional pathways to regulate cell invasion. Particularly, we show that HIF2α enhances trimethylation of histones H3K27 by regulating EZH2 activity, which in turn leads to repression of downstream genes, as *OAS1* or *MX2*, suppression of which was shown in previous reports to correlate with increased metastasis. In parallel, HIF2α interacts with p120 and destabilizes E-cadherin and β-catenin complexes, which also significantly contributes to tumor cell invasion and metastasis.

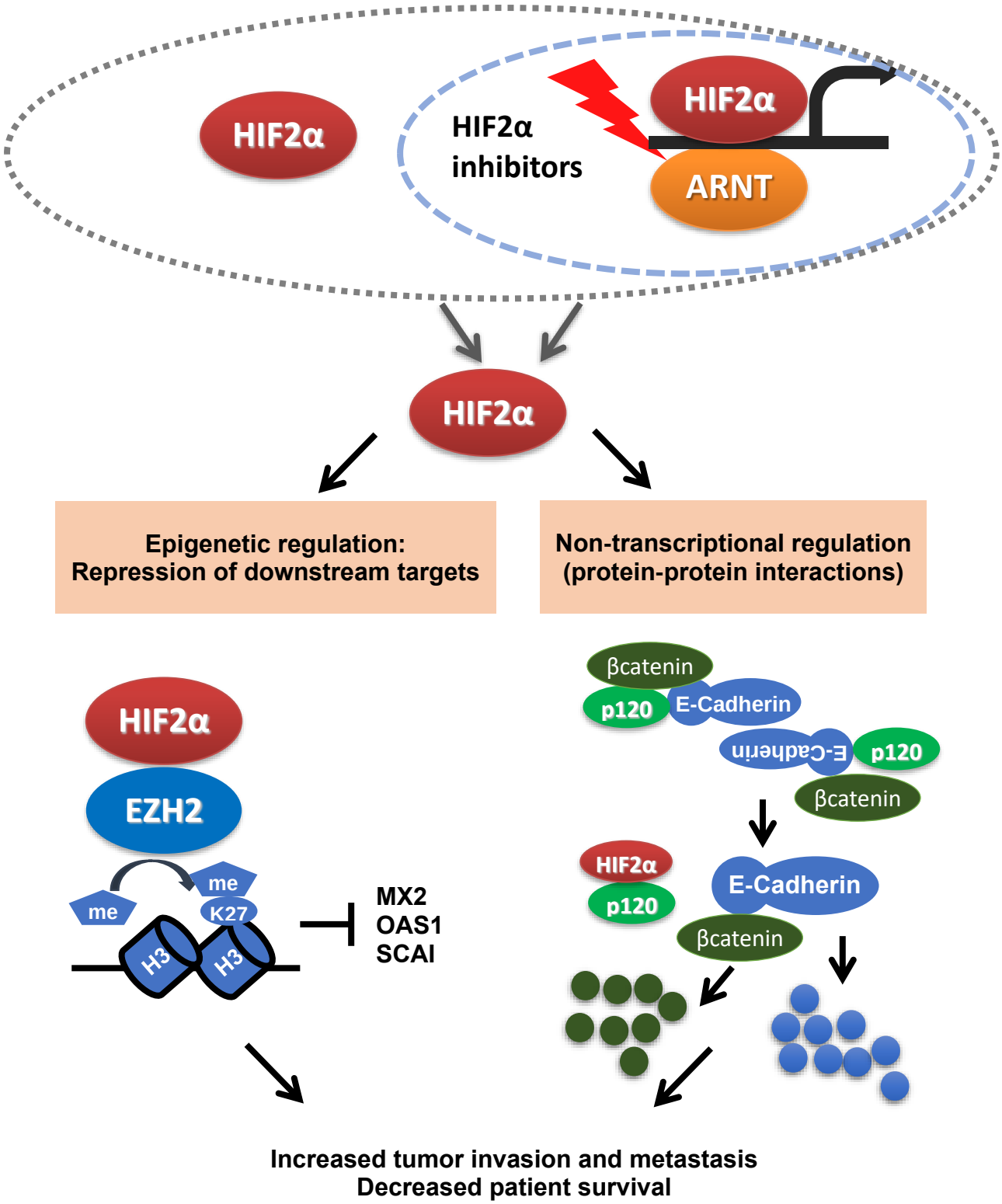

Figure 1. HIF2α employs divergent mechanisms to drive tumor cell invasion and metastasis. Pharmacological dissociation of HIF2α from ARNT leads to the cooperation of HIF2α with EZH2 and multiple other partners that can promote invasion and metastasis in a transcriptional and non-transcriptional manner.

Despite the uncovered HIF2α-mediated mechanisms of tumor invasion and metastasis, several important questions remain unaddressed by the present study. Particularly, further *in vitro* and *in vivo* validation of the identified HIF2α/EZH2 target genes would be required to develop better approaches to inhibit invasion of RCC and CRC tumors. A small gRNA library in combination with a matrigel invasion screen could be successfully employed to address this question. Best candidates can be then evaluated individually by pharmacological targeting or with RNA interference.

Considering the wide interactome data from mass spectrometry, it is difficult to point which of the mechanisms – transcriptional or non-transcriptional – is more important for controlling tumor invasion. Therefore, it is possible that simultaneous targeting of the key transcription-controlled and non-transcriptional regulatory mechanisms of tumor cell invasion mediated by HIF2α would result in a profound anti-metastatic effect not only in CRC and RCC patients, but also in other tumors with elevated HIF2α protein levels.

Considering the vide variety of clinically tested EZH2 inhibitors, it would be especially important to identify the exact HIF2α-mediated canonical and non-canonical functions of EZH2 and exploit these for development of new therapeutic interventions.

Our data hinted at a possible EZH2 co-activator function in RCC cells that is affected by HIF2α, thus it would be also interesting from a fundamental perspective to investigate such a regulatory axis. Moreover, since we also saw HIF2α association with EZH2 in the cytoplasm, such a complex might also exert some functions apart of its chromosome-associated transcriptional regulation. EZH2 and HIF2α were individually shown to facilitate ciliogenesis and integrin turnover, and hence lead to enhanced motility of tumor cells (147, 148, 197).

Pharmacological inhibition of the HIF2α/ARNT heterodimer-dependent transcriptional activity with the newly developed inhibitors was shown to reduce primary RCC growth in preclinical trials. Yet, it might be possible that the absence of positive clinical results so far can be explained not only by acquisition of HIF2α mutations in response to these small molecule inhibitors, but also with the mechanisms leading to increased invasion and metastasis which we identified in this project. However, based on a better understanding of the HIF2α-mediated mechanisms that drive tumor cell invasion we may speculate about the existence of several synthetic lethality pairs between pVHL as the major HIF2α regulator, and other pathways, such as EZH2. In fact, similar synthetic lethality pairs between EZH1 and CDK4/6 or selenocysteine biosynthesis pathway were already proposed by several groups showing very promising therapeutic outcomes in terms of primary tumor growth inhibition (104-106). Interestingly, beyond the proposed EZH1/pVHL synthetic lethality pair, HIF2α and EZH2 combination was dismissed by the authors on the basis of their sgRNA screen, however they never analyzed the potential implications of such a synthetic lethality pair for invasion and metastasis. Yet, before the concept of a HIF2α/EZH2 synthetic lethality pair could be explored in the clinical setting it would be necessary to identify the appropriate criteria to select the patients for testing this new therapeutic approach. Importantly, assessing the pVHL status alone would significantly limit the approach only to tumors which are known to harbor various inactivating mutations in the gene, as is the case in ccRCC. Based on the obtained data we suggest that HIF2α protein levels or expression of direct downstream target genes could serve as more informative markers and might lead to a wider inclusion of patients with different tumor types that could potentially benefit from this new therapeutic approach (for example, this would most certainly result in the inclusion of patients with paragangliomas and pheochromocytomas, which frequently harbor mutations in the ODD domain of

HIF2α resulting in its increased stability and increased oncogenic potential (45-47, 49).

Since our data indicate that HIF2α controls invasion in an ARNT-independent fashion, inhibitors which block HIF2α protein synthesis or promote its degradation might have a better chance of reducing metastasis. For example, such drugs as the small molecule compounds 46 and 76 that were shown to induce the degradation of HIF2α mRNA (115) might be successfully administered as monotherapy or in combination with other drugs to prevent metastasis. Another potential approach could be to employ peggylated siRNAs against HIF2α as reported by Wong and colleagues (100). This is a novel approach in which modified siRNAs efficiently penetrate into cells and survive the microenvironment due to recoupled PEGs and integrins. Since we see destabilization of β-catenin and E-cadherin by HIF2α, other possible therapeutic combinations with drugs that restore cell-to-cell and cell-ECM connections, such as eribulin or dasatinib (224), could possibly synergize with approaches targeting HIF2α.

4. Materials

4.1. Chemicals

Chemicals were purchased from Sigma-Aldrich, Roth, Invitrogen, Merck, Thermo Scientific, New England Biolabs (NEB), BioLegend, or Biozym unless otherwise specified. All reagents were prepared with distilled deionized water (ddH_2O) unless otherwise indicated.

4.2. Buffers and solutions

4.2.1. Transfection and infection of mammalian cells

Chloroquine	10 mg/ml in H_2O, stored at 4 °C
DMEM (without pen/strep and FBS)	Sigma
1 x HBS	25 mM HEPES, 140 mM NaCl, 0.75 mM Na_2HPO_4, pH 7.05 (filtered), stored at -20 °C
$CaCl_2$	2.5 M $CaCl_2$, filtered, stored at -20 °C
Opti-MEM I reduced serum medium	Life Technologies
PBS, 1 x	8 g/L NaCl, 0.2 g/L KCl, 1.44 g/L Na_2HPO_4, 0.24 g/L KH_2PO_4, pH 7.4, autoclaved
PEI (polyethylenimine) branched, Sigma, #408727	1.2 µg/µl PEI in H_2O, filtered, stored at -20 °C
Polybrene (hexadimethrine bromide)	4 mg/ml in H_2O, stored 4 °C
Chloroquine	10 mg/ml in H_2O
siRNA buffer, 5 x	300 mM KCl, 30 mM HEPES, pH 7.5, 1.0 mM $MgCl_2$, filter sterilized, stored at -20 °C

4.2.2. RNA preparation and electrophoresis

TRI RNA isolation reagent	Sigma, 93289
1-Bromo-3-chloropropane	Sigma, B9673
Isopropanol	Sigma
Ethanol	Sigma
2 x RNA loading dye	95 % formamide, 0.025 % SDS, 0.025 % bromophenol blue, 0.025 % xylene cyanol FF, 0.025 % ethidium bromide, 0.5 mM EDTA, stored at -20 °C
1 x TAE buffer	40 mM Tris-acetate, pH 8.3, 1 mM EDTA, stored at 4 °C
Agarose, 1.0-1.5 % in TE buffer	SeaKem
Ethidium bromide, 0.06 %	Roth

4.2.3. DNA isolation and electrophoresis

Genomic DNA extraction buffer (proteinase K digestion buffer)	10 mM Tris, pH 8.0, 2 mM EDTA, 400 mM NaCl, 0.5 % SDS added freshly, 100 µg/ml proteinase K, freshly added
Phenol:chloroform:isoamyl alcohol (25:24:1) saturated with 10 mM Tris, pH 8.0, 1 mM EDTA	Sigma
Glyco-blue DNA co-precipitation reagent (15 mg/ml)	Invitrogen, AM9516
Proteinase K	10 mg/ml protease K in H_2O
RNAse A	10 mg/ml (Thermo Scientific)
3 M Na-acetate, pH 5.3	
TE buffer	10 mM Tris-HCl, pH 8.0, 1 mM EDTA
Isopropanol, ethanol, TAE buffer as described above.	

4.2.4. cDNA synthesis and q-PCR

MLV reverse transcriptase buffer	Promega
MLV reverse transcriptase	Promega
Ribo lock RNAse inhibitor	Thermo Scientific
Random hexamers or octamers	Sigma
SYBR-green qPCR master mix	Sigma
Phusion high fidelity DNA polymerase	NEB
dNTP, 10 mM (dATP, dTTP, dGTP, CTP)	Sigma
Red-Taq polymerase	Sigma

4.2.5. Cell lysis buffers

Buffer	**Composition**
Protein A beads	Pierce protein A agarose (Thermo Scientific)
Protein G beads	Protein G sepharose (Sigma)
Laemmli lysis buffer	10 mM Tris-HCl, pH 7.5, 2 % SDS, 2 mM EGTA, 20 mM NaF, stored at -20 °C
RIPA lysis buffer (weak)	50 mM Tris, pH 8.0, 150 mM NaCl, 0.25 % sodium deoxycholate, 0.5 % NP-40 (Igepal), freshly added protease and phosphatase inhibitors at 1:1000
RIPA lysis buffer (strong)	50 mM Tris, pH 8.0, 150 mM NaCl, 0.1 % SDS, 1 % Triton X-100, freshly added protease and phosphatase inhibitors at 1:1000

Buffer	Composition
TNT lysis buffer	50 mM Tris, pH 8.0, 150-500 mM NaCl, 1 % Triton X-100, protease and phosphatase inhibitors at 1:1000
PBS lysis buffer	1 x PBS, 0.5-1 % Triton X-100, freshly added protease and phosphatase inhibitors at 1:1000
Lysis buffer for mass spectrometry	50 mM Tris HCl, pH 6.8, 2 % SDS, 10 % glycerol, (without DTT or dyes, stored at RT)
Subcellular fractionation	
Cytosolic fraction	5 mM PIPES, pH 8.0, 0.85 mM KCl, 0.1 % Triton X-100, freshly added protease and phosphatase inhibitors at 1:1000
Nuclear fraction	Laemmli lysis buffer
Soluble fraction	TNT 150-300 lysis buffer, freshly added protease and phosphatase inhibitors at 1:1000
Pierce BCA protein assay kit	Thermo Scientific, #23225

4.2.6. SDS-PAGE and Immunoblotting

Reagents/buffers	Composition
Ammonium persulfate (10 %, APS)	0.5 g APS were dissolved in 5 ml H_2O, stored at -20 °C
Antibody dilution buffer	2.5-5 % (w/v) BSA in TBST, 0.1 % Na-azide

Reagents/buffers	Composition
Acrylamide-, bisacrylamide, 37.5:1	Roth
Blocking solution for PVDF membrane	5 % (w/v) non-fat dry milk in TBST
Bis-Tris, 3.5 x	1.25 M Bis-Tris, pH 6.8
Bis-Tris separation gel	8-12 % (v/v) acrylamide, 0.35 M Bis-Tris, 0.1 % (v/v) APS, 0.075 % (v/v) TEMED
Bis-Tris stacking gel	4 % (v/v) acrylamide, 0.2 M Bis-Tris, 0.125 % (v/v) APS, 0.0375 % (v/v) TEMED
Developing solutions A and B	Immobilon Western HRP substrate (Millipore)
4 x Laemmli sample buffer (4 x LSB)	62.5 mM Tris-HCl, pH 6.8, 10 % glycerol, 1 % SDS, 0.005 % bromophenol blue, stored at RT
MOPS running buffer (20 x)	1 M MOPS, 1 M Tris, 20 mM EDTA, 2 % SDS
MOPS running buffer	5 % MOPS running buffer (20 x), 1 mM sodium bisulfite
NuPAGE sample buffer (20 x)	250 mM Tris, pH 8.0, 4 % SDS, 25 % (v/v) glycerol, 0.01 % bromophenol blue, 0.1 M DTT
Protein marker	PageRuler prestained protein ladder (Thermo Scientific)
PVDF transfer membrane	Amersham hybond P Western blotting membranes, PVDF, 0.45 µm (Sigma)
4 x sample buffer, working solution prepared freshly	900 µl 4 x LSB, 100 µl of 2-mercaptoethanol, alternatively: DTT up to 50 mM
Stripping buffer	60 mM Tris, pH 6.8, 0.7 % 2-mercaptoethanol, 2 % SDS

Reagents/buffers	Composition
Transfer buffer (10 x)	144 g/L glycine, 30.2 g/L Tris base
Transfer buffer (ready to use)	10 % transfer buffer (10 x), 20 % methanol
TBS (20 x)	500 mM Tris base, 2.8 M NaCl, pH 7.4
TBS-T	1 x TBS, 0.2 % Tween-20

4.2.7. Chromatin immunoprecipitation

ChIP dilution buffer	50 mM Tris, pH 8.0, 167 mM NaCl, 0.11 % Na-deoxycholate, 1.1 % Triton X-100, freshly added protease and phosphatase inhibitors at 1:1000
ChIP wash buffer I	Nuclei lysis buffer diluted with 10 x with ChIP dilution buffer
Cytoplasmic lysis buffer	5 mM PIPES, pH 8.0, 0.85 mM KCl, 1 % Triton X-100, freshly added protease and phosphatase inhibitors at 1:1000
Direct elution buffer	10 mM Tris, pH 8.0, 300 mM NaCl, 5 mM EDTA, 1 % SDS
Formaldehyde	37 % formaldehyde (Sigma)
Glycine solution	2.5 M glycine in water, pH 2.0
Magnetic beads (HighPrep PCR beads)	HighPrep PCR reagents (Biozym)
Micrococcal nuclease	NEB, M0247S
Micrococcal nuclease buffer	1 x MNase buffer (NEB, M0247S)
Nuclei lysis buffer	50 mM Tris, pH 8.0, 10 mM EDTA,

	1 % SDS, freshly added protease and phosphatase inhibitors at 1:1000
PicoGreen reagent	Quant-iT PicoGreen dsDNA reagent (Thermo Scientific)
Phosphatase inhibitors (Sigma, 0044)	1:1000
Protease inhibitors (Sigma, P8340)	1:1000
Protein A magnetic beads	NEB, S1425S
Protein G magnetic beads	NEB, S1430S
Proteinase K and RNaese A	As described in 4.2.3.
ChIP wash buffer II (RIPA high salt buffer II)	50 mM Tris, pH 8.0 500 mM NaCl, 1 mM EDTA, 0.1 % SDS, 0.1 % Na-deoxycholate, 1 % Triton X-100
ChIP wash buffer III (RIPA LiCl buffer III)	50 mM Tris, pH 8.0, 250 mM $LiCl_2$, 1 mM EDTA, 0.7 % Na-deoxycholate, 1 % Triton X-100

4.3. Nucleic acids

4.3.1. Primers used for q-PCR

Name	Sequence (5' to 3'), forward primer	Sequence (5' to 3'), reverse primer
3prime UTR-hHI2a	GGCTTTTTGCCATCTGTGAT	GCACTTGAAGGGCTAGCAAC
3prime UTR-hHI2a	GCGTGGCTTTTCCTAAACTG	GGACAAGTCTGCAGTGTCCA
5prime UTR-hHI2a	CAGCATTCGAGCCACTTTTT	AAAGGTGACTGGGAGGAACC
5prime UTR-hHI2a	TACAATCCTCGGCAGTGTCC	GAGGACGGAGAGAAGGGAAC
hANGPT1 tv 1-3	ACAACCTTGTCAATCTTTGCACT	TGCAAAACACCTTTTTGGGTTCT
hANGPT2	ACCCCACTGTTGCTAAAGAAGA	CCATCCTCACGTCGCTGAATA
hAPOL1	GTGGGATCCACACAGCTCAG	GGCCTCCTCCAAGGAATCTT

Name	Sequence (5’ to 3’), forward primer	Sequence (5’ to 3’), reverse primer
hBMI1 ex-ex	TCCCAGCCCCGCAGAATAAA	AAAAATCCCGGAAAGAGCAGCC
hBMI1	GAGATCGGGGCGAGACAATG	TTTTATTCTGCGGGGCTGGG
hBTRC	CTCAAGTTTATGTGCTCTATGCCC	ATCTTCCTAGGGGGTTCGCC
hCDH1 (N-Cad)	TGGGCCAGGAAATCACATCC	TGCAACGTCGTTACGAGTCA
hCDH1 (E-Cad) tvX2	TGGTAACGGATCCAGCAGTGAA	GAATCGGGTGTCGAGGGAAA
hCITED2	CCTAATGGGCGAGCACATACA	GGGGTAGGGGTGATGGTTGA
hCSTB	ATTCAAGAGCCAGGTGGTCG	CACTCGCAGGTGTACGAAGT
hCyclinD1 (CNND1)	TGGAGCCCGTGAAAAAGAGC	TCTCCTTCATCTTAGAGGCCAC
hCyclophillin (CYP1)	TGCCATCGCCAAGGAGTAG	TGCACAGACGGTCACTCAAA
hEHBP1L1	CCCCAGCCAGATCCCTCTC	AGCATTAGAAGGGCTGGCAA
hEZH2	GCTTCCTACATCGTAAGTGCAA	GCTCCCTCCAAATGCTGGTA
hGLUT1	TCTGGCATCAACGCTGTCTTC	CGATACCGGAGCCAATGGT
hGLUT1	GCCAGAAGGAGTCAGGTTCAA	TCCTCGGAAAGGAGTTAGATCC
hHIF2α	GCGACAATGACAGCTGACAA	CAGCATCCCGGGACTTCT
hHPRT1	TATGGCGACCCGCAGCCC	GCAAGACGTTCAGTCCTGTCCAT
hJAG1	AATGGCTACCGGTGTGTCTG	CCCATGGTGATGCAAGGTCT
hKRT80	TCCAAGGTGACTGTGAACCC	CTTGCACCTTGCCAATTAGGG
hLAT	CTACGAGAACGAGGAACCAGC	CTGTCAGGAAGCACCACCAG
hLOX	GCGAAGGGTGAGGAGTAAGG	AGACCTAAACGTCAGCAGGC
hLOXL2	CCAGTGTGGTCTGCAGAGAG	GATGGGTCCGATCCCTTGC
hMMP13	CATGAGTTCGGCCACTCCTT	CCTCGGAGACTGGTAATGGC
hMMP2	GAGTGCATGAACCAACCAGC	AAACTTGCAGGGCTGTCCTT
hMMP9	TCTATGGTCCTCGCCCTGAA	TTGTATCCGGCAAACTGGCT
hPCSK5	CCTGCCCCATGACAAGGATT	ACTTCCTTGGCATCTCTGGC
hPDK1	GAACCCAAAGACATGACGACG	ATGTCCCAAGTGTGTCTAGGCA
hPGK1	TTAAAGGGAAGCGGGTCGTTA	TCCATTGTCCAAGCAGAATTTGA
hPIP4K2A	AGCACTTCGTAGCGCAGAAA	GCTCAGTTCATTGATCGAGTGG
hPOU51 (Oct4) tv1	TATTTGGGAAGGTATTCAGCCAAAC	GCGATGTGGCTGATCTGCTG
hROR1	AGTGCTGAATTAGTGCCTACCT	TCGAGGGTCAGGTAAGAATCTTTG
hRPL30	ATCTTAGCGGCTGCTGTTGG	GACTCCAGCGACTTTTTCGTC
hRPS14	GGCAGACCGAGATGAATCCTCA	CAGGTCCAGGGGTCTTGGTCC
hSEMA5A	CTAGCCAGGTGCTGAAGAGG	TGTGTGGAAAGTGCCAAGGA
hSerpine1 (PAI-1)	ACCGCAACGTGGTTTTCTCA	TTGAATCCCATAGCTGCTTGAAT
hSLUG	AGACCCCCATGCCATTGAAG	GGCCAGCCCAGAAAAAGTTG
hSNAIL	AAGATGCACATCCGAAGCCA	CAAAAACCCACGCAGACAGG
hSUZ12	AGCCGAAAATGGAGCACGTC	ATCTGTGTTGGCTTCTCAAAGG
hSYNE1	GGTGGTCCCGGTATAAAGGC	CCCAGCCGCCCTCCT
hTGFA	CGGTAGCCGCCTTCCTATTTC	TGGACTCAGACACCAACTGC
hTGFB	ACCTGCCACAGATCCCCTAT	GAGCAACACGGGTTCAGGTA

Name	Sequence (5’ to 3’), forward primer	Sequence (5’ to 3’), reverse primer
hTMEM158	CGCTTCCAGTTCCGAAAAGC	GCAGGGGGATGCAATAGAGG
hTNRS21	CCAATGGGTACACAGCCGAC	TTTCCAGCTGGGTGGTGTCTT
hTNS3	TCCAAAGTGTGTGGAGTTTGC	AATACTTGCAGGCTCGGCAT
hUBA6	TGCAGTCAAAGAGAAGTATGGAA	TGTCTGGAGCAAATGACACAGT
hVEGFA	AGCCTTGCCTTGCTGCTCTA	GTGCTGGCCTTGGTGAGG
hVIM	CTCTGGCACGTCTTGACCTT	TTGCGCTCCTGAAAAACTGC
hZEB2	CTCTGTAGATGGTCCAGTGAAGA	TGCAGTTTGGGCACTCGTAA

4.3.2. Oligos used for cloning: shRNA, guide RNA, mutagenic PCR, and overexpression constructs

shRNA and siRNA

Name	Sequence (5’ to 3’), forward primer
Human ARNT. 1812	TGCTGTTGACAGTGAGCGACAGGATAGAGATCCAAGATTTTAGTGAAGCCACAGATGTAAAA TCTTGGATCTCTATCCTGGTGCCTACTGCCTCGGA
Human HIF2α	TGCTGTTGACAGTGAGCGCCCAGACTGAATCCCTGTTCAATAGTGAAGCCACAGATGTATTG AACAGGGATTCAGTCTGGTTGCCTACTGCCTCGGA
Human HIF2α, 5′-UTR	TGCTGTTGACAGTGAGCGGGCGTCTGAACGTCTCAAAGGATAGTGAAGCCACAGATGTATCC TTTGAGACGTTCAGACGCCTGCCTACTGCCTCGGA
EZH2, siRNA	SMARTpool: ON-TARGETplus EZH2 siRNA, 5 nmol, Horizon Discovery (Dharmacon)

Mutagenic PCR and cloning oligos

Name	Sequence (5’ to 3’), forward primer	Sequence (5’ to 3’), reverse primer
human HIF2α, Q322E	GAGGGGACGGTCATCTACAAC	GGTCTCCAGCCACACGTAGCC
human HIF2α, M338E	GAGTGTGTCAACTACGTCCT	GATGCACTGGGGCTGCAGGT
human HIF2α, Y342T	ACCGTCCTGAGTGAGATTGAG	GTTGACACACATGATGCACTG
M338E, Y342T	GAGTGTGTCAACACCGTCCTGAGTGAG ATTGAG	GATGCACTGGGGCTGCAGGT
wild type human HIF2α, BamHI, EcoRV	ACGTACGGATCCATGACAGCTGACAA GGAGAAGAAA	ACGTACGATATCTCAGGTGGCCTGGT CCAGGGCTCT
bHLH deficient human HIF2α	ACGTACGGATCCGAAGCCGAAGCTGA CCAGCAG	CGTACGATATCTCAGGTGGCCTGGTC CAGGGCTCT

Guide RNA (gRNA)

Name	Sequence (5’ to 3’), forward primer	Sequence (5’ to 3’), reverse primer	Backbone vector
HIF2α KO, gRNA	CACCGATTGCCAGTCGCATGATGG	AAACCCATCATGCGACTGGCAATC	Px459 v2, pLenti-CRISPR v2
miR30 SpeI	ACGTACACTAGTGTTTGTTTGAATGAGGCTTCAGTACTTTACAG	ACGTACACTAGTCCCGCCCGCAAACAACATC	pRRL

Primers used for genotyping and sequencing

Name	Sequence	Purpose
CMV Forward	CGCAAATGGGCGGTAGGCGTG	pcDNA3, TST206
U6 Forward	GAGGGCCTATTTCCCATGATTCC	Px459 v2, pLenti-CRISPR v2
pGIPZ Forward	GCATTAAAGCAGCGTATC	pGIPZ
SFFV 5'-3' (EILERS)	CTTCTGCTTCCCGAGCTCTA	pRRL
SFFV-F Forward	ATTGATTGACTGCCCACCTC	pRRL
MSCV_reverse	CAGCGGGGCTGCTAAAGCGCATGC	pRRL
O_PGK1b reverse	GAACGGACGTGAAGAATGTG	pLKO

4.3.3. Vectors and plasmids

Vector	Description
pcDNA3.1	eukaryotic expression vector with a CMV promoter
pRRL-SFFV-IRES-Hygro	lentiviral expression vector with a SFFV promoter and hygromycin resistance, obtained from the lab of Prof. M. Eilers
pRRL-SFFV-IRES-Puro	lentiviral expression vector with a SFFV promoter and puromycin resistance, obtained from the lab of Prof. M. Eilers
pLKO.1	lentiviral expression vector with a U6 promoter and puromycin resistance, obtained from the lab of Prof. M. Eilers
pGIPZ	lentiviral expression vector with a SV40 promoter, puromycin resistance, and eGFP, obtained from the lab of Prof. M. Eilers

pGIPZ delta EcoR1	lentiviral expression vector with a SV40 promoter, puromycin resistance, eGFP, lacking EcorI restriction site for cloning purposes, obtained from the lab of Prof. M. Eilers
TST206	transposon vector with a CMV promoter, puromycin resistance, provided by Dr. T. Stühmer
pCMV(CAT)T7-SB100	transposase vector (pCMV(CAT)T7-SB100, Addgene, #34879) encoding for the SB100 excisase/integrase
psPAX.2	lentiviral production vector encoding the packaging proteins
pVSVG-Env	lentiviral production vector encoding the vesicular stomatitis virus envelope protein

4.3.4. Cloned constructs

Vector	**Type of vector**	**CDS**
pRRL-Hygro(2337)-mCherry	lentiviral expression	cherry RFP
pRRL-Puro(2337)-HA-HIF2α WT	lentiviral expression	human wild type HIF2α tagged with 2 x HA at the C-terminus
pRRL-Puro(2337)-HA-HIF2α QMY mutant	lentiviral expression	human HIF2α containing a mutation in the ARNT-binding site tagged with 2 x HA at the C-terminus
pRRL-Puro(2337)-HA-HIF2α bHLH mutant	lentiviral expression	human HIF2α without the bHLH domain, tagged with 2 x HA at the C-terminus
pRRL-Hygro(2338)-mCherry	lentiviral expression	cherry RFP
pRRL-Hygro(2338)-mCherry-shHIF2α	lentiviral expression	human wild type HIF2α tagged with 2 x HA at the C-terminus
pRRL-Hygro(2338)-	lentiviral	human wild type HIF2α tagged with 2 x HA at

Vector	**Type of vector**	**CDS**
shHIF2α-HA-WT	expression	the C-terminus
pRRL-Hygro(2338)-shHIF2α-HA-WT QMY	lentiviral expression	human HIF2α containing a mutation in the ARNT-binding site tagged with 2 x HA at the C-terminus
TST206-pT2SVPuroCMV-HA-HIF2α WT	transposon	human wild type HIF2α tagged with 2 x HA at the C-terminus
TST206-pT2SVPuroCMV-FLAG-HIF2α-WT	transposon	human wild type HIF2α tagged with 3 x FLAG at the C-terminus
TST206-pT2SVPuroCMV-FLAG-HIF2α-QMY	transposon	human HIF2α containing a mutation in the ARNT-binding site tagged with 3 x FLAG at the C-terminus
TST206-pT2SVPuroCMV-FLAG-HIF2α-bHLH	transposon	human HIF2α without the bHLH domain, tagged with 3 x FLAG at the C-terminus
px459-CRISPR Cas9-v2	gRNA/Cas9	sgRNA and CRISPR/Cas9
pGIPZ deltaEcoRI-shHIFα	lentiviral for miR-30 RNAi	shRNA against 5’ UTR of human HIF2α

4.4. Enzymes for cloning

All enzymes and supplemented buffers used for cloning were purchased from Thermo Scientific unless otherwise specified.

4.5. Antibodies

List of primary antibodies

IB = immunoblot, ChIP = chromatin immunoprecipitation, IF = immunofluorescence, IP = immunoprecipitation, PLA = proximity ligation assay, mAb = monoclonal antibodies, pAb = polyclonal antibodies

Antibody	Host Isotype	Application	Supplier, ordering no.
Cyclin D1 E3P5S	Rabbit mAb	WB	Cell Signaling, 55506
E-cadherin (24E10)	Rabbit mAb	WB, IF, PLA	Cell Signaling, 3195 P
E-cadherin (Clone 36)	Mouse mAb	WB	BD Biosciences, 610181
EGFR (D38B1)	Rabbit mAb	WB	Cell Signaling, 4267
Ezh2	Rabbit pAb	WB, IP, ChIP, PLA	Bethyl, A304-197A
Ezh2	Rabbit pAb	ChIP, ChIP-Seq	Diagenode, C15410039-50
Ezh2 (D2C9)	Rabbit mAb	WB, IP	Cell Signaling, 5246
FLAG M2	Mouse mIgG1	WB, IP	Sigma, F3165
FLAG M2 (DYKDDDDK)	Rabbit pAb	WB, IP	Cell Signaling, 2368
Glut1, MBS179154	Rabbit mAb	WB	MyBioSource
H3K27me3	Rabbit pAb	ChIP, ChIP-Seq	Diagenode, C15410069
HA-tag (6E2)	Mouse mAb	WB, IP, IF, PLA	Cell Signaling, 2367
HA-tag (C29F4)	Rabbit mAb	WB, PLA	Cell Signaling, 3724
HIF1β/ARNT (D28F3)	Rabbit mAb	WB, IP	Cell Signaling, 5537P

Antibody	Host Isotype	Application	Supplier, ordering no.
HIF2α	Rabbit pAb	WB, IP, IF, ChIP	Novus, NB100-122
HIF2α	Rabbit pAb	WB, IF	Abcam, ab109616
HIF2α (D9E3)	Rabbit mAb	WB, IF	Cell Signal, 7096S
HIF2α (BL-95-1A2)	Rabbit mAb	WB, IP, ChIP, ChIP-Seq	Bethyl/Biomol, A700-002-T
HIF2α/EPAS1 (ep190b)	Mouse mAb	WB, ChIP, ChIP-Seq	Novus, NB100-132
Histone H3	Rabbit pAb	WB	Abcam, ab1791
SUZ12 (D39F6)	Rabbit mAb	WB, IP	Cell Signaling, 3737
Tri-Methyl-Histone H3 (Lys27) (C36B11)	Rabbit mAb	WB	Cell Signaling, 9733
VHL (von Hippel-Lindau)	Rabbit pAb	WB	Cell Signaling, 68547
Vinculin	Mouse mIgG1	WB	Sigma, SAB4200080
α-Tubulin	Mouse mIgG1	WB	Cell Signaling, 3873P
β-Actin	Mouse mIgG1	WB	Sigma, AC-15/A5441
β-Catenin (L87A12)	Mouse mAb	WB, IF, IP	Cell Signaling, 2698

Secondary antibodies

Antigen	Application	Supplier, ordering no.
anti-Rabbit IgG-HRP	IB	Cell Signaling, 7074
anti-Mouse IgG-HRP	IB	Cell Signaling, 7076
Alexa Fluor 488 anti-Rabbit IgG	IF	Cell Signaling, 4412
Alexa Fluor 488 anti-Mouse IgG	IF	Cell Signaling, 4408
Alexa Fluor 555 anti-Rabbit IgG	IF	Cell Signaling, 4413
Alexa Fluor 555 anti-Mouse IgG	IF	Cell Signaling, 4409

4.6. Bacteria cell culture

4.6.1. Bacteria Strains

DH5α	NEB® 5-alpha competent *E. coli*, high efficiency (C2987H)
	NEB® 5-alpha competent *E. coli*, subcloning efficiency (C2988J)
10-beta	NEB® 10-beta competent *E. coli*, high efficiency (C3019I)
	NEB® 10-beta electrocompetent *E. coli* (C3020K)

4.6.2. Cultivation medium and supplements for bacterial cell culture

Antibiotics	Specified antibiotics were added to LB medium and LB agar plates to the following end concentrations: ampicillin 100 µg/ml kanamycin 30 µg/ml
LB medium	10 g/L tryptone, 5 g/L yeast extract, 10 g/L NaCl, autoclaved
LB agar	LB medium with 15 g/L agar, autoclaved
SOC medium	20 g/L tryptone, 5 g/L yeast extract, 4.8 g/L $MgSO_4$, 3.603 g/L dextrose, 0.5 g/L NaCl, 0.186 g/L KCl, autoclaved
SOC (NEB, B9035)	2 % vegetable peptone, 0.5 % yeast extract, 10 mM NaCl, 2.5 mM KCl, 10 mM $MgCl_2$, 10 mM $MgSO_4$, 20 mM glucose

To prepare LB agar plates, LB agar medium was autoclaved, then cooled to approx. 55 °C, and the desired antibiotic was added to the final concentration as indicated. The final mix was then poured into 10 cm bacterial Petri dishes.

4.7. Mammalian cell culture

4.7.1. Mammalian cell lines

Cell lines	Description
A498	Human kidney carcinoma (CLS Cell Lines Service)
786O	Human renal cell adenocarcinoma (CLS Cell Lines Service)
769P	Human renal cell adenocarcinoma
UMRC2	Human renal cell adenocarcinoma, University of Michigan Renal Carcinoma-2, (UMRC2)
RCC-4	Human renal cell adenocarcinoma
HCT116	Human colon carcinoma cell line (ATCC)
HEK293T	Human embryo kidney cell line (ATCC)
HeLa	Human cervical carcinoma cell line (ATCC)
LentiX	subclone of the transformed human embryonic kidney cell line, HEK293 (TaKaRa)
MCO2	Mouse colon carcinoma cell line, kindly provided by Dr. Daniel Dauch, Department of Internal Medicine VIII, University Clinic Tübingen
Phoenix ECO	Second-generation retrovirus producer lines based on the 293T cell line

4.7.2. Media and antibiotics for mammalian cell culture

Composition of full medium used for culturing all mammalian lines in the project: DMEM with 4.5 g/L glucose, L-glutamine, sodium pyruvate, and sodium bicarbonate (Sigma), 10 % FBS (Sigma), 1 % (v/v) penicillin/streptomycin (Sigma, P4333).

4.7.3. Antibiotics and chemicals used for mammalian cell culture

The following antibiotics with the indicated concentrations were applied to select for transfected or transduced cells:

Antibiotic	Concentration	Cell line	Selection time
Blasticidin (InvivoGen)	5 µg/ml	HeLa	3-5 days
	5 µg/ml	HCT116	3-5 days
Puromycin (InvivoGen)	1 µg/ml	A498	3 days
	1 µg/ml	786O	3 days
	0.5-1 µg/ml	HeLa	2-3 days
	0.5-1 µg/ml	HCT116	3 days
Hygromycin (InvivoGen)	75-100 µg/ml	A498	5-7 days
	100-150 µg/ml	786O	5 days

Following chemicals were used for transfection, transduction, and cell culture-based biochemical protein stability and degradation assays:

Chemical	Stock concentration	Final concentration
Chloroquine (Sigma)	10 mM	10 µM
Polyethylenimine, branched, Sigma, #408727	1.2 mg/ml in H2O	DNA:PEI 1:2-1:5
Polybrene (hexadimethrine bromide, Sigma)	4 mg/ml	4 µg/ml
Cycloheximide (CHX, Sigma)	50 mg/µl in 100 % ethanol	50 µg/ml, 100 µg/ml
MG-132 (Calbiochem)	10 mM in DMSO	10 µM

4.7.4. Chemotherapeutic agents

Compound	Target	Supplier	Catalog number
EPZ005687	EZH2 inhibitor	Biomol	Cay13966-5mg
GSK-343	EZH2 inhibitor	Medchemexpress	HY-13500
Compound 2	HIF2α inhibitor	Axon	2034
CAS-882268-69-1	HIF-2α Translation Inhibitor	Calbiochem	400087
PT-2385	HIF2α inhibitor	Medchemexpress	HY-12867
PT-2399	HIF2α inhibitor	Medchemexpress	HY-108697

4.8. Hematoxylin and eosin staining (H/E)

Chemical	Stock concentration
PFA (paraformaldehyde)	4 % PFA dissolved in 1 x PBS
Mayer's hematoxylin solution	Applichem, #A4840-500
Eosin solution	eosin Y solution, alcohol-based, Sigma-Aldrich, #HT110116
0.5 M PB buffer	115 mM NaH_2PO_4, 385 mM Na_2PO_4, pH 7.4, stored at RT

4.9. Kits

Kit	Company	Reference number
GenElute HP Plasmid Maxiprep Kit	Sigma	NA0310-1KT
GenElute Gel Extraction Kit	Sigma	NA1111
GenElute HP Plasmid Midiprep Kit	Sigma	NA0200-1KT
GenElute HP Plasmid Miniprep Kit	Sigma	PLN70-1KT
MinElute PCR Purification Kit	Qiagen	28006
Monarch DNA Gel Extraction Kit	NEB	T1020S
NEBNext Multiplex Oligos for Illumina (Index Primer Set 1)	NEB	E7600S
NEBNext Multiplex Oligos for Illumina (Index Primer Set 2)	NEB	E7600S
NEBNext Poly(A) mRNA Magnetic Isolation Module	NEB	E7490S
NEBNext Ultra II DNA Library Prep Kit for Illumina	NEB	E7530S
NEBNext Ultra RNA Library Prep Kit for Illumina	NEB	E7530S
RNase-Free DNase Set	Qiagen	79254
Pierce BCA Protein Assay Kit	Thermo Scientific	23225
Experion RNA StdSens Analysis Kit	Bio-Rad	700-7103
Experion DNA 1K Analysis Kit	Bio-Rad	7007107
Quant-iT PicoGreen dsDNA Reagent	Thermo Scientific	P7581

4.10. Consumables

Consumables such as cell culture dishes, reaction tubes, and other disposable plastic consumables were purchased from Applied Biosystems, Eppendorf, Greiner, Nunc, Sarstedt, and VWR.

4.11. Equipment

Equipment	Supplier
Automated electrophoresis chambers and power supply	Bio-Rad
Chemiluminescence imaging	Bio-Rad ChemiDocTM MP Imaging System, 1708281
Cell culture incubator	Thermo Scientific, HERA cell 150i
Cell counter	LunaTM Automated Cell Counter
Centrifuges	Eppendorf 5417R
	Eppendorf 5424
	VWR PCR plate spinner
Deep-sequencer	Genome Analyzer IIx (Illumina)
Heating blocks	Accu block digital dry bath
	Eppendorf Thermomixer C
Illumina NextSeq instrument	Illumina NextSeq 500
Immunoblot transfer chamber	BioSTEP
pH meter	Schott Lab850
Photometer	Bio Photometer D30
Microscopes	Motic AE31
	Olympus CKX41
	Olympus BX63
Microtome	LEICA RM2145
PCR thermal cycler	Bio-Rad T100TM Thermal Cycler
Power supply	VWR
Quantitative RT-PCR machine	Bio-Rad CFX Connect Real-Time system
SDS-PAGE system	Bio-Rad
Plate reader	TECAN infinite M200 PRO
Transilluminator	DR-45M
Ultrasonificator	UP50H Ultrasonic Processor
Water bath	VWR VWB12

4.12. Software and online resources

Programs	Supplier
ApE plasmid editor	by M. Wayne Davis
Bio-Rad CFX Manager 3.1	Bio-Rad
GraphPad Prism 8.4.0	GraphPad Prism
Crispr gRNA design tool	http://crispr.mit.edu/
c-Bio Portal	http://www.cbioportal.org/
ImageJ (FIJI)	v.1.51j8, https://imagej.nih.gov/ij/
Image Lab 5.0 software	Bio-Rad
Integrated Genome Browser	Nicol et al., 2009
Kaplan-Meier Plotter	https://kmplot.com/
NIS-Elements BR 3.0	Nikon
Office 365	Microsoft Inc.
R 3.1.1	R foundation
STATISTICA 8.0 software package	Statsoft
UCSC Genome Bioinformatics	http://genome.ucsc.edu
PimerX	http://www.bioinformatics.org/primerx/
Primer bank	https://pga.mgh.harvard.edu/primerbank/

5. Methods

5.1. Cell biology methods

5.1.1. Cultivation of mammalian cells

All cell lines were cultured in an incubator at 37 °C, 5 % CO_2 and normoxic conditions (21 % O_2) and relative humidity of 95 % in tissue culture dishes.

Maintenance and passaging of cells. Cell lines were maintained in culture up to 3 months depending on their proliferation rate. To avoid artifacts related to passaging and aging cells were passaged not more than 30 times after thawing. New cell lines generated after transient transfection or transduction were expanded after the final selection and cryopreserved at earliest possible passages.

Cells were subcultured upon reaching 80-90 % confluency. After removal of the medium cells were washed with PBS and further incubated with 0.125 % trypsin/EDTA solution for 5-8 min to detach the cells from the culture dishes. Then, full culture medium with 10 % FBS was added to neutralize the trypsin and the suspension centrifuged at 1000 rpm for 5 min. Next, the supernatant was discarded, cells resuspended in fresh medium and seeded onto new culture dishes at ratios ranging between 1:5 and 1:20 depending on the recommendations for a particular cell line. For experiments which required a fixed number of cells, the cell number was estimated with a Neubauer counting chamber. Confluency never exceeded 80 % at the moment of lysis or termination of an experiment.

Cryopreservation of cells. For banking, cells were collected while in the exponential growth phase (estimated as 70-80 % confluency) at the earliest possible passage after generating new lines. For this, cells were trypsinized, centrifuged at 1000 rpm for 3 min, resuspended in cryomedium (cell culture medium with 5 % DMSO or alternatively full medium with 5 % DMSO and 50 % FBS), and

aliquoted in cryovials (1 ml of cell suspension per vial containing approx. half the cells from one Petri dish or 1.5-2 million cells per vial). Vials were then gradually cooled in isopropanol-containing cryoboxes at -80 °C and the next day transferred to boxes at -80 °C or in liquid nitrogen for long term storage.

Thawing of cells. Cryopreserved cells were rapidly thawed in a water bath at 37 °C, after which the cell suspension was transferred to a 15 ml tube with fresh growth medium and centrifuged to remove DMSO. After centrifugation, the supernatant was removed, cells resuspended in fresh complete medium and plated in tissue culture dishes. Next day medium was changed to fresh complete medium, or with medium supplemented with an appropriate antibiotic in case of transduced cells.

5.1.2. Transfection of mammalian cells with plasmid DNA

To generate stable cells one of the methods to introduce plasmid DNA into mammalian cells was used depending on the cell line and purpose (stable transfection, generation of CRISPR Cas9 knockout cells, or production of lentiviral particles). Cells were seeded at an appropriate density 24 h before transfection. On the day of transfection growth medium was replaced with fresh full cell culture medium and the transfection mixture added in a dropwise manner.

Transfection with polyethylenimine (PEI) was used to introduce sleeping beauty transposase and CRISPR-Cas9 vectors into HCT116 and HeLa cells, as well as HEK293T cells. The transfection solution A and B for 1 well of a 6-well plate were prepared as follows:

Solution A	6 µg target DNA	200 µl plain DMEM medium
Solution B	12 µl PEI (1.0 µg/µl)	200 µl plain DMEM medium

After incubation for 5 min at room temperature (RT), solutions were mixed and incubated for further 5-20 min at RT. The final transfection mix was added dropwise to the cells and incubated overnight. Next morning, transfection medium was replaced with fresh cell culture medium.

For transfections with transposons and the sleeping beauty transposase the following mixture was used: 2 µg of the sleeping beauty transposase SB100 with 4 µg of the TST-206 transposon vector. 48 hours post transfection puromycin was applied for selection of transfected cells first at 0.5 µg/ml, followed by 1 µg/ml from the next day.

Calcium phosphate transfection. Cells were seeded one or two days before transfection to achieve a density of approx. 60 % at transfection. On the day of transfection, the medium was changed two hours before adding the DNA mixture with fresh medium supplemented with 25 µM chloroquine. For transfection of cells in a 10 cm dish, 30 µg DNA were mixed with 50 µl 2.5 M $CaCl_2$ and filled up to 500 µl with ddH_2O. 500 µl 2 x HBS buffer were added in a drop wise manner to the reaction while rigorous agitation to generate calcium phosphate-DNA complexes, and the resulting mixture added to the cells. On the next day, cells were washed with PBS to remove DNA precipitates and fresh cell culture medium was added.

5.1.3. Transfection of cells with siRNA

Non-targeting control siRNA and siEZH2 were purchased from Dharmacon. Lyophilized siRNA pools were resuspended in 1 x siRNA buffer (Dharmacon, Cat# B-002000-UB-100), aliquoted, and stored frozen at -20 °C. Transfection of cells with siRNAs was performed using the DharmaFECT 1 transfection reagent (Dharmacon, catalog ID: T-2001-03). Cells were transfected, at a 50-60 %

confluence. Transfection mixture was prepared according to the manufacturers' instructions for one well in a 12-well plate in three steps:

Solution 1, 100 µl	8.5 µl siRNA (5 µM)	91.5 µl Opti-MEM
Solution 2, 100 µl	4.125 µl Dharmafect 1	95.8 µl Opti-MEM

The final transfection mix was produced by combining mixtures 1 and 2, followed by an incubation period of 15 min at RT. Next, 0.8 ml of cell culture medium were added to the transfection mixture and the cell medium in the wells was replaced with 1 ml of the transfection mixture. Next day, the medium was once again replaced with fresh culture medium. Cells were incubated for 72 hours before the start of the following experiments. To expand the cells for further experiments, 24 hours post transfection cells were plated into 6-well plates or 6 cm dishes. Knockdown efficiency was validated by qPCR and immunoblot.

5.1.4. Production of lentiviruses in HEK293T cells and transduction of mammalian cells

Recombinant lentiviruses were produced in the S2 facility of CCCM Würzburg and Department of Internal Medicine VIII, University Hospital Tübingen.

Human embryonic kidney cells HEK293T were used as the producer line. Five million cells were seeded into 10 cm cell culture dishes one day prior to transfection. Second generation packaging plasmids (pCI-VSVG-Env and psPAX2) were used for virus production. 25 µg of the transfer plasmid and 12.5 µg of each of the packaging plasmids were co-transfected into the HEK cells by calcium phosphate transfection as described before. In case of transfection with PEI, the following mixtures were used:

Solution A	11.2 µg target DNA 2.8 µg psPAX2 1.4 µg pCI-VSVG-Env	650 µl Opti-MEM serum reduced medium

Solution B	30 µl PEI (1.0 µg/µl)	670 µl Opti-MEM serum reduced medium

After combining the solutions A and B, the resulting mixture was incubated for 20 min. The medium was removed from the dishes with HEK cells and fresh culture medium was added 2 hours prior to the transfection.

Transfection medium was distributed dropwise onto the HEK cells. The virus-containing supernatant was harvested twice: 48 h and 72 h after the transfection. The supernatants were passed through a 0.45 µm filter to remove any cell debris and used directly for transduction of target cells. Selection with appropriate antibiotics was initiated 24 or 48 h post transduction.

5.1.5. Cell migration in the wound healing assay

Cell motility was assessed in the wound healing migration assay. For this, 2 x 10^5 or 4 x 10^5 cells (RCC or Hela cells, respectively) were plated in 6-well cell culture plates and treated with appropriate compounds (e.g. PT2385). When the monolayer reached 90-100 % confluence, three-four lanes (scratches) were manually applied using the yellow tip. Afterwards, cells were washed once with PBS to remove detached cells and fresh media with the drugs was added. Pictures were taken at 0, 12, 24, and 48 hours after generating of the wound with the inverted Motic AE31 microscope. Images were further analyzed with ImageJ. Cell migration was estimated as covered area at indicated timepoints relative to the start area in the beginning of the experiment and was calculated according to the formula:

$$\text{Cell migration} = 1 - \frac{\text{Uncovered area at indicated timepoint}}{\text{Uncovered area at 0 timepoint}}.$$

5.1.6. Modified Boyden chamber matrigel invasion assay

The capacity of cells to invade was estimated using the modified Boyden chamber assay. The principal difference between the modified version of the protocol and the original assay is that in the modified Boyden chamber assay cells first must invade through an ECM matrix – matrigel – to migrate through the porous membrane. In addition, the number of invaded cells was always normalized to the numbers of initially plated cells in the top compartment of the chamber.

To assess invasion, cells were trypsinized, counted, and resuspended in diluted matrigel (1:10 or 1:5 depending on the cell line). 35 thousand cells in 100 µl of diluted Matrigel were seeded per one well in the upper compartment of the inserts (Corning, Cat# 3422) in a 24-well plate on top of a porous membrane (pore size – 8 µm). Three or four wells were seeded per each condition. The suspensions were allowed to polymerize in the incubator at 37 °C for 1 h. Next, the polymerized matrigel containing cells was carefully overlaid with medium containing 1 % FBS, while 600 µl of complete growth medium (10 % FBS) were added to the lower compartment. The difference in FBS percentage in the medium between the upper and lower compartments created a gradient of nutrients and chemokines directing cell migration towards the lower compartment. After 16 hours of incubation of the inserts in an incubator, invasion was stopped by replacing the medium in the lower compartment to 70 % ethanol. Cells were fixed for 10 min at RT, then the ethanol was replaced with PBS and cells were let to rehydrate for another 10 min. Next, the nuclei of cells were stained with DAPI. For this, PBS from the lower compartment was replaced to a DAPI solution (2.5 µg/ml DAPI in 1 x PBS), and the inserts incubated for 10 min at RT. The inserts were then washed for 10 min in PBS, after which pictures were taken of the DAPI stained nuclei in the upper compartment using a fluorescent Olympus microscope (Olympus CKX41) with a 4 x objective. In the end, medium and matrigel were completely removed from the lower and

upper compartments, membranes detached from the insert walls and placed on glass slides. A drop of fluorescent mounting medium (Abcam, ab128982) was placed on top of the membranes and sealed with a cover glass. Afterwards, fluorescent pictures were taken from the fixed membranes with the 4 x objective.

The number of cells in the upper and lower compartment of the membrane was estimated by counting DAPI stained nuclei in ImageJ (1.8.0_112, https://imagej.nih.gov/ij/index.html). Invasion rate was determined according to the following formula:

$$\text{Invasion index} = \frac{\text{No of cells in the lower compartment}}{\text{No of cells in the upper compartment}}$$

The final result was presented as a relative invasion score where invasion index of each test-condition was normalized to the appropriate control.

5.1.7. Immunofluorescent staining of cells on coverslips

For immunofluorescence staining, cells were seeded on sterile 10 mm glass coverslips placed in 6-well plates. Cells were washed once with PBS, fixed with 1 or 4 % PFA for 15 min at RT, and washed twice with PBS. Coverslips were then placed on parafilm and cells permeabilized with 0.5 % Triton X-100 in TBS for 10-15 min. Afterwards, coverslips were washed twice with TBS, followed by blocking with 2.5 % BSA in TBS for 30 min at RT. Afterwards, the following steps were performed: 1) one hour of incubation with the primary antibodies diluted in the IF blocking buffer at RT, followed by three washing steps with TBS for 5 min; 2) one hour of incubation in the dark at RT with fluorophore-conjugated secondary antibodies (all used in the dilution 1:200 in the IF blocking buffer), followed by three washing steps with TBS; 3) 10 min incubation at RT with Hoechst (5 µg/ml in TBS), followed with three final washing steps with TBS, and one in ddH_2O. Afterwards, a drop of fluorescent mounting medium was placed on the coverslips and they were positioned on microscope slides (alternatively, after step 2 coverslips

were washed with ddH_2O and mounted with the DAPI-containing mounting medium, VECTASHIELD HardSet Antifade Mounting Medium with DAPI, H-1500). Epifluorescence images were taken using the Olympus microscope BX63 with 40 x and 60 x immersion objectives. Images were further processed in ImageJ. At least 10 pictures per slide were taken and at least 50 cells were quantified for statistical analysis.

5.2. Biochemical methods

5.2.1. Preparation of whole cell protein extracts

For whole cell protein extraction, cells were detached by trypsinization, centrifuged, and pellets lysed in the Laemmli lysis buffer. Alternatively, cells were washed with ice-cold PBS and scraped with a silicon policeman directly in the Laemmli lysis buffer. The lysates were transferred into 1.5 ml Eppendorf tubes and subjected to sonification using the following parameters (UP50H Ultrasonic Processor): cycle 100 %, amplitude 30-40 %, duration of the pulse 30 sec - 1 min until the suspension became homogenous indicating that the DNA was sufficiently shared. Then, protein lysates were heated for 5 min at 95 °C and frozen at -20 °C or subjected to immunoblotting. Protein concentration was determined with the BCA assay.

5.2.2. Total protein quantification by the bicinchoninic acid colorimetric assay (BCA)

Quantification of the total protein concentration in lysates with TNT or Laemmli buffers was performed using the BCA assay. For the assay, 5 µl of the protein lysate were pipetted into a well of a transparent flat-bottomed 96-well plate and mixed with 100 µl BCA reagent consisting of buffer A and buffer B (50:1). The

reaction was incubated for 30 min at 37 °C and the absorbance measured at a wavelength of 560 nm. A well containing only the lysis buffer with the BCA reagent served as the blank control. Protein concentration was determined on the basis of a standard curve which was built in advance for each type of the lysis buffer.

5.2.3. SDS polyacrylamide gel electrophoresis (SDS-PAGE) and immunoblot

SDS polyacrylamide gel electrophoresis was applied to separate proteins based on their molecular weight. First, samples were normalized according to their protein concentration. For 1 mm thick gels 12.5-25 µg of the protein and 25-50 µg for a 1.5 mm gels were loaded per lane. Protein lysates were boiled in 6 x Laemmli sample buffer for 5 min at 95 °C, centrifuged, and equal protein amounts and volumes were loaded into Bis-Tris polyacrylamide gels consisting of 8-12 % stacking and 4 % resolving gels. The Page Ruler Pre-Stained Protein Ladder (Fermentas) was used as a molecular weight marker. Separation of the proteins was performed using the SDS-PAGE chambers (Bio-Rad) at 80-120 V in the 1 x MOPS running buffer containing freshly added sodium bisulfite.

Protein transfer. Following separation by SDS-PAGE, the proteins were transferred onto a PVDF membrane for immunoblotting. PVDF membranes were first activated in 100 % methanol and then soaked in the transfer buffer together with sponges, gels and filter papers. The transfer sandwich was assembled in the following sequence: sponge – filter papers – membrane – gel – filter papers – sponge. Wet transfer was performed with the transfer sandwiches in a transfer cassette filled with the transfer buffer at 125 V at 4 °C for 2 hours.

Immunoblot. After transfer, the membranes were washed with water and blocked for 30 min in the blocking buffer followed by incubation with primary antibodies at 4 °C overnight. Afterwards, membranes were washed three times for 15-20 min

with 1 x TBS-T and incubated for 1.5-2 hours with secondary antibodies (diluted 1:3000 in the blocking solution) followed by additional three washing steps with TBS-T, and once with PBS to remove residues of Triton X-100 which is a peroxidase inhibitor. Antibodies were visualized by chemiluminescence using the Immobilon Western Substrate (Millipore) according to the manufacturer's instructions and detected with the ChemiDocTM MP Imaging System.

Stripping of PVDF membranes. To remove antibodies, the membranes were incubates for 20 min at 50 °C in the stripping buffer. Next, the membranes were washed thoroughly first with tap water, then distilled water, and finally with TBS-T to remove any residual striping buffer before blocking. Afterwards, the membranes were blocked and subjected to the usual immunoblotting procedure.

5.2.4. Coomassie G250 staining of proteins in polyacrylamide gels

To analyze immuneprecipitated proteins before mass spectrometry, eluates were subjected to SDS-PAGE and stained with Coomassie G250. The gels were incubated for 2 hours in the Coomassie G250 fixing/staining solution (0.5 % Coomassie Brilliant Blue G250, 50 % methanol, and 10 % acetic acid) followed by several change of dH_2O and an overnight de-staining in dH_2O (until protein bands were visible with the weakest background possible). Gels were visualized by Bio-Rad Gel Imager 1708281 with integrated automatic parameters for imaging Coomassie stained gels.

5.2.5. Cycloheximide decay assay

To determine the rate of protein turnover, a cycloheximide decay assay was employed. For that, cells were incubated with 50 µg/ml cycloheximide for a different period of time. Then, cells were washed with ice-cold PBS and directly lysed in the Laemmli lysis buffer or trypsinized, centrifuged, the resulting cell

pellets washed with ice-cold PBS, and then lyzed in the Laemmli lysis buffer. Cell lysates were sonicated as described above, and the lysates analyzed by SDS-PAGE and immunoblot.

5.2.6. Immunoprecipitation for interaction studies

For immunoprecipitation of endogenous proteins cell extracts were prepared in native non-denaturing conditions.

HIF2α/ARNT interaction. 786O or A498 cells overexpressing the HA-tagged HIF2α were plated on 6 cm dishes and treated with the indicated doses of the PT2385 inhibitor overnight. The next day, cells were washed twice with PBS, lysed with the ice-cold TNT150-Glycerol lysis buffer, scraped with a silicone policeman, and kept on ice for 30 min. Then, the lysates were centrifuged for 15 min at 10'000 rpm at 4 °C. 10 % of the supernatant were taken as input, while the rest used for immunoprecipitation with 1 µg of the anti-ARNT antibodies and an appropriate IgG control, and Protein A agarose beads or 10-15 µl of anti-HA mouse conjugated agarose beads. The reaction mix was incubated on a rotating platform at 4 °C for 4 hours to overnight. Afterwards, beads were collected by brief centrifugation, washed with ice-cold NETN buffer twice at 4 °C for 5-15 min each wash. Alternatively, cells were grown in 6 well plates, treated with the PT2385 inhibitor overnight, and the next day collected by trypsinization and processed as described above.

HCT116 cells overexpressing the Flag-tagged HIF2α were treated with 100 µM DFO overnight and the next day with 10 µM MG132 for 2 hours to block protein degradation. Then, the cells were washed twice with PBS, lysed, and processed as described above.

To elute the protein complexes, the beads and inputs were incubated with 35-40 µl DTT sample lysis buffer at 95 °C for 10 min with occasional agitation. The

resulting protein lysates were separated by SDS-PAGE electrophoresis and analyzed by immunoblotting.

Immunoprecipitation for mass spectrometry. HCT116 cells overexpressing the Flag-tagged HIF2α were plated into 15 cm dishes. Upon reaching 60 % confluency, the cells were treated with 100 μM DFO overnight to chemically mimic hypoxia. The next day cells were washed with PBS, detached by trypsinization and resuspended in ice-cold culture medium. Next, the cells were centrifuged at 4 °C for 5 min at 1200 rpm, the supernatant discarded, and the cells washed once with PBS to remove any residues of trypsin or the medium, and finally centrifuged to obtain a cell pellet. The obtained pellets were lysed in TNT300 supplemented with protease and phosphatase inhibitors for 20 min on ice with occasionally agitation. Afterwards, the lysates were diluted with TNT150 and incubated for the next 10 min on ice. Next, lysates were transferred to 2 ml Eppendorf tubes precooled on ice and centrifuged for 15 min at 12’000 rpm at 4 °C. The resulting supernatants were used for immunoprecipitation with 3 μg Sigma anti-Flag M2 antibodies and magnetic Protein G beads overnight. Next day the beads were washed four times (5 min each step) with TNT150 followed by an elution step with the DTT-free elution buffer for 30 min at 37 °C with shaking at 8’000 rpm in a thermal block. 15 % of the protein eluate were precipitated according to the DTT-acetone protocol and subjected for analysis by WB (5 %) and Coomassie G250 staining (10 % of the eluate).

5.2.7. Protein concentration by acetone precipitation

To visualize the efficiency of immunoprecipitation before mass spectrometry, protein eluates were subjected to acetone precipitation. These experiments were performed at 4 °C and the tubes were constantly kept on ice. Four volumes of ice-cold acetone containing 20 mM DTT were added to one volume of the protein

sample. The mixture was mixed and incubated at -20 °C overnight. Next day the samples were centrifuged at 10’000 g for 15 min at 4 °C. Then, the supernatants were discarded, pellets air dried and resuspended in the DTT sample buffer.

5.2.8. Identification of HIF2α interactome by mass spectrometry (MS)

Mass spectrometry analysis of HIF2α interactome in HCT116 cells was performed by Prof. Andreas Schlosser at the Center for Integrative and Translational Bioimaging, Rudolf-Virchow-Zentrum at the Julius-Maximilians-Universität Würzburg.

Gel electrophoresis. Protein precipitation was performed overnight at -20 °C with fourfold volume of acetone. Pellets were washed with acetone at -20 °C. Precipitated proteins were dissolved in NuPAGE LDS sample buffer (Life Technologies), reduced with 50 mM DTT at 70 °C for 10 minutes and alkylated with 120 mM iodoacetamide at room temperature for 20 minutes. Separation was performed on NuPAGE Novex 4-12 % Bis-Tris gels (Life Technologies) with MOPS buffer according to the manufacturer’s instructions. Gels were washed three times for 5 min with water and stained for 1 h with Simply Blue Safe Stain (Life Technologies). After washing with water for 1 h, each gel lane was cut into 15 slices.

In-gel digestion. The excised gel bands were de-stained with 30 % acetonitrile in 0.1 M NH_4HCO_3 (pH 8), shrunk with 100 % acetonitrile, and dried in a vacuum concentrator (Concentrator 5301, Eppendorf, Germany). Digests were performed with 0.1 µg trypsin per gel band overnight at 37 °C in 0.1 M NH_4HCO_3 (pH 8). After removing the supernatant, peptides were extracted from the gel slices with 5 % formic acid, and extracted peptides were pooled with the supernatant.

NanoLC-MS/MS Analysis. NanoLC-MS/MS analyses were performed on an Orbitrap Fusion (Thermo Scientific) equipped with a PicoView Ion Source (New

Objective) and coupled to an EASY-nLC 1000 (Thermo Scientific). Peptides were loaded on capillary columns (PicoFrit, 30 cm x 150 µm ID, New Objective) self-packed with ReproSil-Pur 120 C18-AQ, 1.9 µm (Dr. Maisch) and separated with a 30-minute linear gradient from 3 % to 30 % acetonitrile and 0.1 % formic acid and a flow rate of 500 nl/min.

Both MS and MS/MS scans were acquired in the Orbitrap analyzer with a resolution of 60'000 for MS scans and 7'500 for MS/MS scans. HCD fragmentation with 35 % normalized collision energy was applied. A Top Speed data-dependent MS/MS method with a fixed cycle time of 3 seconds was used. Dynamic exclusion was applied with a repeat count of 1 and an exclusion duration of 30 seconds; singly charged precursors were excluded from selection. Minimum signal threshold for precursor selection was set to 50'000. Predictive AGC was used with AGC a target value of 2e5 for MS scans and 5e4 for MS/MS scans. EASY-IC was used for internal calibration.

MS data analysis. Raw MS data files were analyzed with MaxQuant version 1.6.2.2 (225). Database search was performed with Andromeda, which is integrated in the utilized version of MaxQuant. The search was performed against the UniProt human database. Additionally, a database containing common contaminants was used. The search was performed with tryptic cleavage specificity with 3 allowed miscleavages. Protein identification was under control of the false-discovery rate (FDR; <1% FDR on protein and PSM level). In addition to MaxQuant default settings, the search was performed against following variable modifications: protein N-terminal acetylation, Gln to pyro-Glu formation (N-term. Gln) and oxidation (Met). Carbamidomethyl (Cys) was set as fixed modification. Further data analysis was performed using R scripts developed in-house. Missing LFQ intensities in the control samples were imputed with values close to the baseline. Data imputation was performed with values from a standard normal distribution

with a mean of the 5 % quantile of the combined log10-transformed LFQ intensities and a standard deviation of 0.1. For the identification of significantly enriched proteins, boxplot outliers were identified in intensity bins of at least 300 proteins. Log2 transformed protein ratios of sample versus control with values outside a 1.5 x (significance 1) or 3 x (significance 2) interquartile range (IQR), respectively, were considered as significantly enriched. GoTerms were added using Perseus (226).

5.2.9. Chromatin immunoprecipitation (ChIP)

Chromatin immunoprecipitation was performed to detect interactions of proteins with DNA. In brief, proteins were crosslinked to DNA by 1 % formaldehyde, chromatin subsequently isolated and fragmented. Protein-DNA fragments were then precipitated using specific antibodies against the protein of interest and enrichment for the bound DNA assessed by quantitative real-time PCR using primers for a specific DNA sequence or subjected to sequencing.

Protein/DNA crosslinking and isolation of chromatin. For a ChIP assay cells were grown in 15 cm dishes per each IP (or half of cells in a 15 cm dish for a histone IP) which equals to approximately 7.5-8 million cells. To crosslink proteins with DNA, the cells were fixed with 1 % formaldehyde for 10 min at RT under gentle agitation. Formaldehyde crosslinking was then terminated by addition of glycine to a final concentration of 125 mM and incubation for 5 min at RT on a shaker. Next steps were carried out on ice or at 4 °C. Cells were washed twice with ice-cold PBS and scraped off the plates in PBS and pelleted by centrifugation for 10 min at 4’000 g. The pellets were then resuspended in 5 ml hypotonic ChIP swelling buffer (the volume was adjusted depending on the size of the cell pellet) containing proteinase and phosphatase inhibitors and incubated for 10 min on ice.

Then, lysed and permeabilized cells were pelleted by centrifugation for 10 min at 4000 g.

To obtain the proper size of the chromatin in a range of 150-1000 bp, enzymatic digestion had been employed. Nuclei were washed in the MNase buffer, transferred to 1.5 ml Eppendorf tubes, and centrifuged briefly at high speed. The nuclei were then resuspended in 200 µl of 1 x MNase digestion buffer with the appropriate amount of MNAse (7.5 µl of 1:10 diluted micrococcus nuclease enzyme) and incubated for 18-20 min at 37 °C under constant agitation at 1000 rpm. The enzymatic reaction was stopped by addition of 20 µl of 0.5 M EDTA, mixed, incubated for 5 min on ice, and centrifuged at 13'000 rpm for 1 min. The pelleted nuclei were then resuspended in the nuclei lysis buffer and incubated for 10 min. To shear the nuclear membrane and release chromatin, suspensions of nuclei were sonicated with the UP50H Ultrasonic Processor for 5-7 min at 50 % amplitude and 50 % cycles (30 s pulse followed by 1 min break), and incubated on ice for additional 10 min. Efficiency of the nuclei lysis and chromatin release was assessed under the microscope. Then, chromatin was separated from the nuclei debris by centrifugation at 14'000 rpm for 10 min. 2.5-5 % of the chromatin was taken as input and the remaining fraction diluted 10-fold with the ChIP dilution buffer. Size of the fragmented chromatin was determined before immunoprecipitation. After size control, chromatin was centrifuged for additional 10 min at 13'000 rpm and the supernatant containing the soluble chromatin was transferred into 1.5 ml low-binding microtubes.

Chromatin size control. Twenty microliters of the obtained chromatin (adjusted with ddH_2O) were diluted with 380 µl ChIP elution buffer, 16.8 µl 5M NaCl were then added and the samples incubated at 65 °C for 6 h under constant agitation. Then, 1 µl RNase A (10 mg/ml stock solution) was added followed by an incubation at 37 °C for 1 h. Afterwards, 2 µl proteinase K (1 mg/ml stock solution)

was added and the samples incubated at 45 °C for 2 h in a thermal shaker. Chromatin was purified by phenol-chloroform extraction, precipitated with 100 % ethanol and 3 M Na-acetate, and washed with 80 % ethanol. The resulting DNA was air-dried, solubilized in 20 µl ddH_2O and loaded with 6 x DNA loading buffer in a 2 % agarose gel.

Chromatin immunoprecipitation. The remaining chromatin was divided into 2 tubes for IgG- and target protein-IP. 1-3 µg IgG or the specific antibody against the target protein were added to the chromatin and the samples rotated overnight at 4 °C. The next day Protein A or G magnetic beads in the amount suggested by the manufacturer were washed with the ChIP-IP buffer, resuspended in the same buffer, distributed between the reactions, and incubated for additional 5 hours. Afterwards, the beads were washed three times with the ChIP wash buffer, RIPA high salt buffer, the RIPA LiCl buffer, and finally once with the TE buffer. For each washing step, the beads were incubated on ice for 5 min with occasional mixing by flipping the tube. After each washing step the beads were centrifuged at 3'000 rpm for 2 min and collected with a magnet. The supernatants were removed by aspiration.

DNA elution, reverse-crosslinking and purification. To elute the captured chromatin, beads were incubated with 300 µl of the direct elution buffer at 65 °C for 1 hour under intensive shaking. The input and the beads were incubated with 2 µl RNAse A in 300 µl of the direct elution buffer for 1 h at 37 °C followed by an overnight incubation at 65 °C under intensive shaking to reverse-crosslink and release the DNA from the proteins. Next, samples were incubated with 3 µl proteinase K and incubated at 45 °C for 2 h to digest the proteins.

Purification of the ChIP DNA. DNA was purified using the MinElute PCR Purification Kit (Qiagen) according to the manufacturer's instructions. DNA was eluted from the column with 25 µl elution buffer. Alternatively, ChIP DNA was

purified by ethanol precipitation. For that, an equal volume of phenol-chloroform-isoamyl alcohol was added to the samples, vigorously mixed for 30 sec and centrifuged at 15'000 g for 5 min at RT. Then, the top aqueous phase (approx. 250-275 µl) was transferred to new 1.5 ml Eppendorf tubes and mixed with 1 µl Glycoblue (Thermo Scientific), 1/10th of the sample volume 3M Na-acetate pH 5.2, and 2.5 sample volumes of 100 % ethanol followed by an overnight incubation at -20 °C. Precipitated DNA was then collected by centrifugation for 30 min at 13'000 rpm at 4 °C. The resulting DNA pellet was finally washed with 75 % ethanol, air dried, and dissolved in 50 µl 0.1 x TE buffer.

To estimate the enrichment of DNA at specific genomic sites, qPCR was performed with 0.5 µl of DNA per reaction.

5.3. Next-generation sequencing

5.3.1. RNA sequencing: mRNA isolation, size selection, and cDNA synthesis

For RNA sequencing total RNA was isolated with RNeasy Mini Columns from cells *in vitro*. In case of RNA isolation from mouse tumor nodules, tumor tissue was homogenized with Eppendorf pestles in 1 ml of Trizol and then processed according to the manufacturer's instructions.

Quality of the isolated RNA was analyzed using the Experion Automated Electrophoresis System (Bio-Rad) with RNA standard sense chips according to the manufacturer's protocol. RNA used for RNA sequencing had at least an RNA integrity number (RIN) of 9 on the scale from 1 to 10. Alternatively, RNA integrity was verified with formamide agarose gel electrophoresis.

After quality analysis, 1 µg of total RNA was used to isolate mRNA with the NEBNext Poly(A) mRNA Magnetic Isolation Module according to the manufacturer's instructions. Agencourt AMPure XP Beads (Beckman Coulter) or

Highprep PCR magnetic beads (Magbio) were used to purify the double stranded cDNA which was then used for library preparation.

cDNA libraries were synthesized using a kit for Illumina. To enrich the isolated cDNA, 12 cycles of PCR were used. Final size, amount, and quality of the libraries were evaluated with DNA ChIP (Bio-Rad) or electrophoresis in 1.2 % agarose gels.

5.3.2. ChIP sequencing

For ChIP sequencing initially the standard ChIP procedure was performed. For EZH2 ChIP sequencing the number of reactions, and hence cells, antibodies, and dynabeads were doubled. Precipitated and purified DNA was solubilized in 25 µl ddH_2O and quantified using the Quanti-iTTM PicoGreen dsDNA Assay Kit (Life Technologies).

ChIP-Seq DNA libraries were prepared with the NEBNext Ultra II DNA Library Prep Kit for Illumina following the manufacturer's protocol with minor modifications. Precipitated ChIP DNA was purified with a double volume of HighPrep PCR beads. Then, DNA was enriched with 3-5 PCR cycles and again cleaned from the PCR buffer and oligos with HighPrep PCR beads. The resulting purified DNA was loaded in 1.5 % agarose gels and eventually extracted with the Monarch DNA Gel Extraction Kit (size selection in the range of 200-750 bp). DNA libraries were then amplified with additional five PCR cycles and the concentration estimated with the Quanti-iTTM PicoGreen dsDNA Assay Kit.

Sequencing of the DNA libraries was performed using the Illumina NextSeq 500 instrument at the Biocenter, Julius-Maximillian University Würzburg, or at the Core Unit Systemmedizin, University of Würzburg.

5.3.3. RNA-Seq and ChIP-Seq data analysis

All bioinformatic analyses of ChIP and RNA sequencing data were performed by Prof. Dr. Nikita Popov and Valentina Andrioletti. The reads were aligned to the human genome GRCh38/hg38 with STAR aligner (Dobin et al., 2013). Independent ChIP-qPCR assays were performed to validate the individual peaks identified by ChIP sequencing with the primers listed in section 4.3.1.

5.4. Molecular biology methods

5.4.1. RNA isolation

RNA isolation was performed using the columns or the TRI isolation reagent.

To isolate RNA from cells, TRI RNA isolation reagent (Sigma) was used according to the manufacturer's protocol. In brief, cells were collected by trypsinization and resuspended in the TRI reagent for lysis. Then, bromphenol was added, vigorously mixed and briefly centrifuged. To precipitate RNA, the upper transparent aqueous phase containing RNA was transferred into a fresh tube followed by addition of an equal volume of isopropanol. RNA was pelleted and washed twice with 75 % ethanol to remove any residual phenol components which might inhibit subsequent enzymatic reactions. RNA pellet was resuspended in 50 µl RNAse and DNAse free water and the concentration quantified with a Nanodrop spectrophotometer. The RNA was used for cDNA synthesis and stored at -80 °C.

RNA isolation from cells for RNA sequencing was performed using the RNeasy Quiagen Kit (Cat# 74104) following the manufacturer's instructions. Briefly, the kit provides a spin column-based platform for RNA isolation which relies on the ability of RNA molecules to reversibly bind silica membranes. Cells were first lysed in a denaturing guanidine-thiocyanate buffer (RLT buffer with addition of β-mercaptoethanol). Then, ethanol was added to ensure proper RNA binding and the

lysates loaded onto binding columns containing silica membranes and centrifuged. Contaminants were then removed in several washing steps and highly pure RNA eluted in DEPC-treated water. Upon isolation, RNA concentration was determined using the Nanodrop spectrophotometer and processed accordingly. The residual RNA was stored at -80 °C until reverse transcription.

5.4.2. RNA quality control by electrophoresis

The quality of isolated RNA, which is important for RNA sequencing analysis, was assessed with electrophoresis in agarose gels with formamide or with a commercial RNA chip. In the first case, 1.2 % agarose solution in 1 x TAE buffer was prepared with 0.3 µg/ml ethidium bromide. To prevent RNA degradation, formamide was added to the samples as follows: 3 µg RNA were diluted with water to 15 µl and mixed with an equal volume of the 2 x RNA loading dye. Next, the mixture was heated at 65 °C for 7 min followed by immediate chilling on ice. 2 µg were loaded into the pocket and run at 60 V for 1 hour in ice-cold 1 x TAE buffer at 4 °C. Images of the RNA gels were taken and analyzed using the ImageJ software. This method allows to visualize the bands from rRNA peaks. The height of the 28S and 18S bands can be compared, with a 2:1 ratio indicating non-degraded RNA.

Additionally, quality of the RNA was analyzed using the Experion Automated Electrophoresis System (Bio-Rad) with the RNA standard chips according to the manufacturer's protocol. RNA used for RNA sequencing had at least an RNA integrity number (RIN) of 9 (RIN can range from 10 in completely intact RNA to 1 in degraded samples).

5.4.3. cDNA synthesis by reverse transcription (RT)

To analyze the expression of specific genes or clone the cDNA of a particular gene, cDNA was synthesized from total RNA in a reverse transcription reaction with

random hexamers. At first, RNA was denatured and annealed with random oligos as following: 2 µl of 500 µM random hexamers were mixed with 2 µg of total RNA and diluted to 15 µl with nuclease-free water following by incubation at 70 °C for 5 min to denature RNA and let the oligos bind to the RNA. After a brief incubation on ice, 35 µl of cDNA synthesis mix were added to the denatured RNA samples as follows:

Table 5.1. cDNA synthesis mix

1 x 50 µl Reaction mix	**Component**
15 µl	RNA with random hexamers, denatured and annealed
10 µl	5 x M-MLV reverse transcriptase reaction buffer (Promega)
1.25 µl	10 mM dNTPs (Sigma)
1 µl	RiboLock RNase Inhibitor (40 U/µl, Thermo)
1 µl	M-MLV reverse transcriptase (200 U/µl, Promega)
Up to 35 µl	Nuclease-free water

Table 5.2. cDNA synthesis protocol

Temperature	**Time**
25 °C	10 min
37 °C	60 min
70 °C	15 min
4 °C	Hold

After synthesis, cDNA was diluted to a final concentration of 8 ng/µl with DEPC-treated water and 5 µl of the diluted cDNA (40 ng) were used per one quantitative PCR reaction. For cloning, 40-60 ng of cDNA were used in the PCR reaction.

5.4.4. Polymerase chain reaction (PCR)

PCR for DNA cloning. To generate DNA fragments, the target DNA was amplified from cDNA or plasmid DNA as templates. The reaction mix was set up with the following components (Table 5.3.) and the reaction performed in a PCR amplifier (Table 5.4.).

Table 5.3. Components of a PCR mix

Component	**25 µl reaction**
5 x Phusion HF or GC Buffer	5 µl
10 mM dNTPs	0.5 µl
10 µM forward primer	1.25 µl
10 µM reverse primer	1.25 µl
Template DNA	1-50 ng
DMSO (optional)	0.75 µl
Phusion DNA Polymerase	0.25-0.5 µl
Nuclease-free water	to 25 µl

Table 5.4. Standard thermocycling conditions

Step	**Temperature**	**Time**	**Cycles**
Initial denaturation	98 °C	30 s	1 x
Denaturation Annealing Extension	98 °C 50-62 °C 72 °C	30 s 20-30 s 30 s per 1 kb	20-30 x
Final extension	72 °C	10 min	1 x

Next, synthesized DNA was subjected to restriction digestion (directly in the PCR mix in case of buffer compatibility). Otherwise, the reaction mix was purified with the PCR purification kit (Sigma) and then used for restriction. Finally, the digested DNA was loaded with 6 x loading buffer to pockets in an agarose gel, followed by

electrophoretic separation and extraction from the gel with a Sigma gel extraction kit.

PCR for site-directed mutagenesis. To generate point-mutant variants of a desired protein mutagenic PCR was performed. For this purpose, a plasmid containing the wild type coding sequence of a gene was amplified by PCR with specific primers containing mutated nucleotides. The PCR protocol was the same as for cloning, except of primer annealing temperatures which was usually kept low (approx. 50 °C). To destroy the parental wild type template DNA, DpnI digestion was performed as follows: 2 µl DpnI added to PCR mixture and incubated at 37 °C overnight. The product was then diluted 1:5 in ddH_2O for transformation of chemically competent bacteria.

Quantitative real-time PCR (qPCR). Quantitative real-time PCR was employed to analyze mRNA abundance or to assess enrichment of specific DNA fragments after chromatin immunoprecipitation. Abundance of the transcripts was quantified during DNA amplification when a signal from a fluorescent dye which rapidly intercalates into the newly synthesized double-stranded DNA is recorded in real time. The qPCR reaction mixture as described below (Table 5.5.) was incubated under the thermocycling conditions for qPCR (Table 5.6.).

Table 5.5. qPCR reaction mix

Component	**10 µl reaction**
cDNA (see 3.4.1) or DNA from ChIP diluted in nuclease-free water	5 µl
SYBR-Green Mix (Thermo Scientific)	4.5 µl
10 µM forward primer	0.25 µl
10 µM Reverse primer	0.25 µl

Table 5.6. Thermocycling conditions for qPCR

Step	Reaction	Temperature	Time
1	Initial denaturation	94 °C	5 min
2	Denaturation Annealing + extension + fluorescence reading	94 °C 60 °C	15 s 1 min
Step 2 repeated for 40-45 cycles			
3	Final extension	72 °C	10 min
4	Melting curve + fluorescence reading	60-95 °C, Increment of 0.5 °C	1 min

Analysis of relative gene expression was performed using the Livak delta/delta CT method where target gene mRNA is first normalized to the house keeping gene (HPRT or hS14), and then – to the respective control sample in a group according to the following formulas:

$$\Delta CT = CT_{target} - CT_{HPRT}$$

$$\Delta\Delta CT = \Delta CT_{treatment} - \Delta CT_{control}$$

$$\text{Enrichment (fold)} = 2^{-\Delta\Delta CT}$$

For ChIP experiments the result was presented as percent of input:

$$\text{Percent input} = 100 \times 2^{(\text{Adjusted input}) - Ct(IP))}$$

To adjust the input to 100 % in case 1 % of the ChIP reaction mixture was taken for qPCR, the calculation was as follows:

$$Ct\ input - \log_2 100$$

For 1 % input, Adjusted input = Ct input - 6.644, where 6.644 is coming from $\log_2 100$. In case the input was further diluted 1:5 times (to a final dilution of 500-fold), Adjusted input = Ct input – 8.97 ($\log_2 500 = 8.97$).

Data in figures containing qPCR results represent an average from three technical replicates with the standard error of the mean (SEM).

5.4.5. Transformation of competent cells with plasmid DNA and plasmid amplification

Chemically competent bacteria were thawed on ice and mixed with the ligation mix or 1 µg of plasmid DNA. Bacteria were incubated on ice for 30 min, followed by a heat shock for 45 s at 42 °C. Reactions were then cooled down on ice for 5 min followed by the addition of 900 µl SOC medium and incubation for 1 hour at 37 °C. 100 µl of the resulting bacterial suspension was spread over prewarmed LB agar plates with specific antibiotics or expanded in LB medium in Erlenmeyer flasks overnight at 37 °C and constant agitation for subsequent plasmid preparation. Alternatively, commercially available competent bacterial cells were used for cloning procedures, where 1-10 ng of ligated DNA were used for transformation according to the manufacturer's instructions.

5.4.6. Transformation and plasmid isolation from bacteria

Minipreparation (miniprep) for analysis of plasmid DNA. To analyze the cloned constructs, plasmid DNA was isolated with alkaline lysis. In case bacterial colonies were grown on LB plates after transformation with the ligation or mutagenic PCR products, they were expanded in 2 ml LB medium with antibiotics at 37 °C overnight in a bacterial incubator with agitation. Bacteria pellets were resuspended in 100 µl GTE buffer containing 0.5 µl RNase A, followed by lysis with 200 µl of NaOH/SDS lysis solution for 3 min at RT. Lysis was stopped by addition of 150 µl of the potassium acetate solution. The mixtures were then spun down at 14'000 rpm, 4 °C for 10 min. The supernatants were transferred into a fresh tube and mixed with equal volumes of 100 % isopropanol followed by incubation for 30 min on ice to allow DNA precipitation. The mixtures were then

centrifuged for another 15 min at 14’000 rpm and 4 °C. The resulting DNA pellets were washed with 70 % ethanol, air dried and dissolved in 50 µl TE buffer.

To amplify small amounts of plasmids for transfection, bacteria with the desired plasmids were incubated in 5 ml LB medium and the plasmids isolated with the Miniprep kit (Sigma) according to the manufacturer’s instructions.

Preparative isolation of plasmid DNA (maxiprep). For preparative isolation of plasmid DNA, 200 ml of an overnight bacterial culture were processed according to the manufacturer’s protocol (Sigma plasmid Midiprep and Maxiprep kits). The purified plasmid DNA was solubilized in elution buffer supplies with the kit and adjusted to a concentration of 1 µg/µl. In case lower than 1 µg/µl concentrations of DNA plasmids were achieved, concentration via isopropanol precipitation was performed according to the manufacturer’s instructions.

5.4.7. Analysis of DNA with restriction digestion

To prepare DNA for cloning and for analysis of plasmids isolated from colonies, digestion was performed with restriction enzymes from NEB or Thermo Scientific according to the manufacturer’s recommendations. The digestion reaction mix was prepared as following:

1 µg DNA
0.5 µl restriction enzyme 1
0.5 µl restriction enzyme 2
1 µl 10 x reaction buffer
ddH_2O to 10 µl

Reaction mixtures were incubated for 2-5 hours at the recommended temperature. For overnight restriction digestion, 10 times less quantities of enzymes were used. For specific digestion reactions, such as direct digestion in a PCR reaction mix, the amounts of DNA, enzymes, total reaction volume, and digestion time were optimized.

5.4.8. Electrophoretic separation of DNA in agarose gels

Separation of DNA fragments by gel electrophoresis was performed in 1-2 % agarose gels depending on the expected fragment size in a 1 x TAE buffer. For this purpose, appropriate quantities of agarose were boiled in 1 x TAE buffer, then 1 µg/µl GelGreen or 0.3 µg/ml ethidium bromide were added to a chilled to approx. 50 °C agarose solution and casted in a gel chamber with combs until completely polymerized. Then, DNA samples were mixed with the 6 x DNA loading buffer containing the dye and loaded into the pockets of the gel. The DNA ladder was loaded next to the samples as a marker to estimate the DNA fragments size. Samples were separated at 120 V for one hour and the DNA fragments were visualized with a UV transilluminator.

5.4.9. Extraction and purification of DNA fragments and PCR products

Extraction and purification of DNA fragments was performed with commercially available kits according to the manufacturer's instructions. In brief, this method is column-based and relies on the ability of DNA to reversibly bind the silica membranes upon centrifugation. Purification of PCR products was performed with the PCR purification kit (Sigma). To purify and extract the DNA from agarose gels, the desired fragment was cut out of the gel and extracted with the gel extraction kit (Sigma or NEB).

5.4.10. DNA ligation

Ligation of DNA fragments into backbone vectors was performed with the T4 DNA ligase (Thermo Scientific). The DNA fragment (insert) was used in 3 x molar excess to the linearized and dephosphorylated vector.

Ligation mix, 10 µl:	100-200 ng linearized vector X ng fragment 1 µl T4 DNA ligase 1 µl 10 x ligation buffer ddH_2O to 10 µl

The ligation mix was incubated at 16 °C overnight und transformed into chemically competent bacteria.

5.4.11. Nucleic acid quantification

Nanodrop measurement. The concentration of DNA and RNA was measured with the Bio Photometer spectrophotometer. 2 µl of DNA or RNA were applied to measure the absorbance at 260 nm. The purity was judged by the ratio of absorbance at 260 and 280 nm, where ~1.8 for DNA and ~2.0 for RNA were generally accepted as sufficiently pure.

PicoGreen measurement. Concentrations of dsDNA in ChIP experiments or DNA libraries (ChIP-seqiencing or RNA-sequencing) were quantified with the Quant-iT PicoGreen dsDNA reagent (Invitrogen) according to the manufacturer's protocol. In brief, this is a quantitative fluorescent based method in which DNA concentration is determined as an amount of incorporated PicoGreen with a standard fluorescein excitation and emission wavelengths. The fluorescence of PicoGreen was measured at a wavelengths of 485/535 nm.

Bioanalyzer. RNA to be used for library preparation for RNA-Sequencing (as well as the prepared DNA-libraries) was quantified with the ExperionTM Automated Electrophoresis System from Bio-Rad according to manufacturer's recommendations. In brief, this technology is based on gel electrophoresis and allows multiple measurements in one run. It also automates analysis by combining electrophoresis, staining, destaining, band detection, and imaging in a single step.

5.5. *In vivo* mouse model of ccRCC and CRC

5.5.1. Passive metastasis models and orthotopic kidney transplantation for spontaneous metastasis

All animal experiments in this project were performed in collaboration with Dr. Angel Cuesta at the Margarita Salas Center for Biological Research (CIB M), Spanish National Research Council (CSIC), Madrid, Spain, according to the local and international (FELASA) animal welfare and experimentation regulations.

Immunocompromised NOD scid gamma NMRI-Foxn1nu/nu (NSG) mice were used in animal studies to allow xenotransplantation of human tumor lines. Male 8-10-week-old NSG mice from an own colony were kept in SPF conditions.C57/Bl.6J mice from an own colony were used for experiments with the MCO2 mouse colorectal line.

In all, three metastasis models were used in the study: two passive models (for lung and liver metastasis) and one model of spontaneous metastasis from orthotopically transplanted kidney tumors.

For the passive metastasis model with the human 786O ccRCC line, cells were trypsinized, counted and resuspended in sterile PBS to the final concentration of 10 mln/ml. Then, 100 µl of the suspension were injected into the tail vein of the mice (2 million cells/animal). 50 days after the injection animals were sacrificed, lungs carefully excised and the number of superficial lung metastases counted.

To assess the ability of MCO2 cells overexpressing WT or QMY HIF2α to form metastasis, we employed a passive model where tumor cells are injected into the spleen, resulting in their delivery through the connecting vessels to the liver. For this, mice were anesthetized with a mixture of ketamine/xylazine (100 mg/kg ketamine and 10 mg/kg xylazine dissolved in 0.9 % NaCl solution). After testing for the toe pinch reflex, animals were fixed on the back, the abdominal area shaven

with an automatic razor and cleaned with alcohol. A one-centimeter long midline incision in the skin was made approx. from the middle of the abdomen to the tip of the sternum. The underlying peritoneum was accessed by a slightly shorter incision along the *linea alba*. Next, the spleen was located and partially retrieved from the abdomen by gently pulling on the attached part of the pancreas. Next, a previously prepared suspension of MCO2 cells in sterile PBS (250 thousand cells in 100 µl) was injected directly into the spleen. The spleen was then gently returned to its proper position, peritoneum wall reconnected with resorbable sutures, while the skin was separately closed with non-resorbable sutures. During the surgery and in the postoperative period mice were kept on a heating pad to prevent any complications coming from hypothermia. One month after transplantation the mice were sacrificed, livers removed, and the numbers of superficial metastases recorded.

Lastly, we also tested the ability of RCC cells overexpressing the WT or QMY HIF2α to give rise to spontaneous metastasis after an orthotopic injection of the cells under the kidney capsule. For this, mice were anesthetized as described above. Next, animals were positioned to expose their right flank. One-centimeter long incisions in the skin and the underlying peritoneal wall were made, and the kidney exposed. 1 million 786O ccRCC cells in 50 µl sterile PBS were then injected under the kidney capsule. In the end of the operation the peritoneal wall was closed with resorbable sutures, while the skin was sutured with a non-resorbable line. 75 days after the injection the mice were sacrificed, and the numbers of superficial lung metastases counted.

5.5.2. Quantification of lung and liver metastases

To assess the metastatic dissemination of tumors, in the end of every *in vivo* experiment superficial lung and liver metastases ware quantified. For this, after

being sacrificed by a lethal dose of anesthesia, mice were rapidly dissected, lugs and livers carefully isolated and placed into PBS in Petri dishes. Fresh lung and liver specimens were examined for the presence of superficial metastasis first by the naked eye, then – with the help of a surgical stereomicroscope under a low magnification (2-5 x). Examples of the lung metastases that were quantified are presented in Fig. 12. After quantification of metastases, lungs and livers were fixed in 4 % PFA for further analysis by hematoxylin/eosin staining.

5.6. Hematoxylin and eosin staining of paraffin embedded tumor tissue

To examine metastatic tumor nodules standard hematoxylin and eosin (H/E) staining was used. Hematoxylin stains nucleic acids basophilic structures in the cells, such as DNA in the nuclei, and is detected as a blue color after the staining, while eosin is an acidic dye which stains cytoplasms of cells and the extracellular matrix resulting in various degrees of pink staining (227).

For fixation, resected mouse lungs and livers were fixed in 4 % formalin overnight, after which the fixative was replaced by PBS until further processing. Fixed specimens were subsequently embedded in paraffin at the Department of Pathology, University Hospital Tübingen. Prior to staining, paraffin blocks were cut into 4 μm thick sections and placed onto standard glass slides. H/E staining was carried out according to the following staining protocol:

Table 5.7. Hematoxylin/eosin staining protocol

Step	**Solution**	**Time**
Removal of paraffin	No solutions, 65 °C	20 min
Rehydration	Sequential exposure to xylol, xylol/ethanol, 100 % ethanol, 95 % ethanol, 70 % ethanol, 50 % ethanol, and ddH_2O	Each step – 5 min
Hematoxylin staining of the nuclei	Mayer's hematoxylin solution	8 min
Washing, 2 x	Tap water	Briefly
Blueing of the hematoxylin stain	Running tap water	10 min
Washing	ddH_2O	Briefly
Eosin staining of the cytoplasm	1 % eosin in 70 % ethanol	4 min
Washing, 3 x	ddH_2O	Briefly
Dehydration and clearing:		
70 % ethanol		1 min
95 % ethanol		1 min
100 % ethanol		2 min
Xylene/ethanol		2 min
Xylene		4 min

After xylene, few drops of the mounting medium (Neo-Mount, Millipore) were applied onto the stained sections and coverslips were mounted on top of the stained slices and the slides left to dry overnight.

5.7. Gene expression analysis using the TCGA database

TCGA (The Cancer Genome Atlas) data for gene expression was retrieved using the cBioPortal (http://www.cbioportal.org/; Cerami et al., 2012; Gao et al., 2013). In brief, after specifying the tumor type – either kidney renal clear cell carcinoma

(KIRC) or colorectal adenocarcinoma (CRC) – mRNA z-scores (RNA Seq V2 RSEM) for genes of interest were downloaded and transferred into an Excel table. Then, using the Excel filter function, the retrieved patient dataset was segregated into two groups according to EZH2 expression or metastasis status (patients with EZH2 mRNA z-scores higher than 1.0 and patients with EZH2 z-scores lower than -1, or MTS = 1 and MTS = 0). The cutoff values of -1 and 1 were chosen based on the range of EZH2 expression and available numbers of cases to ensure meaningful statistical analysis. Patients in the two groups were then compared for the expression of various hypoxia response genes and overall survival (by Kaplan-Maier plots).

5.8. Statistical analysis

In this thesis all bars present the average with the standard error of the mean. For statistical analysis, the Mann-Whitney U-test was employed in all cases, unless otherwise indicated. Analysis was performed with the STATISTICA 8.0 software package (Statsoft). Statistical significance was assumed at the following values: $p<0.05$ (*), $p<0.01$ (**), or $p<0.001$ (***).

Literature

1. Rezvani HR, Ali N, Nissen LJ, Harfouche G, de Verneuil H, Taïeb A, et al. HIF-1α in Epidermis: Oxygen Sensing, Cutaneous Angiogenesis, Cancer, and Non-Cancer Disorders. Journal of Investigative Dermatology. 2011;131(9):1793-805.
2. Dunwoodie SL. The role of hypoxia in development of the Mammalian embryo. Dev Cell. 2009;17(6):755-73.
3. Schito L, Semenza GL. Hypoxia-Inducible Factors: Master Regulators of Cancer Progression. Trends in Cancer. 2016;2(12):758-70.
4. Heidegger I, Pircher A, Pichler R. Targeting the Tumor Microenvironment in Renal Cell Cancer Biology and Therapy. Front Oncol. 2019;9:490.
5. Chen J, Ding Z, Peng Y, Pan F, Li J, Zou L, et al. HIF-1α Inhibition Reverses Multidrug Resistance in Colon Cancer Cells via Downregulation of MDR1/P-Glycoprotein. PLOS ONE. 2014;9(6):e98882.
6. Lv Y, Zhao S, Han J, Zheng L, Yang Z, Zhao L. Hypoxia-inducible factor-1α induces multidrug resistance protein in colon cancer. Onco Targets Ther. 2015;8:1941-8.
7. Wigerup C, Påhlman S, Bexell D. Therapeutic targeting of hypoxia and hypoxia-inducible factors in cancer. Pharmacol Ther. 2016;164:152-69.
8. Daskalaki I, Gkikas I, Tavernarakis N. Hypoxia and Selective Autophagy in Cancer Development and Therapy. Frontiers in Cell and Developmental Biology. 2018;6(104).
9. Semenza Gregg L. Hypoxia-Inducible Factors in Physiology and Medicine. Cell. 2012;148(3):399-408.
10. Schödel J, Grampp S, Maher ER, Moch H, Ratcliffe PJ, Russo P, et al. Hypoxia, Hypoxia-inducible Transcription Factors, and Renal Cancer. Eur Urol. 2016;69(4):646-57.
11. Smythies JA, Sun M, Masson N, Salama R, Simpson PD, Murray E, et al. Inherent DNA-binding specificities of the HIF-1α and HIF-2α transcription factors in chromatin. EMBO Rep. 2019;20(1).
12. Lee KY, Gesta S, Boucher J, Wang XL, Kahn CR. The differential role of Hif1β/Arnt and the hypoxic response in adipose function, fibrosis, and inflammation. Cell Metab. 2011;14(4):491-503.
13. Hu CJ, Sataur A, Wang L, Chen H, Simon MC. The N-terminal transactivation domain confers target gene specificity of hypoxia-inducible factors HIF-1alpha and HIF-2alpha. Mol Biol Cell. 2007;18(11):4528-42.
14. Koh MY, Powis G. Passing the baton: the HIF switch. Trends in Biochemical Sciences. 2012;37(9):364-72.

15. McKeown SR. Defining normoxia, physoxia and hypoxia in tumours—implications for treatment response. The British Journal of Radiology. 2014;87(1035):20130676.
16. Carreau A, El Hafny-Rahbi B, Matejuk A, Grillon C, Kieda C. Why is the partial oxygen pressure of human tissues a crucial parameter? Small molecules and hypoxia. Journal of cellular and molecular medicine. 2011;15(6):1239-53.
17. Fallah J, Rini BI. HIF Inhibitors: Status of Current Clinical Development. Curr Oncol Rep. 2019;21(1):6.
18. Motta S, Minici C, Corrada D, Bonati L, Pandini A. Ligand-induced perturbation of the HIF-2α:ARNT dimer dynamics. PLoS Comput Biol. 2018;14(2):e1006021-e.
19. Konietzny R, König A, Wotzlaw C, Bernadini A, Berchner-Pfannschmidt U, Fandrey J. Molecular Imaging. Annals of the New York Academy of Sciences. 2009;1177(1):74-81.
20. Brahimi-Horn MC, Pouysségur J. HIF at a glance. Journal of Cell Science. 2009;122(8):1055-7.
21. Koh MY, Nguyen V, Lemos R, Jr., Darnay BG, Kiriakova G, Abdelmelek M, et al. Hypoxia-induced SUMOylation of E3 ligase HAF determines specific activation of HIF2 in clear-cell renal cell carcinoma. Cancer research. 2015;75(2):316-29.
22. Bae SH, Jeong JW, Park JA, Kim SH, Bae MK, Choi SJ, et al. Sumoylation increases HIF-1alpha stability and its transcriptional activity. Biochem Biophys Res Commun. 2004;324(1):394-400.
23. Seo H-W, Kim E-J, Na H, Lee M-O. Transcriptional activation of hypoxia-inducible factor-1α by HDAC4 and HDAC5 involves differential recruitment of p300 and FIH-1. FEBS Letters. 2009;583(1):55-60.
24. Lisy K, Peet DJ. Turn me on: regulating HIF transcriptional activity. Cell Death & Differentiation. 2008;15(4):642-9.
25. Lee JW, Ko J, Ju C, Eltzschig HK. Hypoxia signaling in human diseases and therapeutic targets. Exp Mol Med. 2019;51(6):1-13.
26. Schödel J, Oikonomopoulos S, Ragoussis J, Pugh CW, Ratcliffe PJ, Mole DR. High-resolution genome-wide mapping of HIF-binding sites by ChIP-seq. Blood. 2011;117(23):e207-e17.
27. Lee M-C, Huang H-J, Chang T-H, Huang H-C, Hsieh S-Y, Chen Y-S, et al. Genome-wide analysis of HIF-2α chromatin binding sites under normoxia in human bronchial epithelial cells (BEAS-2B) suggests its diverse functions. Scientific Reports. 2016;6(1):29311.
28. Yao X, Tan J, Lim KJ, Koh J, Ooi WF, Li Z, et al. VHL Deficiency Drives Enhancer Activation of Oncogenes in Clear Cell Renal Cell Carcinoma. Cancer Discov. 2017;7(11):1284-305.

29. Patel SA, Simon MC. Biology of hypoxia-inducible factor-2α in development and disease. Cell Death & Differentiation. 2008;15(4):628-34.
30. Graham AM, Presnell JS. Hypoxia Inducible Factor (HIF) transcription factor family expansion, diversification, divergence and selection in eukaryotes. PLOS ONE. 2017;12(6):e0179545.
31. Patel SA, Simon MC. Biology of hypoxia-inducible factor-2alpha in development and disease. Cell Death Differ. 2008;15(4):628-34.
32. Ruas JL, Poellinger L, Pereira T. Role of CBP in regulating HIF-1-mediated activation of transcription. Journal of Cell Science. 2005;118(2):301-11.
33. Xiang L, Gilkes DM, Hu H, Luo W, Bullen JW, Liang H, et al. HIF-1α and TAZ serve as reciprocal co-activators in human breast cancer cells. Oncotarget. 2015;6(14):11768-78.
34. Hanna S, Krishnan B, Bailey S, Moschos S, Kuan P-F, Shimamura T, et al. HIF1α and HIF2α independently activate SRC to promote melanoma metastases. The Journal of clinical investigation. 2013;123.
35. Downes NL, Laham-Karam N, Kaikkonen MU, Ylä-Herttuala S. Differential but Complementary HIF1alpha and HIF2alpha Transcriptional Regulation. Molecular Therapy. 2018;26(7):1735-45.
36. Lin Q, Cong X, Yun Z. Differential hypoxic regulation of hypoxia-inducible factors 1alpha and 2alpha. Mol Cancer Res. 2011;9(6):757-65.
37. Keith B, Johnson RS, Simon MC. HIF1α and HIF2α: sibling rivalry in hypoxic tumour growth and progression. Nat Rev Cancer. 2011;12(1):9-22.
38. Imtiyaz HZ, Williams EP, Hickey MM, Patel SA, Durham AC, Yuan LJ, et al. Hypoxia-inducible factor 2alpha regulates macrophage function in mouse models of acute and tumor inflammation. J Clin Invest. 2010;120(8):2699-714.
39. Gerri C, Marín-Juez R, Marass M, Marks A, Maischein H-M, Stainier DYR. Hif-1α regulates macrophage-endothelial interactions during blood vessel development in zebrafish. Nature Communications. 2017;8(1):15492.
40. Simon MC, Keith B. The role of oxygen availability in embryonic development and stem cell function. Nat Rev Mol Cell Biol. 2008;9(4):285-96.
41. Gale M, Yan Q. High-throughput screening to identify inhibitors of lysine demethylases. Epigenomics. 2015;7(1):57-65.
42. Kurt B, Gerl K, Karger C, Schwarzensteiner I, Kurtz A. Chronic Hypoxia-Inducible Transcription Factor-2 Activation Stably Transforms Juxtaglomerular Renin Cells into Fibroblast-Like Cells in vivo. Journal of the American Society of Nephrology. 2015;26(3):587-96.
43. Nanduri J, Semenza GL, Prabhakar NR. Epigenetic changes by DNA methylation in chronic and intermittent hypoxia. Am J Physiol Lung Cell Mol Physiol. 2017;313(6):L1096-L100.

44. Serocki M, Bartoszewska S, Janaszak-Jasiecka A, Ochocka RJ, Collawn JF, Bartoszewski R. miRNAs regulate the HIF switch during hypoxia: a novel therapeutic target. Angiogenesis. 2018;21(2):183-202.
45. Yang C, Sun MG, Matro J, Huynh TT, Rahimpour S, Prchal JT, et al. Novel HIF2A mutations disrupt oxygen sensing, leading to polycythemia, paragangliomas, and somatostatinomas. Blood. 2013;121(13):2563-6.
46. Zhuang Z, Yang C, Lorenzo F, Merino M, Fojo T, Kebebew E, et al. Somatic HIF2A Gain-of-Function Mutations in Paraganglioma with Polycythemia. New England Journal of Medicine. 2012;367(10):922-30.
47. Toledo RA, Qin Y, Srikantan S, Morales NP, Li Q, Deng Y, et al. In vivo and in vitro oncogenic effects of HIF2A mutations in pheochromocytomas and paragangliomas. Endocr Relat Cancer. 2013;20(3):349-59.
48. Toledo RA. New HIF2alpha inhibitors: potential implications as therapeutics for advanced pheochromocytomas and paragangliomas. Endocr Relat Cancer. 2017;24(9):C9-C19.
49. Fliedner SMJ, Shankavaram U, Marzouca G, Elkahloun A, Jochmanova I, Daerr R, et al. Hypoxia-Inducible Factor 2α Mutation-Related Paragangliomas Classify as Discrete Pseudohypoxic Subcluster. Neoplasia. 2016;18(9):567-76.
50. Dang CV, O'Donnell KA, Zeller KI, Nguyen T, Osthus RC, Li F. The c-Myc target gene network. Semin Cancer Biol. 2006;16(4):253-64.
51. Xia X, Lemieux ME, Li W, Carroll JS, Brown M, Liu XS, et al. Integrative analysis of HIF binding and transactivation reveals its role in maintaining histone methylation homeostasis. Proceedings of the National Academy of Sciences. 2009;106(11):4260-5.
52. Wierzbicki PM, Klacz J, Kotulak-Chrzaszcz A, Wronska A, Stanislawowski M, Rybarczyk A, et al. Prognostic significance of VHL, HIF1A, HIF2A, VEGFA and p53 expression in patients with clearcell renal cell carcinoma treated with sunitinib as firstline treatment. Int J Oncol. 2019;55(2):371-90.
53. Oladipupo S, Hu S, Kovalski J, Yao J, Santeford A, Sohn RE, et al. VEGF is essential for hypoxia-inducible factor-mediated neovascularization but dispensable for endothelial sprouting. Proceedings of the National Academy of Sciences of the United States of America. 2011;108(32):13264-9.
54. Ban HS, Kim B-K, Lee H, Kim HM, Harmalkar D, Nam M, et al. The novel hypoxia-inducible factor-1α inhibitor IDF-11774 regulates cancer metabolism, thereby suppressing tumor growth. Cell Death & Disease. 2017;8(6):e2843-e.
55. Kim J-w, Tchernyshyov I, Semenza GL, Dang CV. HIF-1-mediated expression of pyruvate dehydrogenase kinase: A metabolic switch required for cellular adaptation to hypoxia. Cell Metabolism. 2006;3(3):177-85.
56. Del Rey MJ, Valín Á, Usategui A, García-Herrero CM, Sánchez-Aragó M, Cuezva JM, et al. Hif-1α Knockdown Reduces Glycolytic Metabolism and

Induces Cell Death of Human Synovial Fibroblasts Under Normoxic Conditions. Scientific Reports. 2017;7(1):3644.
57. Okamoto A, Sumi C, Tanaka H, Kusunoki M, Iwai T, Nishi K, et al. HIF-1-mediated suppression of mitochondria electron transport chain function confers resistance to lidocaine-induced cell death. Scientific Reports. 2017;7(1):3816.
58. Zhang Y, Liu D, Hu H, Zhang P, Xie R, Cui W. HIF-1α/BNIP3 signaling pathway-induced-autophagy plays protective role during myocardial ischemia-reperfusion injury. Biomedicine & Pharmacotherapy. 2019;120:109464.
59. Huang J, Gao L, Li B, Liu C, Hong S, Min J, et al. Knockdown of Hypoxia-Inducible Factor 1α (HIF-1α) Promotes Autophagy and Inhibits Phosphatidylinositol 3-Kinase (PI3K)/AKT/Mammalian Target of Rapamycin (mTOR) Signaling Pathway in Ovarian Cancer Cells. Med Sci Monit [Internet]. 2019 2019/06//; 25:[4250-63 pp.].
60. Zhao X, Liu L, Li R, Wei X, Luan W, Liu P, et al. Hypoxia-Inducible Factor 1-α (HIF-1α) Induces Apoptosis of Human Uterosacral Ligament Fibroblasts Through the Death Receptor and Mitochondrial Pathways. Med Sci Monit. 2018;24:8722-33.
61. Flamant L, Notte A, Ninane N, Raes M, Michiels C. Anti-apoptotic role of HIF-1 and AP-1 in paclitaxel exposed breast cancer cells under hypoxia. Molecular Cancer. 2010;9(1):191.
62. Koshiji M, Kageyama Y, Pete EA, Horikawa I, Barrett JC, Huang LE. HIF-1α induces cell cycle arrest by functionally counteracting Myc. The EMBO Journal. 2004;23(9):1949-56.
63. Carrera S, Senra J, Acosta MI, Althubiti M, Hammond EM, de Verdier PJ, et al. The Role of the HIF-1α Transcription Factor in Increased Cell Division at Physiological Oxygen Tensions. PLOS ONE. 2014;9(5):e97938.
64. Gordan JD, Bertout JA, Hu C-J, Diehl JA, Simon MC. HIF-2alpha promotes hypoxic cell proliferation by enhancing c-myc transcriptional activity. Cancer Cell. 2007;11(4):335-47.
65. Liu Y, Wu J, Huang W, Weng S, Wang B, Chen Y, et al. Development and validation of a hypoxia-immune-based microenvironment gene signature for risk stratification in gastric cancer. Journal of Translational Medicine. 2020;18(1):201.
66. Doedens AL, Phan AT, Stradner MH, Fujimoto JK, Nguyen JV, Yang E, et al. Hypoxia-inducible factors enhance the effector responses of CD8(+) T cells to persistent antigen. Nature immunology. 2013;14(11):1173-82.
67. Labrousse-Arias D, Martínez-Alonso E, Corral-Escariz M, Bienes-Martínez R, Berridy J, Serrano-Oviedo L, et al. VHL promotes immune response against renal cell carcinoma via NF-κB-dependent regulation of VCAM-1. J Cell Biol. 2017;216(3):835-47.

68. Cho SH, Raybuck AL, Blagih J, Kemboi E, Haase VH, Jones RG, et al. Hypoxia-inducible factors in CD4+ T cells promote metabolism, switch cytokine secretion, and T cell help in humoral immunity. Proceedings of the National Academy of Sciences. 2019;116(18):8975-84.
69. Evans AJ, Russell RC, Roche O, Burry TN, Fish JE, Chow VW, et al. VHL promotes E2 box-dependent E-cadherin transcription by HIF-mediated regulation of SIP1 and snail. Mol Cell Biol. 2007;27(1):157-69.
70. Yang J, Zhang X, Zhang Y, Zhu D, Zhang L, Li Y, et al. HIF-2α promotes epithelial-mesenchymal transition through regulating Twist2 binding to the promoter of E-cadherin in pancreatic cancer. J Exp Clin Cancer Res. 2016;35:26-.
71. Hu F, Deng X, Yang X, Jin H, Gu D, Lv X, et al. Hypoxia upregulates Rab11-family interacting protein 4 through HIF-1α to promote the metastasis of hepatocellular carcinoma. Oncogene. 2015;34(49):6007-17.
72. Chiavarina B, Whitaker-Menezes D, Migneco G, Martinez-Outschoorn UE, Pavlides S, Howell A, et al. HIF1-alpha functions as a tumor promoter in cancer associated fibroblasts, and as a tumor suppressor in breast cancer cells: Autophagy drives compartment-specific oncogenesis. Cell Cycle. 2010;9(17):3534-51.
73. Imamura T, Kikuchi H, Herraiz M-T, Park D-Y, Mizukami Y, Mino-Kenduson M, et al. HIF-1α and HIF-2α have divergent roles in colon cancer. International Journal of Cancer. 2009;124(4):763-71.
74. Steunou A-L, Ducoux-Petit M, Lazar I, Monsarrat B, Erard M, Muller C, et al. Identification of the hypoxia-inducible factor 2α nuclear interactome in melanoma cells reveals master proteins involved in melanoma development. Mol Cell Proteomics. 2013;12(3):736-48.
75. Zhang W, Shi X, Peng Y, Wu M, Zhang P, Xie R, et al. HIF-1α Promotes Epithelial-Mesenchymal Transition and Metastasis through Direct Regulation of ZEB1 in Colorectal Cancer. PLoS One. 2015;10(6):e0129603.
76. Yang S-W, Zhang Z-G, Hao Y-X, Zhao Y-L, Qian F, Shi Y, et al. HIF-1α induces the epithelial-mesenchymal transition in gastric cancer stem cells through the Snail pathway. Oncotarget. 2017;8(6):9535-45.
77. Mazumdar J, Hickey MM, Pant DK, Durham AC, Sweet-Cordero A, Vachani A, et al. HIF-2alpha deletion promotes Kras-driven lung tumor development. Proc Natl Acad Sci U S A. 2010;107(32):14182-7.
78. Kim WY, Perera S, Zhou B, Carretero J, Yeh JJ, Heathcote SA, et al. HIF2α cooperates with RAS to promote lung tumorigenesis in mice. The Journal of Clinical Investigation. 2009;119(8):2160-70.
79. Hong C-F, Chen W-Y, Wu C-W. Upregulation of Wnt signaling under hypoxia promotes lung cancer progression. Oncology Reports. 2017;38.

80. Timar J, Szasz AM, Kardos M, Tokes A, Kulka J, Szendroi M, et al. Expression of HIF1a and HIF2a in bone metastatic clear cell renal cell cancer and use as prognostic markers. Journal of Clinical Oncology. 2013;31(15_suppl):e15523-e.
81. Cho H, Du X, Rizzi JP, Liberzon E, Chakraborty AA, Gao W, et al. On-target efficacy of a HIF-2alpha antagonist in preclinical kidney cancer models. Nature. 2016;539(7627):107-11.
82. Choi H, Chun Y-S, Kim T-Y, Park J-W. HIF-2α Enhances β-Catenin/TCF-Driven Transcription by Interacting with β-Catenin. Cancer Research. 2010;70(24):10101-11.
83. Bouaziz W, Sigaux J, Modrowski D, Devignes C-S, Funck-Brentano T, Richette P, et al. Interaction of HIF1α and β-catenin inhibits matrix metalloproteinase 13 expression and prevents cartilage damage in mice. Proceedings of the National Academy of Sciences. 2016;113(19):5453-8.
84. Hubbi ME, Kshitiz, Gilkes DM, Rey S, Wong CC, Luo W, et al. A nontranscriptional role for HIF-1α as a direct inhibitor of DNA replication. Sci Signal. 2013;6(262):ra10.
85. Chee NT, Lohse I, Brothers SP. mRNA-to-protein translation in hypoxia. Molecular Cancer. 2019;18(1):49.
86. Uniacke J, Holterman CE, Lachance G, Franovic A, Jacob MD, Fabian MR, et al. An oxygen-regulated switch in the protein synthesis machinery. Nature. 2012;486(7401):126-9.
87. Troilo A, Alexander I, Muehl S, Jaramillo D, Knobeloch K-P, Krek W. HIF1α deubiquitination by USP8 is essential for ciliogenesis in normoxia. EMBO reports. 2014;15(1):77-85.
88. Resnick A. HIF Stabilization Weakens Primary Cilia. PLoS One. 2016;11(11):e0165907.
89. Müller S, Djudjaj S, Lange J, Iacovescu M, Goppelt-Struebe M, Boor P. HIF stabilization inhibits renal epithelial cell migration and is associated with cytoskeletal alterations. Scientific Reports. 2018;8(1):9497.
90. Wang Y, Ohh M. Oxygen-mediated endocytosis in cancer. Journal of Cellular and Molecular Medicine. 2010;14(3):496-503.
91. Koizume S, Ito S, Miyagi E, Hirahara F, Nakamura Y, Sakuma Y, et al. HIF2α-Sp1 interaction mediates a deacetylation-dependent FVII-gene activation under hypoxic conditions in ovarian cancer cells. Nucleic Acids Res. 2012;40(12):5389-401.
92. Gonzalez-Flores A, Aguilar-Quesada R, Siles E, Pozo S, Rodríguez-Lara MI, López –Jiménez L, et al. Interaction between PARP-1 and HIF-2α in the hypoxic response. Oncogene. 2014;33(7):891-8.

93. Villa JC, Chiu D, Brandes AH, Escorcia FE, Villa CH, Maguire WF, et al. Nontranscriptional role of Hif-1α in activation of γ-secretase and notch signaling in breast cancer. Cell reports. 2014;8(4):1077-92.
94. Lutz MS, Burk RD. Primary cilium formation requires von hippel-lindau gene function in renal-derived cells. Cancer Res. 2006;66(14):6903-7.
95. Esteban MA, Harten SK, Tran MG, Maxwell PH. Formation of primary cilia in the renal epithelium is regulated by the von Hippel-Lindau tumor suppressor protein. J Am Soc Nephrol. 2006;17(7):1801-6.
96. Wann A.K.T TCL, Chapple J.P., Martin M Knight M.M. Interleukin-1β sequesters hypoxia inducible factor 2α to the primary cilium. Cilia. 2013;2(17):1-14.
97. Ho JJD, Wang M, Audas Timothy E, Kwon D, Carlsson Steven K, Timpano S, et al. Systemic Reprogramming of Translation Efficiencies on Oxygen Stimulus. Cell Reports. 2016;14(6):1293-300.
98. Vanharanta S, Shu W, Brenet F, Hakimi AA, Heguy A, Viale A, et al. Epigenetic expansion of VHL-HIF signal output drives multiorgan metastasis in renal cancer. Nat Med. 2013;19(1):50-6.
99. Schokrpur S, Hu J, Moughon DL, Liu P, Lin LC, Hermann K, et al. CRISPR-Mediated VHL Knockout Generates an Improved Model for Metastatic Renal Cell Carcinoma. Scientific Reports. 2016;6(1):29032.
100. Wong SC, Cheng W, Hamilton H, Nicholas AL, Wakefield DH, Almeida A, et al. HIF2alpha-Targeted RNAi Therapeutic Inhibits Clear Cell Renal Cell Carcinoma. Mol Cancer Ther. 2018;17(1):140-9.
101. Shinojima T, Oya M, Takayanagi A, Mizuno R, Shimizu N, Murai M. Renal cancer cells lacking hypoxia inducible factor (HIF)-1α expression maintain vascular endothelial growth factor expression through HIF-2α. Carcinogenesis. 2007;28(3):529-36.
102. Biswas S, Troy H, Leek R, Chung Y-L, Li J-l, Raval RR, et al. Effects of HIF-1 ? and HIF2 ? on Growth and Metabolism of Clear-Cell Renal Cell Carcinoma 786-0 Xenografts. Journal of Oncology. 2010;2010:757908.
103. Cancer Genome Atlas Research N. Comprehensive molecular characterization of clear cell renal cell carcinoma. Nature. 2013;499(7456):43-9.
104. Chakraborty AA, Nakamura E, Qi J, Creech A, Jaffe JD, Paulk J, et al. HIF activation causes synthetic lethality between the VHL tumor suppressor and the EZH1 histone methyltransferase. Sci Transl Med. 2017;9(398):eaal5272.
105. Nicholson HE, Tariq Z, Housden BE, Jennings RB, Stransky LA, Perrimon N, et al. HIF-independent synthetic lethality between CDK4/6 inhibition and VHL loss across species. Science Signaling. 2019;12(601):eaay0482.
106. Sun N, Petiwala S, Lu C, Hutti JE, Hu M, Hu M, et al. VHL Synthetic Lethality Signatures Uncovered by Genotype-Specific CRISPR-Cas9 Screens. Crispr j. 2019;2:230-45.

107. Bouhamdani N, Comeau D, Coholan A, Cormier K, Turcotte S. Targeting lysosome function causes selective cytotoxicity in VHL-inactivated renal cell carcinomas. Carcinogenesis. 2019.
108. Singhal R, Mitta SR, Olive KP, Lyssiotis CA, Shah YM. Hypoxia inducible factor-2α increases sensitivity of colon cancer cells towards oxidative cell death. bioRxiv. 2019:823997.
109. Dong W, Wu X. Overexpression of Rab11-FIP2 in colorectal cancer cells promotes tumor migration and angiogenesis through increasing secretion of PAI-1. Cancer Cell Int. 2018;18:35-.
110. Zong S, Li W, Li H, Han S, Liu S, Shi Q, et al. Identification of hypoxia-regulated angiogenic genes in colorectal cancer. Biochem Biophys Res Commun. 2017;493(1):461-7.
111. Riechelmann R, Grothey A. Antiangiogenic therapy for refractory colorectal cancer: current options and future strategies. Ther Adv Med Oncol. 2017;9(2):106-26.
112. Moreno Roig E, Yaromina A, Houben R, Groot AJ, Dubois L, Vooijs M. Prognostic Role of Hypoxia-Inducible Factor-2alpha Tumor Cell Expression in Cancer Patients: A Meta-Analysis. Front Oncol. 2018;8:224.
113. Das B, Pal B, Bhuyan R, Li H, Sarma A, Gayan S, et al. MYC Regulates the HIF2a Stemness Pathway via Nanog and Sox2 to Maintain Self-Renewal in Cancer Stem Cells versus Non-Stem Cancer Cells. Cancer Research. 2019;79(16):4015-25.
114. Zhang Q, Lou Y, Zhang J, Fu Q, Wei T, Sun X, et al. Hypoxia-inducible factor-2α promotes tumor progression and has crosstalk with Wnt/β-catenin signaling in pancreatic cancer. Molecular Cancer. 2017;16(1):119.
115. Zimmer M, Ebert BL, Neil C, Brenner K, Papaioannou I, Melas A, et al. Small-Molecule Inhibitors of HIF-2a Translation Link Its 5'UTR Iron-Responsive Element to Oxygen Sensing. Molecular Cell. 2008;32(6):838-48.
116. Metelo AM, Noonan HR, Li X, Jin Y, Baker R, Kamentsky L, et al. Pharmacological HIF2α inhibition improves VHL disease-associated phenotypes in zebrafish model. J Clin Invest. 2015;125(5):1987-97.
117. Wallace EM, Rizzi JP, Han G, Wehn PM, Cao Z, Du X, et al. A Small-Molecule Antagonist of HIF2α Is Efficacious in Preclinical Models of Renal Cell Carcinoma. Cancer Research. 2016;76(18):5491-500.
118. Xu R, Wang K, Rizzi JP, Huang H, Grina JA, Schlachter ST, et al. 3-[(1S,2S,3R)-2,3-Difluoro-1-hydroxy-7-methylsulfonylindan-4-yl]oxy-5-fluorobenzonitrile (PT2977), a Hypoxia-Inducible Factor 2α (HIF-2α) Inhibitor for the Treatment of Clear Cell Renal Cell Carcinoma. Journal of Medicinal Chemistry. 2019;62(15):6876-93.
119. Persson CU, von Stedingk K, Fredlund E, Bexell D, Pahlman S, Wigerup C, et al. ARNT-dependent HIF-2 transcriptional activity is not sufficient to regulate

downstream target genes in neuroblastoma. Exp Cell Res. 2020;388(2):111845.
120. Courtney KD, Ma Y, Diaz de Leon A, Christie A, Xie Z, Woolford L, et al. HIF-2 Complex Dissociation, Target Inhibition, and Acquired Resistance with PT2385, a First-in-Class HIF-2 Inhibitor in Clear Cell Renal Cell Carcinoma Patients. Clinical Cancer Research. 2019:clincanres.1459.2019.
121. Okazaki KM, Maltepe E. Oxygen, epigenetics and stem cell fate. Regenerative Medicine. 2006;1(1):71-83.
122. Maltepe E, Krampitz GW, Okazaki KM, Red-Horse K, Mak W, Simon MC, et al. Hypoxia-inducible factor-dependent histone deacetylase activity determines stem cell fate in the placenta. Development. 2005;132(15):3393-403.
123. Kato H, Tamamizu-Kato S, Shibasaki F. Histone Deacetylase 7 Associates with Hypoxia-inducible Factor 1α and Increases Transcriptional Activity. Journal of Biological Chemistry. 2004;279(40):41966-74.
124. Arany Z, Huang LE, Eckner R, Bhattacharya S, Jiang C, Goldberg MA, et al. An essential role for p300/CBP in the cellular response to hypoxia. Proceedings of the National Academy of Sciences. 1996;93(23):12969-73.
125. Batie M, Frost J, Frost M, Wilson JW, Schofield P, Rocha S. Hypoxia induces rapid changes to histone methylation and reprograms chromatin. Science. 2019;363(6432):1222-6.
126. Du R, Xia L, Ning X, Liu L, Sun W, Huang C, et al. Hypoxia-induced Bmi1 promotes renal tubular epithelial cell–mesenchymal transition and renal fibrosis via PI3K/Akt signal. Molecular Biology of the Cell. 2014;25(17):2650-9.
127. Jin X, Kim LJY, Wu Q, Wallace LC, Prager BC, Sanvoranart T, et al. Targeting glioma stem cells through combined BMI1 and EZH2 inhibition. Nature Medicine. 2017;23(11):1352-61.
128. Wang X, Wang Y, Li L, Xue X, Xie H, Shi H, et al. A lncRNA coordinates with Ezh2 to inhibit HIF-1α transcription and suppress cancer cell adaption to hypoxia. Oncogene. 2020;39(9):1860-74.
129. Mahara S, Chng WJ, Yu Q. Molecular switch of EZH2 in hypoxia. Cell Cycle. 2016;15(22):3007-8.
130. Kim J, Lee Y, Lu X, Song B, Fong K-W, Cao Q, et al. Polycomb- and Methylation-Independent Roles of EZH2 as a Transcription Activator. Cell Reports. 2018;25(10):2808-20.e4.
131. Yamagishi M, Hori M, Fujikawa D, Ohsugi T, Honma D, Adachi N, et al. Targeting Excessive EZH1 and EZH2 Activities for Abnormal Histone Methylation and Transcription Network in Malignant Lymphomas. Cell Reports. 2019;29(8):2321-37.e7.

132. Mahara S, Lee PL, Feng M, Tergaonkar V, Chng WJ, Yu Q. HIFI-alpha activation underlies a functional switch in the paradoxical role of Ezh2/PRC2 in breast cancer. Proc Natl Acad Sci U S A. 2016;113(26):E3735-44.
133. Fu Y, Chen J, Pang B, Li C, Zhao J, Shen K. EZH2-induced H3K27me3 is associated with epigenetic repression of the ARHI tumor-suppressor gene in ovarian cancer. Cell Biochem Biophys. 2015;71(1):105-12.
134. Gao SB, Zheng QF, Xu B, Pan CB, Li KL, Zhao Y, et al. EZH2 represses target genes through H3K27-dependent and H3K27-independent mechanisms in hepatocellular carcinoma. Mol Cancer Res. 2014;12(10):1388-97.
135. Gan L, Yang Y, Li Q, Feng Y, Liu T, Guo W. Epigenetic regulation of cancer progression by EZH2: from biological insights to therapeutic potential. Biomarker Research. 2018;6(1):10.
136. Wassef M, Michaud A, Margueron R. Association between EZH2 expression, silencing of tumor suppressors and disease outcome in solid tumors. Cell Cycle. 2016;15(17):2256-62.
137. Andrews D, Oliviero G, De Chiara L, Watson A, Rochford E, Wynne K, et al. Unravelling the transcriptional responses of TGF-β: Smad3 and EZH2 constitute a regulatory switch that controls neuroretinal epithelial cell fate specification. The FASEB Journal. 2019;33(5):6667-81.
138. Nuytten M, Beke L, Van Eynde A, Ceulemans H, Beullens M, Van Hummelen P, et al. The transcriptional repressor NIPP1 is an essential player in EZH2-mediated gene silencing. Oncogene. 2008;27(10):1449-60.
139. Hirukawa A, Smith H, Zuo D, Dufour C, Savage P, Bertos N, et al. Targeting EZH2 reactivates a breast cancer subtype-specific anti-metastatic transcriptional program. Nature Communications. 2018;9.
140. Margueron R, Li G, Sarma K, Blais A, Zavadil J, Woodcock CL, et al. Ezh1 and Ezh2 maintain repressive chromatin through different mechanisms. Mol Cell. 2008;32(4):503-18.
141. Ren G, Baritaki S, Marathe H, Feng J, Park S, Beach S, et al. Polycomb protein EZH2 regulates tumor invasion via the transcriptional repression of the metastasis suppressor RKIP in breast and prostate cancer. Cancer Res. 2012;72(12):3091-104.
142. Zhaomei Mu, Hua Li, Sandra V Fernandez, Katherine R Alpaugh, Rugang Zhang and, Cristofanilli M. EZH2 knockdown suppresses the growth and invasion of human inflammatory breast cancer cells. Journal of Experimental & Clinical Cancer Research. 2013;32(70):1-9.
143. Liu L, Xu Z, Zhong L, Wang H, Jiang S, Long Q, et al. Prognostic Value of EZH2 Expression and Activity in Renal Cell Carcinoma: A Prospective Study. PloS one. 2013;8:e81484.

144. Sashida G, Iwama A. Multifaceted role of the polycomb-group gene EZH2 in hematological malignancies. International Journal of Hematology. 2017;105(1):23-30.
145. Skoda RC, Schwaller J. Dual roles of EZH2 in acute myeloid leukemia. Journal of Experimental Medicine. 2019;216(4):725-7.
146. Wassef M, Luscan A, Aflaki S, Zielinski D, Jansen PWTC, Baymaz HI, et al. EZH1/2 function mostly within canonical PRC2 and exhibit proliferation-dependent redundancy that shapes mutational signatures in cancer. Proceedings of the National Academy of Sciences. 2019;116(13):6075-80.
147. Gunawan M, Venkatesan N, Loh JT, Wong JF, Berger H, Neo WH, et al. The methyltransferase Ezh2 controls cell adhesion and migration through direct methylation of the extranuclear regulatory protein talin. Nature Immunology. 2015;16(5):505-16.
148. Venkatesan N, Wong JF, Tan KP, Chung HH, Yau YH, Cukuroglu E, et al. EZH2 promotes neoplastic transformation through VAV interaction-dependent extranuclear mechanisms. Oncogene. 2018;37(4):461-77.
149. Hoffmeyer K, Junghans D, Kanzler B, Kemler R. Trimethylation and Acetylation of β-Catenin at Lysine 49 Represent Key Elements in ESC Pluripotency. Cell Reports. 2017;18(12):2815-24.
150. Su Ih, Dobenecker M-W, Dickinson E, Oser M, Basavaraj A, Marqueron R, et al. Polycomb Group Protein Ezh2 Controls Actin Polymerization and Cell Signaling. Cell. 2005;121(3):425-36.
151. Razidlo GL, Magnine C, Sletten AC, Hurley RM, Almada LL, Fernandez-Zapico ME, et al. Targeting Pancreatic Cancer Metastasis by Inhibition of Vav1, a Driver of Tumor Cell Invasion. Cancer Res. 2015;75(14):2907-15.
152. Loh JT, Lim TJF, Ikumi K, Matoba T, Janela B, Gunawan M, et al. Ezh2 Controls Skin Tolerance through Distinct Mechanisms in Different Subsets of Skin Dendritic Cells. iScience. 2018;10:23-39.
153. Chan HL, Beckedorff F, Zhang Y, Garcia-Huidobro J, Jiang H, Colaprico A, et al. Polycomb complexes associate with enhancers and promote oncogenic transcriptional programs in cancer through multiple mechanisms. Nature Communications. 2018;9(1):3377.
154. Kahn TG, Dorafshan E, Schultheis D, Zare A, Stenberg P, Reim I, et al. Interdependence of PRC1 and PRC2 for recruitment to Polycomb Response Elements. Nucleic acids research. 2016;44(21):10132-49.
155. Leisz S, Schulz K, Erb S, Oefner P, Dettmer K, Mougiakakos D, et al. Distinct von Hippel-Lindau gene and hypoxia-regulated alterations in gene and protein expression patterns of renal cell carcinoma and their effects on metabolism. Oncotarget. 2015;6.

156. Maxwell PH, Wiesener MS, Chang G-W, Clifford SC, Vaux EC, Cockman ME, et al. The tumour suppressor protein VHL targets hypoxia-inducible factors for oxygen-dependent proteolysis. Nature. 1999;399(6733):271-5.
157. Shen C, Beroukhim R, Schumacher SE, Zhou J, Chang M, Signoretti S, et al. Genetic and functional studies implicate HIF1α as a 14q kidney cancer suppressor gene. Cancer discovery. 2011;1(3):222-35.
158. Bloomfield KL, Baldwin BL, Harkin DG, Tonissen KF. Modification of the Boyden chamber to improve uniformity of cell invasion of matrigel-coated membranes. Biotechniques. 2001;31(6):1242, 4, 6.
159. Justus CR, Leffler N, Ruiz-Echevarria M, Yang LV. In vitro cell migration and invasion assays. J Vis Exp. 2014(88):51046.
160. Erbel PJ, Card PB, Karakuzu O, Bruick RK, Gardner KH. Structural basis for PAS domain heterodimerization in the basic helix--loop--helix-PAS transcription factor hypoxia-inducible factor. Proc Natl Acad Sci U S A. 2003;100(26):15504-9.
161. Rogers JL, Bayeh L, Scheuermann TH, Longgood J, Key J, Naidoo J, et al. Development of inhibitors of the PAS-B domain of the HIF-2alpha transcription factor. J Med Chem. 2013;56(4):1739-47.
162. Satcher RL, Pan T, Cheng C-J, Lee Y-C, Lin S-C, Yu G, et al. Cadherin-11 in renal cell carcinoma bone metastasis. PloS one. 2014;9(2):e89880-e.
163. Liou Y-F, Hsieh Y-S, Hung T-W, Chen P-N, Chang Y-Z, Kao S-H, et al. Thymoquinone inhibits metastasis of renal cell carcinoma cell 786-O-SI3 associating with downregulation of MMP-2 and u-PA and suppression of PI3K/Src signaling. Int J Med Sci. 2019;16(5):686-95.
164. Pan T, Fong ELS, Martinez M, Harrington DA, Lin S-H, Farach-Carson MC, et al. Three-dimensional (3D) culture of bone-derived human 786-O renal cell carcinoma retains relevant clinical characteristics of bone metastases. Cancer Lett. 2015;365(1):89-95.
165. Ishiyama N, Lee S-H, Liu S, Li G-Y, Smith MJ, Reichardt LF, et al. Dynamic and Static Interactions between p120 Catenin and E-Cadherin Regulate the Stability of Cell-Cell Adhesion. Cell. 2010;141(1):117-28.
166. Pieters T, Goossens S, Haenebalcke L, Andries V, Stryjewska A, De Rycke R, et al. p120 Catenin-Mediated Stabilization of E-Cadherin Is Essential for Primitive Endoderm Specification. PLOS Genetics. 2016;12(8):e1006243.
167. Yuan Y, Hilliard G, Ferguson T, Millhorn DE. Cobalt inhibits the interaction between hypoxia-inducible factor-alpha and von Hippel-Lindau protein by direct binding to hypoxia-inducible factor-alpha. J Biol Chem. 2003;278(18):15911-6.
168. Jilg CA, Neumann HP, Gläsker S, Schäfer O, Ardelt PU, Schwardt M, et al. Growth Kinetics in Von Hippel-Lindau-Associated Renal Cell Carcinoma. Urologia Internationalis. 2012;88(1):71-8.

169. Wolf MM, Kimryn Rathmell W, Beckermann KE. Modeling clear cell renal cell carcinoma and therapeutic implications. Oncogene. 2020;39(17):3413-26.
170. Petrella BL, Brinckerhoff CE. Tumor cell invasion of von Hippel Lindau renal cell carcinoma cells is mediated by membrane type-1 matrix metalloproteinase. Mol Cancer. 2006;5:66.
171. Luo J, Lee S, Cui Y, Yang R, li L, Chang C. Infiltrating bone marrow mesenchymal stem cells (BM-MSCs) increase prostate cancer cell invasion via altering the CCL5/HIF2alpha/androgen receptor signals. Oncotarget. 2015;6.
172. Evelonn EA, Landfors M, Haider Z, Kohn L, Ljungberg B, Roos G, et al. DNA methylation associates with survival in non-metastatic clear cell renal cell carcinoma. BMC Cancer. 2019;19(1):65.
173. Bratslavsky G, Liu JJ, Johnson AD, Sudarshan S, Choyke PL, Linehan WM, et al. Salvage Partial Nephrectomy for Hereditary Renal Cancer: Feasibility and Outcomes. The Journal of Urology. 2008;179(1):67-70.
174. Huang C-R, Lee C-T, Chang K-Y, Chang W-C, Liu Y-W, Lee J-C, et al. Down-regulation of ARNT promotes cancer metastasis by activating the fibronectin/integrin β1/FAK axis. Oncotarget. 2015;6(13).
175. Sobczuk P, Brodziak A, Khan MI, Chhabra S, Fiedorowicz M, Wełniak-Kamińska M, et al. Choosing The Right Animal Model for Renal Cancer Research. Transl Oncol. 2020;13(3):100745.
176. Tausendschön M, Rehli M, Dehne N, Schmidl C, Döring C, Hansmann M-L, et al. Genome-wide identification of hypoxia-inducible factor-1 and -2 binding sites in hypoxic human macrophages alternatively activated by IL-10. Biochimica et Biophysica Acta (BBA) - Gene Regulatory Mechanisms. 2015;1849(1):10-22.
177. Chan N, Pires IM, Bencokova Z, Coackley C, Luoto KR, Bhogal N, et al. Contextual synthetic lethality of cancer cell kill based on the tumor microenvironment. Cancer Res. 2010;70(20):8045-54.
178. Wang Q, Xu L, Zhang X, Liu D, Wang R. GSK343, an inhibitor of EZH2, mitigates fibrosis and inflammation mediated by HIF-1α in human peritoneal mesothelial cells treated with high glucose. European journal of pharmacology. 2020;880:173076.
179. Au - Xia X, Au - Li H, Au - Satheesan S, Au - Zhou J, Au - Rossi JJ. Humanized NOD/SCID/IL2 null (hu-NSG) Mouse Model for HIV Replication and Latency Studies. JoVE. 2019(143):e58255.
180. Hou W, Ji Z. Generation of autochthonous mouse models of clear cell renal cell carcinoma: mouse models of renal cell carcinoma. Experimental & Molecular Medicine. 2018;50(4):30.
181. Alfranca A, Gutiérrez MD, Vara A, Aragonés J, Vidal F, Landázuri MO. c-Jun and Hypoxia-Inducible Factor 1 Functionally Cooperate in Hypoxia-

Induced Gene Transcription. Molecular and Cellular Biology. 2002;22(1):12-22.
182. Yu B, Miao Z-H, Jiang Y, Li M-H, Yang N, Li T, et al. c-Jun Protects Hypoxia-Inducible Factor-1α from Degradation via Its Oxygen-Dependent Degradation Domain in a Nontranscriptional Manner. Cancer Research. 2009;69(19):7704-12.
183. Amelio I, Mancini M, Petrova V, Cairns RA, Vikhreva P, Nicolai S, et al. p53 mutants cooperate with HIF-1 in transcriptional regulation of extracellular matrix components to promote tumor progression. Proceedings of the National Academy of Sciences. 2018;115(46):E10869-E78.
184. Prickaerts P, Adriaens ME, Beucken Tvd, Koch E, Dubois L, Dahlmans VEH, et al. Hypoxia increases genome-wide bivalent epigenetic marking by specific gain of H3K27me3. Epigenetics & Chromatin. 2016;9(1):46.
185. Mitic T, Caporali A, Floris I, Meloni M, Marchetti M, Urrutia R, et al. EZH2 modulates angiogenesis in vitro and in a mouse model of limb ischemia. Mol Ther. 2015;23(1):32-42.
186. Dardenne E, Beltran H, Benelli M, Gayvert K, Berger A, Puca L, et al. N-Myc Induces an EZH2-Mediated Transcriptional Program Driving Neuroendocrine Prostate Cancer. Cancer Cell. 2016;30(4):563-77.
187. Ku M, Koche RP, Rheinbay E, Mendenhall EM, Endoh M, Mikkelsen TS, et al. Genomewide Analysis of PRC1 and PRC2 Occupancy Identifies Two Classes of Bivalent Domains. PLOS Genetics. 2008;4(10):e1000242.
188. Dietrich N, Lerdrup M, Landt E, Agrawal-Singh S, Bak M, Tommerup N, et al. REST–Mediated Recruitment of Polycomb Repressor Complexes in Mammalian Cells. PLoS genetics. 2012;8:e1002494.
189. Zhou H, Wu G, Ma X, Xiao J, Yu G, Yang C, et al. Attenuation of TGFBR2 expression and tumour progression in prostate cancer involve diverse hypoxia-regulated pathways. J Exp Clin Cancer Res. 2018;37(1):89.
190. Hernando H, Gelato K, Lesche R, Beckmann G, Koehr S, Otto S, et al. EZH2 Inhibition Blocks Multiple Myeloma Cell Growth through Upregulation of Epithelial Tumor Suppressor Genes. Molecular Cancer Therapeutics. 2015;15.
191. Lv Y-F, Yan G-N, Meng G, Zhang X, Guo Q-N. Enhancer of zeste homolog 2 silencing inhibits tumor growth and lung metastasis in osteosarcoma. Scientific reports. 2015;5:12999.
192. Juraleviciute M, Pozniak J, Nsengimana J, Harland M, Randerson-Moor J, Wernhoff P, et al. MX 2 is a novel regulator of cell cycle in melanoma cells. Pigment Cell Melanoma Res. 2020;33(3):446-57.
193. Maia CJ, Rocha SM, Socorro S, Schmitt F, Santos CR. Oligoadenylate synthetase 1 (OAS1) expression in human breast and prostate cancer cases, and its regulation by sex steroid hormones. Advances in Modern Oncology Research. 2016;2(2).

194. Doherty MR, Cheon H, Junk DJ, Vinayak S, Varadan V, Telli ML, et al. Interferon-beta represses cancer stem cell properties in triple-negative breast cancer. Proc Natl Acad Sci U S A. 2017;114(52):13792-7.
195. Kim JC, Ha YJ, Tak KH, Roh SA, Kwon YH, Kim CW, et al. Opposite functions of GSN and OAS2 on colorectal cancer metastasis, mediating perineural and lymphovascular invasion, respectively. PLoS One. 2018;13(8):e0202856.
196. Yu T, Wang Y, Hu Q, Wu W, Wu Y, Wei W, et al. The EZH2 inhibitor GSK343 suppresses cancer stem-like phenotypes and reverses mesenchymal transition in glioma cells. Oncotarget. 2017;8(58).
197. Jackson PK. EZH2 Inactivates Primary Cilia to Activate Wnt and Drive Melanoma. Cancer Cell. 2018;34(1):3-5.
198. Basheer F, Giotopoulos G, Meduri E, Yun H, Mazan M, Sasca D, et al. Contrasting requirements during disease evolution identify EZH2 as a therapeutic target in AML. Journal of Experimental Medicine. 2019;216(4):966-81.
199. Ivanov AI, Nusrat A, Parkos CA. Endocytosis of Epithelial Apical Junctional Proteins by a Clathrin-mediated Pathway into a Unique Storage Compartment. Molecular Biology of the Cell. 2004;15(1):176-88.
200. Liao X-H, Zhang Y, Dong W-J, Shao Z-M, Li D-Q. Chromatin remodeling protein MORC2 promotes breast cancer invasion and metastasis through a PRD domain-mediated interaction with CTNND1. Oncotarget [Internet]. 2017 2017/11//; 8(58):[97941-54 pp.].
201. Liu Y, Li QC, Miao Y, Xu HT, Dai SD, Wei Q, et al. Ablation of p120-catenin enhances invasion and metastasis of human lung cancer cells. Cancer Sci. 2009;100(3):441-8.
202. Hernández-Martínez R, Ramkumar N, Anderson KV. p120-catenin regulates WNT signaling and EMT in the mouse embryo. Proceedings of the National Academy of Sciences. 2019;116(34):16872-81.
203. Kourtidis A, Ngok SP, Anastasiadis PZ. p120 catenin: an essential regulator of cadherin stability, adhesion-induced signaling, and cancer progression. Prog Mol Biol Transl Sci. 2013;116:409-32.
204. Venhuizen JH, Jacobs FJC, Span PN, Zegers MM. P120 and E-cadherin: Double-edged swords in tumor metastasis. Semin Cancer Biol. 2020;60:107-20.
205. Shi Y, Qin N, Zhou Q, Chen Y, Huang S, Chen B, et al. Role of IQGAP3 in metastasis and epithelial–mesenchymal transition in human hepatocellular carcinoma. Journal of Translational Medicine. 2017;15(1):176.
206. Dongol S, Zhang Q, Qiu C, Sun C, Zhang Z, Wu H, et al. IQGAP3 promotes cancer proliferation and metastasis in high-grade serous ovarian cancer. Oncology Letters. 2020.

207. Wu J, Chen Z, Cao H, Yu Z, Feng J, Wang K, et al. High expression of IQGAP3 indicates poor prognosis in colorectal cancer patients. Int J Biol Markers. 2019;34(4):348-55.
208. Hua X, Long Z-Q, Zhang W-W, Lin C, Sun X-Q, Wen W, et al. IQGAP3 Overexpression Correlates with Poor Prognosis and Radiation Therapy Resistance in Breast Cancer. bioRxiv. 2018:346163.
209. Hu W, Wang Z, Zhang S, Lu X, Wu J, Yu K, et al. IQGAP1 promotes pancreatic cancer progression and epithelial-mesenchymal transition (EMT) through Wnt/β-catenin signaling. Scientific Reports. 2019;9(1):7539.
210. Xu W, Xu B, Yao Y, Yu X, Cao H, Zhang J, et al. Overexpression and biological function of IQGAP3 in human pancreatic cancer. Am J Transl Res. 2016;8(12):5421-32.
211. Wang XX, Li XZ, Zhai LQ, Liu ZR, Chen XJ, Pei Y. Overexpression of IQGAP1 in human pancreatic cancer. Hepatobiliary Pancreat Dis Int. 2013;12(5):540-5.
212. Raman D, Sai J, Hawkins O, Richmond A. Adaptor protein2 (AP2) orchestrates CXCR2-mediated cell migration. Traffic. 2014;15(4):451-69.
213. Bucher D, Mukenhirn M, Sochacki KA, Saharuka V, Huck C, Zambarda C, et al. Focal adhesion-generated cues in extracellular matrix regulate cell migration by local induction of clathrin-coated plaques. bioRxiv. 2018:493114.
214. Yoon S-O, Shin S, Mercurio AM. Hypoxia Stimulates Carcinoma Invasion by Stabilizing Microtubules and Promoting the Rab11 Trafficking of the α6β4 Integrin. Cancer Research. 2005;65(7):2761-9.
215. Wang T, Gilkes D, Takano N, Xiang L, Luo W, Bishop C, et al. Hypoxia-inducible factors and RAB22A mediate formation of microvesicles that stimulate breast cancer invasion and metastasis. Proceedings of the National Academy of Sciences of the United States of America. 2014;111.
216. Howe EN, Burnette MD, Justice ME, Clancy JW, Guldner IH, Schnepp PM, et al. Rab11b-mediated integrin recycling promotes brain metastatic adaptation and outgrowth. bioRxiv. 2019:666750.
217. Schackmann RCJ, Tenhagen M, van de Ven RAH, Derksen PWB. p120-catenin in cancer – mechanisms, models and opportunities for intervention. Journal of Cell Science. 2013;126(16):3515-25.
218. Wu Q, Li G, Wen C, Zeng T, Fan Y, Liu C, et al. Monoubiquitination of p120-catenin is essential for TGFβ-induced epithelial-mesenchymal transition and tumor metastasis. Science Advances. 2020;6(4):eaay9819.
219. Hosking CR, Ulloa F, Hogan C, Ferber EC, Figueroa A, Gevaert K, et al. The Transcriptional Repressor Glis2 Is a Novel Binding Partner for p120 Catenin. Molecular Biology of the Cell. 2007;18(5):1918-27.

220. Chan SC, Zhang Y, Pontoglio M, Igarashi P. Hepatocyte nuclear factor-1β regulates Wnt signaling through genome-wide competition with β-catenin/lymphoid enhancer binding factor. Proceedings of the National Academy of Sciences of the United States of America. 2019;116(48):24133-42.
221. Nlandu Khodo S, Neelisetty S, Phillips M, Manolopoulou M, Bhave G, May L, et al. Blocking TGF- β and β -Catenin Epithelial Crosstalk Exacerbates CKD. Journal of the American Society of Nephrology. 2017;28:ASN.2016121351.
222. Daly CS, Flemban A, Shafei M, Conway ME, Qualtrough D, Dean SJ. Hypoxia modulates the stem cell population and induces EMT in the MCF-10A breast epithelial cell line. Oncol Rep. 2018;39(2):483-90.
223. Wang D, Wang Y, Kong T, Fan F, Jiang Y. Hypoxia-induced β-catenin downregulation involves p53-dependent activation of Siah-1. Cancer Science. 2011;102(7):1322-8.
224. Dybdal-Hargreaves N, Risinger A, Mooberry S. Regulation of E-cadherin localization by microtubule targeting agents: rapid promotion of cortical E-cadherin through p130CAS/Src inhibition by eribulin. Oncotarget. 2017;9.
225. Cox J, Mann M. MaxQuant enables high peptide identification rates, individualized p.p.b.-range mass accuracies and proteome-wide protein quantification. Nature Biotechnology. 2008;26(12):1367-72.
226. Tyanova S, Temu T, Sinitcyn P, Carlson A, Hein MY, Geiger T, et al. The Perseus computational platform for comprehensive analysis of (prote)omics data. Nature Methods. 2016;13(9):731-40.
227. Fischer AH, Jacobson KA, Rose J, Zeller R. Hematoxylin and eosin staining of tissue and cell sections. CSH Protoc. 2008;2008:pdb.prot4986.

Appendix

Abbreviations:

Prefixes

p	pico
n	nano
µ	micro
m	milli
c	centi
k	kilo

Units

°C	degree Celsius
A	ampere
Da	Dalton
g	gram
h	hour
l	liter
m	meter
min	minute
M	mol/l
s	second
U	unit
v/v	volume per volume
w/v	weight per volume

Other abbreviations

A	adenine
A	alanine, Ala
aa	amino acid
ANGPT2	angiopoietin 2
APS	ammoniumpersulfate
ARNT	Aryl Hydrocarbon Receptor Nuclear Translocator
ATCC	American type culture collection
ATP	adenosin-5’-triphosphate
b2M	β2-microglobulin
bp	Base pairs
BSA	bovine serum albumin

C	cytosine
ccRCC	clear cell renal cell carcinoma
CDH1	cadherin 1, E-cadherin
CDH2	cadherin 2, N-cadherin
CDK	cyclin-dependent kinase
cDNA	complementary DNA
ChIP	chromatin immunoprecipitation
ChIP-Seq	chromatin immunoprecipitation followed by deep-sequencing
CHX	cycloheximide
CITED2	Cbp/p300 interacting transactivator with Glu/Asp rich carboxy-terminal domain 2
CMV	cytomegalovirus
CRC	**c**olo**r**ectal **c**ancer
Ctrl	control
DAPI	4',6-diamidino-2-phenylindole, dihydrochloride
ddH_2O	bidistilled water
DMEM	Dulbecco's Modified Eagles Medium
DMSO	dimethyl sulfoxide
DNA	deoxyribonucleic acid
dNTPs	deoxyribonucleoside-5'-triphosphate (dATP, dCTP, dGTP, dTTP)
DTT	dithiothreitol
E	glutamic acid, Glu
E.coli	*Escherichia coli*
e.g.	exempli gratia, for example
ECL	enhanced chemoluminescence
EDTA	ethylendiamintetraacetate
EGF	epidermal growth factor
EGFR	epidermal growth factor receptor
EZH2	enhancer of zeste homolog 2, histone-lysine N-methyltransferase
FBS	fetal bovine serum
FC	fold change
FDR	false discovery rate
Fig.	figure
G	guanine
g rcf,	relative centrifugal force
GAPDH	glyceraldehyde-3-phosphate dehydrogenase
GFP	green fluorescent protein
GLUT1	Glucose transporter 1
GTP	guanosine-5'-triphosphate

HIF2α	hypoxia-inducible factor 2-alpha
HLH	helix-loop-helix
HRP	horseradish peroxidase
Hygro	hygromycin
IF	immunofluorescence
IgG	immunoglobulin
IP	immunoprecipitation
IRES	internal ribosomal entry site
K	lysine, Lys
K27	lysine 27
LB	lysogeny broth
M	methionine
mRNA	messenger RNA
MS	mass spectrometry
MTS	metastases
MX2	MX dynamin like GTPase 2
NEM	N-ethylmaleimide
NLS	nuclear localization signal
NOD	non-obese diabetic
NP-40	Nonidet P-40
NSG	NOD scid gamma NMRI-Foxn1nu/nu
nsc	non silencing control
OAS1	2'-5'-oligoadenylate synthetase 1
ODD	oxygen-dependent degradation
OE	overexpression
p	phospho
P	proline, Pro
PAGE	polyacrylamide gel electrophoresis
PAI2	phosphoribosylanthranilate isomerase 2, alternative SERPINB2 serpin family B member 2
PAS	a Per-Arnt-Sim domain
PBS	phosphate-buffered saline
PCR	polymerase chain reaction
PEI	polyethylenimine
PI	propidiumiodide
PMSF	phenylmethylsulfonyl fluoride
PVDF	polyvinylidene difluoride
Q	glutamine
QMY	Q322E, M338E, Y342T mutant

qPCR	quantitative PCR
R	arginine, Arg
RING	really interesting new gene
RNA	ribonucleic acid
RNase	ribonuclease
RT	room temperature
S	serine, Ser
scid	severe combined immunodeficient
SDS	sodium dodecyl sulfate
SDS-PAGE	SDS polyacrylamide gel electrophoresis
SEM	standard error of the mean
sgRNA	single guide ribonucleic acid
sh	short hairpin
siRNA	short interfering ribonucleic acid
siRNA	small interfering RNA
T	threonine, Thr
TAD	transactivation domain
TBS	Tris-buffered saline
TBS-T	Tris-buffered saline with tween-20
TE	Tris-EDTA buffer
TEMED	N,N,N’,N’-tetramethylethylendiamine
TNT	Tris-NaCl-Triton X-100
Tris	Tris-(hydroxymethyl)-aminomethane
Ub	ubiquitin
UTR	untranslated region
VEGFA	vascular endothelial growth factor A
VHL	Von Hippel-Lindau Tumor Suppressor, E3 Ubiquitin Protein
WB	western blot
WT	wild type
Y	tyrosine, Tyr

Acknowledgments

First of all, I would like to thank Prof. Dr. Nikita Popov for supervising this thesis and for giving me the opportunity to work on this project on the whole way from Comprehensive Cancer Center Mainfranken Würzburg to the University Hospital Tübingen. I am very grateful for the guidance, advice, constant support, discussions, and the wonderful scientific microenvironment which motivated me throughout the years.

I would also like to thank Prof. Dr. Stefan Laufer for his support and commitment as the committee head, and especially for catalyzing the defense procedure.

I thank Prof. Dr. Prof. Schwarzer and Prof. Dr. Matthias Gehringer for being members of my thesis committee and for providing the opportunity to present and discuss my project here at the Eberhard Karls Universität Tübingen.

I am grateful to my previous thesis committee members Prof. Almut Schulze, Dr. Grzegorz Sumara, and Prof. Martin Eilers at the Julius-Maximilians-Universität Würzburg for the fruitful discussions and constructive criticism in the meetings we had.

I would also like to thank the Graduate School of Life Sciences in Würzburg for providing the soft skill courses, intercultural communication, and supporting the participation in conferences. I am also very grateful to the Postgraduate School at the Faculty of Science at the Eberhard Karls Universität Tübingen for giving me this possibility to defend this project here.

Many thanks to the members of the Hudeček, Jundt, Stühmel, Flentje, Eilers research groups for the technical help, amazing working atmosphere, and fruitful discussions.

I am very grateful to all former and present colleagues from our group who were always patient, ready to help, supportive, and inspiring during my PhD years: Andreas Hellman, Jing Xu, Ksenija Popova, Ravi Babu Kollampaly, Julia Horn, Vanessa Rousseau, Radhika Kharal, Chao Jin, and Elias Einig. Thank you all for a wonderful time spent together during all those years!

A special thanks to my dear colleagues Wenshan Xu and Valentina Andrioletti with whom I was working side by side (or rather bench to bench) for all their kind support, inspiration, confidence and sharing with me their strength on the way to the finish.

I am very grateful to Prof. Lars Zender and his lab members for the technical assistance, creative, very friendly and supportive atmosphere which transforms the scientific search into a pleasant adventure. My special thanks go to Elke Rist for her warm welcoming in the new lab, her enthusiasm and kind support.

I am very obliged to Dr. Angel Cuesta at the Centro de Investigaciones Biológicas (CIB), Madrid, Spain for sharing his unbreakable spirit and optimism, devotion to science, and, of course, enormous work on the *in vivo* part of this project.

I want to thank my family for their continuous encouragement, understanding, patience, belief, and love. You have taught me to follow my own way and supported my choices during the turbulent years on the road to becoming a scientist. I would like to thank my husband Omelyan for being so patient and staying with me during the nights in the lab, for encouraging and believing in me. Thank you for the help throughout this project starting from splitting the cells to experimental advice, protocols, help with the data analysis, and search for improvements.

This thesis would not have been possible without all of you!